Experimental, mesoscopic and statistical approaches of plasticity in polycrystals

Antoine Guitton

Mémoire

présenté en vue de l'obtention de

l'Habilitation à Diriger des Recherches

École Doctorale : Chimie – Mécanique – Matériaux – Physique (C2MP)

présenté par

Dr. Antoine Guitton

Approches expérimentales, mésoscopiques et statistiques de la plasticité dans les polycristaux

Experimental, mesoscopic and statistical approaches of plasticity in polycrystals

Soutenance publique le 30 mars 2022

Composition du jury

Dr. Samuel Forest	Directeur de Recherches CNRS, CDM, FR	*Rapporteur*
Prof. Sandra Korte-Kerzel	Professeure, RWTH Aachen University, DE	*Rapporteure*
Prof. Terry C. Lowe	Professeur, Colorado School of Mines, USA	*Rapporteur*
Prof. Nathalie Allain	Professeure, UL – LEM3, FR	*Examinatrice*
Prof. Emmanuel Bouzy	Professeur, UL – LEM3, FR	*Examinateur*
Prof. Thierry Grosdidier	Professeur, UL – LEM3, FR	*Examinateur*
Dr. Nabila Maloufi	Maître de Conférences HDR, UL – LEM3, FR	*Examinatrice*
Prof. Anthony D. Rollett	Professeur, Carnegie Mellon University, USA	*Président*
Prof. Ludovic Thilly	Professeur, Université de Poitiers – Institut P', FR	*Invité*

"It is a capital mistake to theorize before one has data. Insensibly one begins to twist facts to suit theories, instead of theories to suit facts." [1]

Sir Arthur Conan Doyle (1859–1930)

"All models are wrong but some are useful." [2]

George E. P. Box (1919–2013)

Many thanks!

Before getting to the heart of the matter, a little digression is needed to thank all those who provided help, knowledge, support, technique... in short, all those who made this HDR possible.

First af all, I would like to thank my former and current doctoral researchers – Hana Kriaa, Frederic Habiyaremye – and postdoctoral researchers – Chunyang Zhang, Meriem Ben Haj Slama and Kaustubh Venkatraman. I wish you all the best in your future endeavors.

In addition, I would like to express my sincere gratitude to Dr. Samuel Forest, Prof. Sandra Korte-Kerzel and Prof. Terry C. Lowe for having accepted to be reviewers of this manuscript. I would like to extend my sincere thanks to Prof. Nathalie Allain, Prof. Emmanuel Bouzy, Dr. Nabila Maloufi and Prof. Anthony D. Rollett for having accepted to be examiners and Prof. Thierry Grosdidier for accepting to be my mentor. I extend my warmest thanks to Prof. Ludovic Thilly for representing my thesis directors (Prof. Anne Joulain, Prof. Christophe Tromas and Prof. Ludovic Thilly), as invited member of this jury.

Research is a teamwork, that is why, I would like to offer my special thanks to all of my colleagues from LEM3 and particularly:

- Stéphane Berbenni
- Emmanuel Bouzy
- Benoît Beausir
- Jean-Jacques Fundenberger

- Lionel Germain
- Nathalie Gey
- Julien Guénolé
- Thierry Grosdidier
- Julien Guyon
- Jean-Sébastien Lecomte
- Nabila Maloufi
- Roxane Massion
- Marc Novelli
- Vincent Taupin
- Laszlo S. Toth
- Laurent Weiss
- Yudong Zhang

with who I am pleased to work and chat with.

I wish also all the best to Adrien Heinzelmeier, Julien Aubourg and Renaud Genin for their on-going doctoral research.

In addition, I would like to thank my colleagues from the IUT de Metz and particularly:

- Nathalie Allain
- Patrice Bourson
- Pierre Pino
- Jérôme Serri

Finally, I want to thank the LabEx DAMAS, the région Grand-Est and the CNRS through the MITI interdisciplinary programs for their financial supports.

Contents

Nomenclature

General notations (alphabetic order)

A	A-group element
A-ECCI	Accurate Electron Channeling Constrast Imaging
α_2	Hexagonal phase of TiAl alloys
ApC	Aperture alignment Coils
BCC	Body Centered Cubic
BDT	Brittle-to-Ductile Transition
BSE	BackScattered Electron
cECCI	controlled Electron Channeling Contrast Imaging
CPFEM	Crystal Plasticity models using Finite Elements
CPFFT	Crystal Plasticity models using Fast Fourier Transform algorithms
CRSS	Critical Resolved Shear Stress
DDD	Discrete Dislocation Dynamics
DP	Duplex

EBSD	Electron BackScatter Diffraction
ECCI	Electron Channeling Constrast Imaging
ECP	Electron Channeling Pattern
e.g.	*exempli gratia* = for example
EVPSC	Elasto-ViscoPlastic Self-Consistent
FCC	Face-Centered Cubic Structure
FL	Fully Lamellar
γ	Tetragonal phase of TiAl alloys
GB	Grain Boundary
GE	General Electric
GEnx	General Electric next Generation
GND	Geometrically Necessary Dislocation
HAGB	High-Angle Grain Boundary
HEA	High Entropy Alloy
HR-SACP	High-Resolution Selected Area Channeling Pattern
i.e.	*id est*
IKB	Incipient Kink Band
KB	Kink Band
KNE	Kinking Nonlinear Elastic
LAGB	Low-Angle Grain Boundary
LEAP	Leading Edge Aviation Propulsion
LEM3	*Laboratoire d'Étude des Microstructures et de Mécanique des Matériaux*: Laboratory of Studies of Microstructures and Mechanics of Materials

M	Transition metal
MEA	Medium Entropy Alloy
NG	Near-γ
NI	NanoIndentation
NID	Nanoindentation Induced Dislocation
NL	Near Lamellar
NT	Nano Twin
PCA	Principal Component Analysis
RSS	Resolved Shear Stress
SACP	Selected Area Channeling Pattern
SC	Scanning Coils
SE	Secondary Electron
SEM	Scanning Electron Microscope
SF	Stacking Fault
SMAT	Surface Mechanical Attrition
SSD	Statistically-Stored Dislocation
STEM-in-SEM	Scanning Transmission Electron Microscopy in a Scanning Electron Microscope
TB	Twin Boundary
TEM	Transmission Electron Microscope
VPSC	ViscoPlastic Self-Consistent
X	Carbon and/or nitrogen

Measures (apparition order)

x, y, z	Position coordinates
F	Macroscopic force
S	Section
Σ	Macroscopic stress
χ	Angle between the loading axis and the slip direction
φ	Angle between the loading axis and the normal to the slip plane
(α) or (β)	The slip systems of interest
m	SCHMID factor
(c)	Exponent referring to the crystal frame
$\tau_{RSS}^{(\alpha)}$	Resolved shear stress of the slip system (α)
$\tau_{CRSS}^{(\alpha)}$	Critical resolved shear stress of the slip system (α)
$\mathbf{M}^{(\alpha)}$	SCHMID tensor for the slip system (α)
$\mathbf{B}^{(\alpha)}$	Unit vector along the slip direction of the slip system (α)
$\mathbf{N}^{(\alpha)}$	Unit vector along the normal to the slip plane of the system (α)
$\overrightarrow{b}$	BURGERS vector
$\overrightarrow{u}$	Direction of a dislocation line
H	Height of a surface step
p	Number of dislocations
$\overrightarrow{n}$	Normal vector to the surface

$\overrightarrow{R}$	Translation vector
β	Misorientation
D	Spacing between dislocations in a LAGB
$\mathbf{n_{(GB)}}$	Normal to the grain boundary plane
$\boldsymbol{\sigma}$	Local stress tensor
$\mathbf{R}$	Rotation tensor
n	Stoechiometric number of MAX phases
$\overrightarrow{g}$	Diffracting vector
ρ_{GND}	Density of geometrically necessary dislocations
C	Constant
δx	Step size for the mapping
I_{BSE}	Intensity of backscattered electrons
ψ	Wave function
$\overrightarrow{h}$	Nodes of the reciprocal lattice
m_e	Mass of an electron
E	Kinetic energy of an electron
$\overrightarrow{r}$	Position vector
V_h	Complex FOURIER coefficients
(j)	The j-th wave
$\varepsilon^{(j)}$	Excitation amplitude of the j-th wave
$C_g^{(j)}$	Amplitude of diffracted j-th wave
$\overrightarrow{k_0^{(j)}}$	Wave vector of the j-th primary wave

$q^{(j)}$	Attenuation parameter expressing the exponential attenuation of the wave amplitude with increasing depth z
N	Atom number per unit of volume
σ_B	Cross section of backscattering
η_{OC}	Total BSE intensity due to the orientation contrast
ξ'_0 and ξ'_g	Absorption lengths
ξ_g	Extinction distance
ω	Tilt parameter
s	Deviation parameter of the incident beam respect with the Bragg condition
θ	Angle between the incident beam and the diffracting plane $(h\,k\,l)$
θ_B	Angle between the incident beam and the diffracting plane $(h\,k\,l)$ in Bragg condition
$\overrightarrow{v}$	Rotation axis
ω'	Modified tilt parameter
ω_{DP}	Tilt parameter due a planar defect
z_{DP}	Depth of a planar defect
η_{sup}	Contribution of the upper crystal with an equivalent thickness of z_{DP}
η_{inf}	Contribution of the translated lower crystal with an infinite thickness
η'_{inf}	Contribution of the lower crystal with an infinite thickness
η'_{inf}	Contribution of the lower crystal with an equivalent thickness of z_{DP}

T	Term of the BSE signal dependent on ω and z_{DP}
X	Characteristic distance
z_D	Depth of a dislocation
s_{exp}	Experimental deviation parameter
s_D	Deviation parameter due to a dislocation
$\overrightarrow{R}_{screw}$	Displacement field due to a screw dislocation
$\overrightarrow{R}_{edge}$	Displacement field due to an edge dislocation
h	Penetration depth
h_{max}	Maximum penetration depth
h_r	Penetration depth of the residual imprint
h_c	Penetration depth under contact
h_s	Elastic deformation out of contact
P	Pop-in load
h_p	Pop-in depth
A_p	Projected area
E^*	Reduced elastic modulus of nanoindentation
E_i	Elastic modulus of the indenter
E_s	Elastic modulus of the sample
ν_i	POISSON ratio of the indenter
ν_s	POISSON ratio of the sample
a	Radius of a spherical indenter
K	Number of points of one slip line

$\overrightarrow{\Pi}$ and $\overrightarrow{\Pi'}$	Correlation vectors
$\overrightarrow{f_i}$	base vectors for each family of slip planes
$\Delta\kappa_i$	Difference between angle measured by EBSD and angle measured on ECCI micrographs
$J_{r,c}$	Matrix of one with r rows and c columns
P	Number of detected slip lines
$\overrightarrow{\upsilon}$	Vector of the number of counts
$\mathcal{P}_i$	Probability of observing the slip line corresponding to the i plane family
χ	Sum of least squared differences
$f_{G\alpha G\beta}$	transmission factor between grains $G\alpha$ and $G\beta$
$n_{G\alpha}$, $n_{G\beta}$	Number of slip events in grains $G\alpha$ and $G\beta$
Φ	Classifier
f_{CP}	Crystal Plasticity model
f_{DP}	Deep Learning model
x_i	Inputs
y_i	True outputs
$\hat{y}_i$	Calculated outputs

Introduction

Developing new materials and understanding how they deform is the main challenge of researchers in order to follow and meet the challenging developments needed by a fast-paced and evolving society. For instance, in the framework of energy cost reductions, increasing mechanical performance of materials is synonymous with continuous improvements of experimental techniques leading to new insights on their fundamental deformation mechanisms, which then leads to design high-performance materials with enhanced properties. Although research in materials plasticity has developed for more than one century, it is fair to say that it still holds many secrets, particularly because of difficulties to extrapolate simplistic models to real samples, far from ideal cases. Cottrell summarized this conflict by qualifying the theory of plastic hardening as "the first problem to be attempted by dislocation theory and may be the last to be solved" [3].

Generally, materials are polycrystalline, *i.e.* they consist of millions of single crystals called grains. Grains have different orientations of the atom lattice and they are separated from neighboring grains by interfaces called Grain Boundaries (GBs). It is well established that the irreversible (or plastic) deformation of a sample originates mainly from the nucleation and the propagation of more than hundreds of billions per cm^3 of micrometric (even nanometric) linear defects of the regular crystal lattice called dislocations [4]. Dislocations move through the grain and interact with each other or with GBs. GBs may act in several ways: sinks, obstacles, traps

and sources of dislocations. Combination of experimental and simulations studies gives valuable insights on the operating mechanisms. Although, there exists a well-developed theory for describing the interaction between a single dislocation and a model GB, the response of several real GBs (contained in a real bulk polycrystalline sample) after receiving numerous dislocations is still a major scientific challenge. The mystery becomes inextricable, when one considers that there are more than hundreds of billions of dislocations per cm^3 of sample interacting together and with billions of GBs. Even more inextricable, if one wants to take into account influence of distribution of GBs, other types of interfaces, grain shape, grain orientation, and defects in the bulk sample *i.e.* its microstructure. Due to this inherent complexity, materials scientists have to bridge the gap between these two extreme length scales: sample (or macro-) scale and dislocation (or micro-) scale (Figure 1).

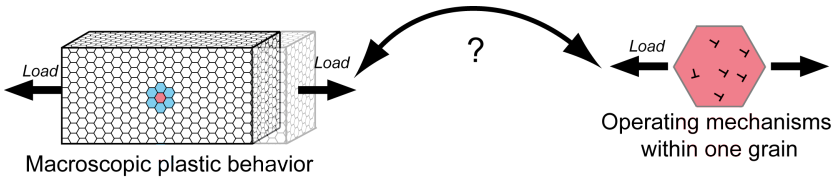

Figure 1 – Scale bridging between the microscopic and the macroscopic scales. A major challenge for materials scientists.

It is obvious that these two worlds interact with each other but their connections remain extremely difficult to understand because of need of extrapolations. Here, the role of micromechanical modeling brings new insight. Such computational schemes need constitutive equations that have to be "fed" with experimental criteria and parameters, capturing important operative mechanisms. However, such valuable experiments are still marginal and all suffer numerous constraints making interpretations unreliable statistically. These obstacles are now close to be overcome, through innovative experimental procedures, made now possible with recent progress in electron microscopy.

Such is the background to the current report. Chapter I summarizes basics of plasticity and the major role of microstructures in deformation mechanims. The example of MAX phases, a promising material for industries, is given, because they show reversible non-elastic phenomena due to the strong anisotropy of their mi-

crostructures. At the end of Chapter I, the influence of strain-path changes on plasticity has been introduced. The development of a miniaturized biaxial deformation rig is reported. Then, Chapter II focuses on the contribution of electron microscopy. Indeed, this is one of the most well-known technique for analyzing defects, thus allowing to understand their response to external solicitations. Two kinds of electron microscopes are generally used and bring complementary information: at micro/nano-scale, Transmission Electron Microscopy (TEM) and at macro/mesoscopic scale, Scanning Electron Microscopy (SEM). Because SEM can access diffraction contrast on bulk materials with the phenomenon of electron channeling, emphasis is on the Electron Channeling Contrast Imaging (ECCI) and its upgrade, the Accurate ECCI (A-ECCI), developed at LEM3. This leads to Chapter III, where physics of ECCI is presented for optimizing experimental conditions. Then Chapter IV explores the potentiality of A-ECCI for probing evolution of crystalline defects combined with localized deformation testing *i.e.* nanoindentation. Mechanisms near one unique GB are discussed in the framework of both a TiAl alloy and a medium-entropy alloy. Chapter V takes advantage of statistics offered by A-ECCI for confronting mesoscopic polycrystal plasticity models with experiments in a β-metastable Ti alloy. Finally, Chapter VI summarizes the importance of science popularization and describes my contributions in several actions.

Chapter I

Microstructure: a major and complex role in polycrystalline plasticity

I.1 From one interface to polycrystals with grain boundaries

I.1.1 Plasticity of monocrystal

It is well known that crystalline materials consist of stacks of atoms arranged in an orderly and periodic manner. Under the action of exterior stresses, specimen starts to deform. At a critical load (*i.e.* the yield stress), parallel and nanometric steps appear on the surface and they are aligned along specific planes and directions. These steps are the signatures of the irreversible (*i.e.* plastic) deformation. They originate from slip on planes along crystallographic directions, similar to the slip of card deck. Observations show that steps correspond to slip systems activated mainly on the most dense crystallographic planes and directions. For example, in the case of Face-Centered Cubic Structure (FCC), slip is on $\{1\,1\,1\}$ planes and along $\langle 1\,1\,0\rangle$ directions, thus giving 12 slip systems in total.

I.1.1.1 Slip systems and Schmid-Boas law in a monocrystal

In a monocrystal, activation of slip systems can be, more and less, predicted by the Schmid-Boas law [5]. Let us consider a crystal, with S as its section (Figure I.1), experiencing a uniaxial tensile force F.

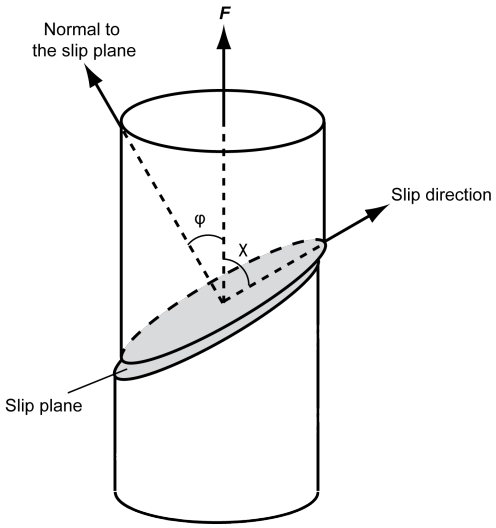

Figure I.1 – Schematic of the Schmid-Boas law.

The macroscopic stress, Σ, due to the application of F is written as $\Sigma = \frac{F}{S}$. Moreover, the component of F projected along the slip direction is $F\cos\chi$. This latter acts on the slip plane with a section equal to $\frac{S}{\cos\varphi}$. Therefore, the Resolved Shear Stress (RSS), $\tau_{RSS}^{(\alpha)}$, for the slip system (α), characterized by the normal to its slip plane (angle φ) and its slip direction (angle χ) is given by:

$$\tau_{RSS}^{(\alpha)} = \Sigma\cos\varphi\cos\chi \tag{I.1}$$

thus linking the RSS to the applied stress, Σ, through the Schmid factor, m, defined as follows:

$$m = \cos\varphi\cos\chi \tag{I.2}$$

Therefore, the system (α) will be active, if the RSS reaches a critical value, the Critical Resolved Shear Stress (CRSS), $\tau_{CRSS}^{(\alpha)}$.

In the general case of a non-uniaxial deformation, $\tau_{RSS}^{(\alpha)}$ is linked to the applied stress tensor written in the crystal frame (c), $\mathbf{T^{(c)}}$, through the Schmid tensor ($\otimes$ is the dyadic product):

$$\mathbf{M}^{(\alpha)} = \frac{1}{2}\left(\mathbf{B}^{(\alpha)}\otimes\mathbf{N}^{(\alpha)} + \mathbf{N}^{(\alpha)}\otimes\mathbf{B}^{(\alpha)}\right) \tag{I.3}$$

$$\tau_{RSS}^{(\alpha)} = \mathbf{T}^{(\mathbf{c})} : \mathbf{M}^{(\alpha)} \tag{I.4}$$

where:

- $\mathbf{B}^{(\alpha)}$: unit vector along the slip direction of the system (α);
- $\mathbf{N}^{(\alpha)}$: unit vector along the normal to the slip plane of the system (α).

I.1.1.2 Dislocations

Slip steps on the surface arise from the movement of several micrometric (even nanometric) linear defects of the regular crystal lattice called dislocations [4, 6]. Dislocations are characterized by the strain field they produce (given by the Burgers vector labelled $\overrightarrow{b}$) and the infinitely thin slip area assimilated by a line named the dislocation line (labeled $\overrightarrow{u}$) [7]. Therefore, the height H of a surface step is given by (p is the number of dislocations and $\overrightarrow{n}$ the normal vector to the surface):

$$H = p\,\overrightarrow{b} \cdot \overrightarrow{n} \tag{I.5}$$

Based on the angle between $\overrightarrow{b}$ and $\overrightarrow{u}$ ($\widehat{\overrightarrow{b}, \overrightarrow{u}}$), three types of dislocations are distinguished:

- for $\widehat{\overrightarrow{b}, \overrightarrow{u}} = 0°$, dislocations are called “screw”;
- for $\widehat{\overrightarrow{b}, \overrightarrow{u}} = 90°$, dislocations are called “edge”;
- for other cases, dislocations are called “mixed”.

The glide plane, with normal $\mathbf{N}^{(\alpha)}$, is defined by the plane $\left(\overrightarrow{b}, \overrightarrow{u}\right)$. Note that for screw dislocations, no unique glide plane can be associated. In most cases, $\overrightarrow{b}$ is a complete lattice translation vector of the crystalline network. Therefore, glide of such dislocations, called “perfect”, leaves a perfect crystal. Nevertheless, in some materials, dislocations with a Burgers that is a vector different from the crystalline network, can be observed. They are called “partial” and their glide leads to the formation of Stacking Faults (SFs).

SFs, as planar defects, can play an important role in plasticity of crystal. Indeed, they are local regions in the crystal where the regular stacking sequence is interrupted [8]. Such error in the stacking is associated to a translation vector $\overrightarrow{R}$ between both parts of the crystal.

I.1.2 Plasticity of polycrystal

I.1.2.1 Grain boundaries

Polycrystals consist of numerous grains separated by GBs [9]. According to synthesis and/or machining processes, crystallographic orientations of grains are random or with preferential orientations (*i.e.* texture). In a polycrystalline sample, each grain has it own orientation with the loading axis. Therefore, one grain will be deformed differently compared to its neighbors [10]. Because of this connection, the grain will undergo loading stress field reduced by the interaction stresses generated by surrounding grains in order to maintain the cohesion of the sample [9]. Therefore, the yield stress is generally higher in polycrystalline specimens compared to the single crystals [11]. Note that the interaction stresses are higher close to GBs than inside the grain [9], so that slip will occur essentially in its center. Moreover, in order to plastically deform a polycrystalline specimen by slip, the Taylor theory says, that minimum five independent slip systems have to be activated in each grain otherwise stress concentrations against GBs will occur, thus leading to cracking [12].

Interfaces, particularly GBs, may act in several ways. The behavior of dislocations reaching a GB depends on the applied stress, the temperature, and, of course, on the GB nature [9, 13, 14].

GBs are described by the misorientation between both adjacent crystals and by the orientation and the position of the GB plane itself. Only five macroscopic parameters are therefore necessary for describing the GB geometry [9]. It is convenient to categorize GBs according to their misorientation. Low-Angle Grain Boundaries (LAGBs) are those with misorientation less than about 20° [4, 9]. They can be described by relatively simple intrinsic dislocation configurations: tilt or twist LAGBs (Figure I.2) made up of walls of edge dislocations or screw dislocations respectively.

Mixed LAGBs consist of a wall of edge and screw dislocations.

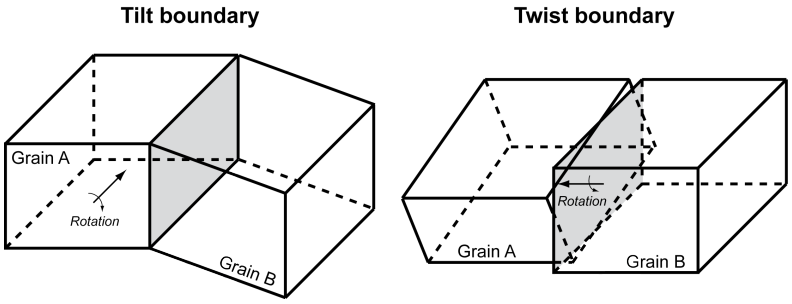

Figure I.2 – Schematic of a tilt GB (left) and twist GB (right).

For LAGBs, the misorientation, β, is related to spacing, D, between intrinsic dislocations with $\overrightarrow{b}$ as their BURGERS vector [8]:

$$D = \frac{\frac{\|\overrightarrow{b}\|}{2}}{\sin\frac{\beta}{2}} \sim \frac{\|\overrightarrow{b}\|}{\beta} \tag{I.6}$$

From equation I.6, it is clear that high misorientations lead to dislocation spacing reduced to one or two atomic spacing. Therefore, the description of such GB in terms of walls of distinguishable dislocations does not make sense anymore. These High-Angle Grain Boundaries (HAGBs), whose misorientation is greater than about $\beta \approx 20°$, become a region of severe localized disorder [4].

Concerning GB energy, its variations with misorientation are shown in Figure I.3 for a tilt GB in a FCC structure and for a twist in a hexagonal structure. After a linear increase to $\beta \approx 20°$, associated with the LAGB nature of the tilt GB, several local minimums are observed for particular values of β. These HAGBs with low interfacial energies at particular misorientations can be separated into two categories: coincident GB and coherent Twin Boundary (TB). Coherence means that atoms on both sides of the GB have a one-to-one matching and for coincident GB, only some atoms may match. Concerning coherent TB, they can be described as a 60°-rotation around $\langle 1\,1\,1\rangle$ (equivalent to 70.53°-$\langle 1\,1\,0\rangle$ in Figure I.3.a) for FCC or they separate two grains, whose lattices are mirror images of each other by reflection in the TB plane. Note that incoherent TBs exist and their plane does not coincide with the twinning plane [15].

In a polycrystal, dislocations move through the grain and interact with each

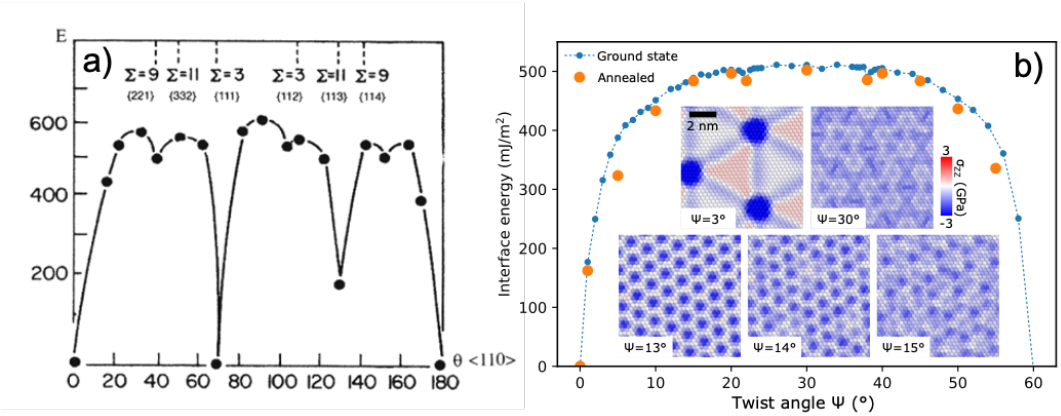

Figure I.3 – Variations of GB energy with misorientation (in $mJ{\cdot}m^{-2}$) a) calculated at 0 K for tilt GB symetric around $\langle 1\,1\,0 \rangle$ in Al, from[9] and b) for a twist GB in Ti_3AlC_2, with magnified views of the stress field σ_{zz}, from [16].

other or with GBs, acting in several ways (sinks, obstacles, traps and sources of dislocations), so that they are very important from the mechanical properties point of view [9]. One of the best-known model based on dislocation pile-up at GBs (described by the HALL-PETCH equation [17]) predicts that the yield stress of the sample is inversely proportional to the square root of its grain size. Therefore, such microscopic operating mechanisms have a direct influence on the strategies employed for designing polycrystalline materials [18–20].

I.1.2.2 Interactions between dislocations and GB

Plastic deformation of polycrystalline materials is strongly influenced by the microstructure, in particular by GBs. Dislocations within a grain and near a GB will interact with the latter, according several scenarios. Figure I.4 gives an overview of several main mechanisms of dislocation-GB interactions. Note that the normal to the GB plane is labeled $\mathbf{n_{GB}}$. The pile-up of dislocations in grain A, in the vicinity of the GB (Figure I.4.a), leads to several cases:

- Figure I.4.b: activation of sources leading to dislocation emission in grain B and in the GB;
- Figure I.4.c: dislocation dissociation at GB without any dislocation emission in grain B. Nevertheless, it can be followed by emission of dislocation in grain

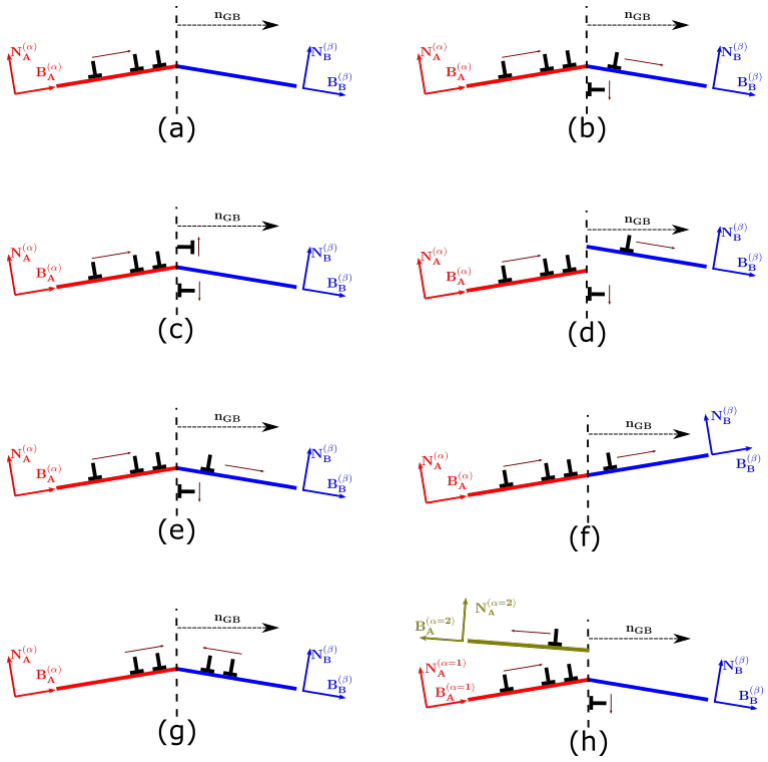

Figure I.4 – Schematics of several mechanisms of interaction between dislocations and a GB for grains A and B (adapted from [21]). $\mathbf{n_{GB}}$ is the normal to GB plane; $\mathbf{N}_{\mathbf{A,B}}^{(\alpha,\beta)}$ and $\mathbf{B}_{\mathbf{A,B}}^{(\alpha,\beta)}$ are respectively the normal to the slip plane and the slip direction.

B (Figure I.4.d);

- Figure I.4.e: transfer of a dislocation from the pile-up in grain A to grain B, leaving residual dislocation at GB, because of continuity of Burgers vector. In the ideal case (Figure I.4.f), the dislocation is transfered integrally without any residual dislocation;

- Figure I.4.g: absorption of dislocations coming from both grain A and grain B, and dislocation emission at GB;

- Figure I.4.h: reflection towards grain A of a dislocation coming from grain A, leaving a residual dislocation at GB.

Of course, mechanisms in Figure I.4 are summarized in a simple manner. More complex mechanisms include, for instance, dislocation absorption at GB by dislocation dissociation. Moreover, the active mechanism (note that several can be

activated simultaneously, as well) not only depends on grain misorientation and the GB nature but also on the type of dislocations (*i.e.* edge, screw or mixed). For example, screw dislocations, can glide through GBs without residual dislocation [21]. GB can act as dislocation source. Such dislocations remains generally in the vicinity of the GB and they can be emitted in both adjacent grains afterwards.

Concerning slip transfer rules, several criteria were proposed. A comprehensive overview is presented in [21]. Briefly, they can be classified into two main categories:

- crystallographic criteria such as slip plane normals and slip directions for active slip systems in both adjacent grains [22–26];
- weight-function-based criteria combined with crystal plasticity output parameters: they are based on the above-factors and they are obtained by the summation over all slip system transmission factors and weighting each one with plastic slips or the SCHMID factors [27].

I.1.2.3 Micromechanical modeling

It is clear that the response of one grain of interest in a polycrystalline sample cannot be understood individually without taking into account its neighborhood. Therefore, the stress field inside one grain ($\boldsymbol{\sigma}$) is not equal to the macroscopic stress field ($\mathbf{T}$), applied on the sample during the deformation test. Mathematically, the problem consists in calculating this local stress tensor ($\boldsymbol{\sigma}$) from polycrystal plasticity models, and then writing it in the crystal frame:

$$\boldsymbol{\sigma}^{(c)} = \mathbf{R} : \boldsymbol{\sigma} : \mathbf{R}^{\top} \tag{I.7}$$

where $\mathbf{R}$ and $\mathbf{R}^{\top}$ are respectively the rotation tensor and its transpose, characterizing the sample microstructure. Then, $\boldsymbol{\sigma}^{(c)}$ can be linked to $\tau_{RSS}^{(\alpha)}$ by $\mathbf{M}^{(\alpha)}$, written in the crystal frame, as well:

$$\tau_{RSS}^{(\alpha)} = \boldsymbol{\sigma}^{(c)} : \mathbf{M}^{(\alpha)} \tag{I.8}$$

Note that in the case of a monocrystal or for simple experimental considerations,

one generally supposes that the solicitation experienced by one grain is equal to that experienced by the all specimen:

$$\mathbf{T} = \boldsymbol{\sigma} \tag{I.9}$$

Therefore, the influence of the surrounding microstructure and the crystalline anisotropy are considered as negligible.

Two types of dislocation configurations are distinguished, of which both the density evolution and their specific interactions can be modeled [28]: Geometrically Necessary Dislocation (GND) densities result in a lattice disorientation of an elementary volume of reference in order to accommodate geometrically the deformation of the specimen (long-range effect). The other type of dislocations is called Statistically-Stored Dislocation (SSD) densities. They do not contribute to lattice disorientation but they can result in pinning of dislocations (short-range effect). Note that experimentally this distinction is mainly a question of resolution *i.e.* each dislocation can be seen as GND [29].

It is obvious that computational schemes need constitutive equations that have to be "fed" with experimental criteria and parameters, capturing the important operative mechanisms [30–36]. Experiments at mesoscopic scale, can bring new light both on our knowledge on polycrystal plasticity and models at the grain scale. Indeed, they can feed numerical simulations for predicting mechanical response of polycrystals (strain hardening, ductility etc.), with respect to the evolution of dislocation densities inside the grains and their interactions with GBs.

Modeling tools include for instance Discrete Dislocation Dynamics (DDD), Crystal Plasticity models using Finite Elements or Fast Fourier Transform algorithms (CPFEM, CPFFT), or mean field approaches (*e.g.* Self-Consistent models like ViscoPlastic Self-Consistent VPSC, Elasto-ViscoPlastic Self-Consistent EVPSC schemes) [37]. Recent studies have been carried out, which aim at coupling models (especially CPFFT) to experiments [38–41]. Such approaches can provide information on textures, GND density patterning, plastic strain localization and transfer across GBs, etc. Among the results, such coupled modeling-experimental methods show importantly, that it is possible to connect the evolution of microstructures to their

stress-strain state.

Through the previous overview, it is clear that the deformation of materials is a multiscale and a statistically complex problem of neighborhood (Figure I.5). Multiscale, because we have to be able to understand the plasticity at every scale where it takes place. Complex because the surrounding microstructure influences the response of the grain, and the combination of all grains gives the macroscopic behavior. On one side, the macroscopic response of a sample is known; on the other side, the operating mechanisms within the grain are well characterized. Knowing what happens in between is very challenging. Moreover, we have no idea whether the reported mechanisms are anecdotal or not, because of low statistic of observations.

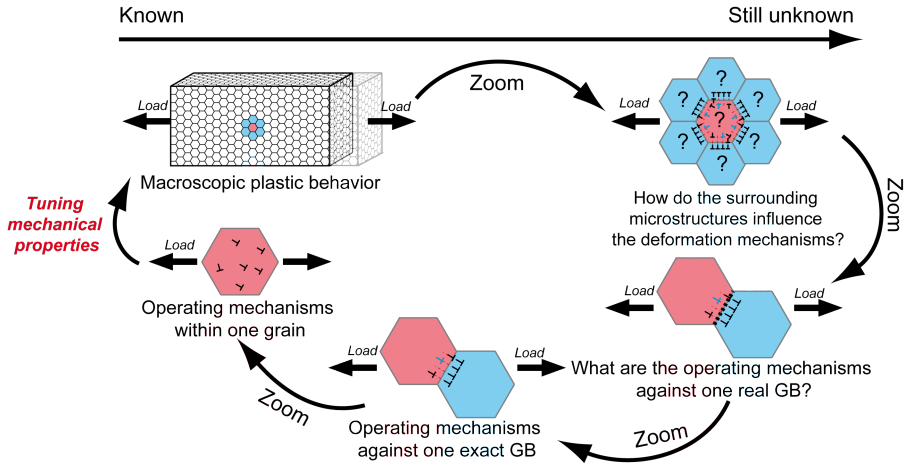

Figure I.5 – Overview of polycrystalline plasticity.

It is true to say that several laws or models were already proposed. In several cases, they have proven their efficiency for predicting, which operating mechanisms will be activated but there are even more cases where they simply do not work. One example is the case of MAX phases. Studying their fundamental deformation mechanisms was the heart of my doctoral work at Pprime Institute (2010 – 2013).

I.2 Effect of microstructure anisotropy on deformation mechanisms: case of MAX phases

I.2.1 Presentation of MAX phases

In the 90s, the research work of Barsoum *et al.* from Drexel University (Philadelphia, USA) led them to focus on Ti_3SiC_2 [42]. They showed that this compound is stiff, lightweight, machinable, made from relatively inexpensive raw materials, resistant to oxidation and thermal shock, and capable of remaining strong up to temperatures above 1300 °C in air. They synthesized about fifty compounds with the same range of promising properties. Because of their composition, Barsoum *et al.* called these remarkable materials $M_{n+1}AX_n$ phases, where [43, 44] (Figure I.6):

- M is a transition metal from the groups 3 (Sc), 4 (Ti, Zr, Hf), 5 (V, Nb, Ta) or 6 (Cr, Mo);
- A is an element from the groups 12 (Cd), 13 (Al, Ga, In, Tl), 14 (Si, Ge, Sn, Pb), 15 (P, As) or 16 (S);
- X is carbone C and/or nitrogen N.

n is an integer from 1 to 3, therefore the structures M_2AX, M_3AX_2 and M_4AX_3 are respectively called 211, 312 and 413.

Figure I.6 gives a non-exhaustive list of thermodynamically stable MAX phases. All of them are not yet synthesized to date. However, a large number of solid solutions on M, A and X sites were obtained. They enable to modify or even to tune properties.

MAX phases have a laminated structure with an hexagonal lattice (space group: P63/mmc). The primitive cell can be described as a stacking of n M_6X octahedron layers with one layer of A element (Figure I.7). Furthermore, measurements of lattice parameters with numerous methods reveal that MAX phases exhibit an elevated crystalline anisotropy. The c/a ratio is generally higher than 3 [45]. MAX phases synthesized by powder metallurgy are polycrystalline bulk samples with random grain orientations. It is commonly observed that during synthesis grains grow

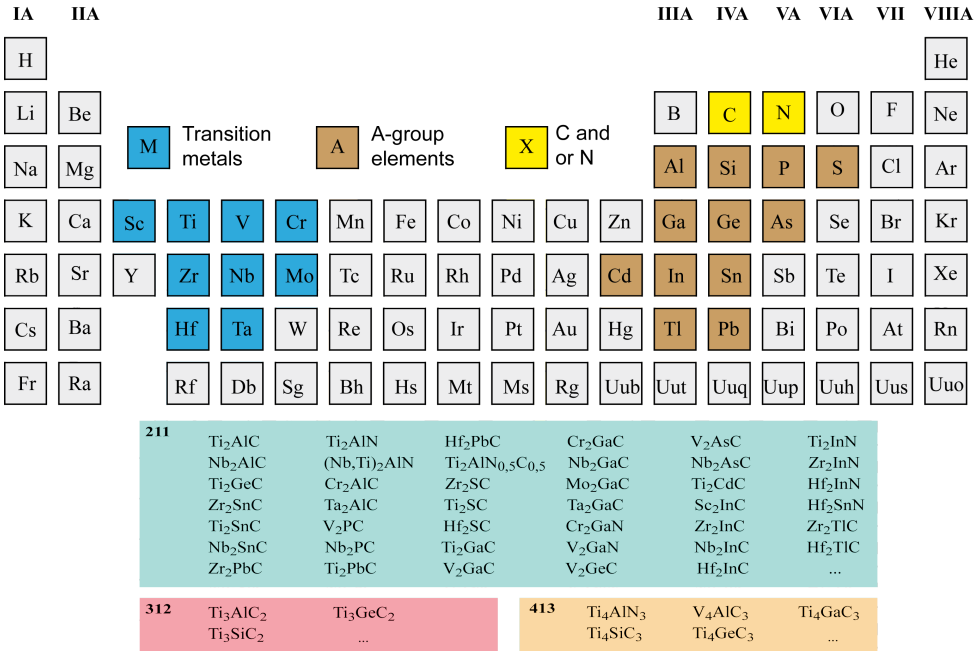

Figure I.6 – The main stable MAX phases. Adapted from [44].

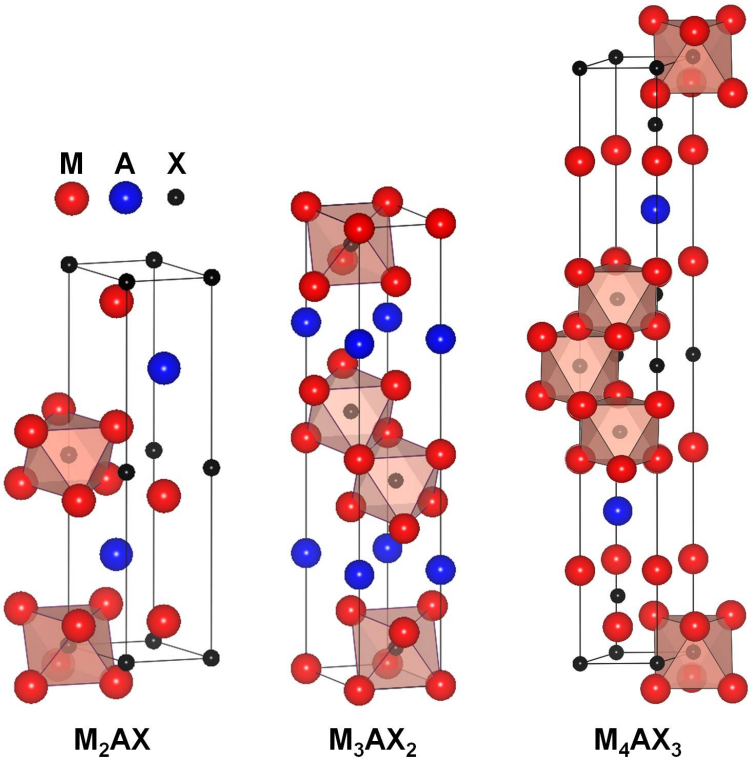

Figure I.7 – The three primitive cells (211, 312 and 413).

in platelet shape. Because of the high crystalline anisotropy, platelet lengths are parallel to basal planes [46]. Therefore, projections on the surface are observed as

rectangles with a high aspect ratio (Figure I.7).

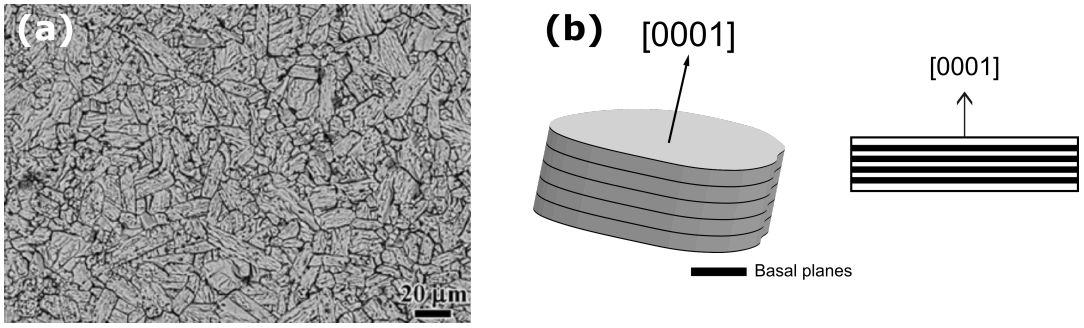

Figure I.8 – Grain shape in MAX phases: (a) Scanning electron microscope micrograph of Ti_2AlN [47]; (b) schematic of the platelet shape.

The technological impact of these ternary compounds does not derive from any single property but rather they achieve a unique combination of properties. Indeed, they combine properties of both ceramics (refractory, high stiffness, low density – $4.5\,g\,cm^{-3}$ for Ti_3SiC_2 [44] –, low ductility at room temperature) and metals (high thermal and electric conductivity, thermal shocks resistance, mechanical resistance). Moreover, several composites of MAX phases and metals allow to elabor complex microstructures for optimizing several properties (electricity, hydrogen storage, etc.) [48–50]. But before any industrial exploitation, it is crucial to shed new light on comprehension of deformation mechanisms of these promising materials.

I.2.2 Overview of deformation mechanisms of MAX phases

MAX phases exhibit a Brittle-to-Ductile Transition (BDT) around 800 °C which leads to failure after a very limited plastic regime at room temperature [43, 52]. A very intriguing behavior is observed, when MAX samples are subjected to load-unload cycles in the elastic regime: reversible hysteretic loops are recorded [53]. These features are illustrated by the compression stress-strain curve shown in Figure I.9 obtained on Ti_2AlN MAX polycrystal [51]. The formation of open loops suggests an energy dissipation process, although in the elastic regime: a "Kinking Non-linear Elastic" (KNE) model has been developed involving Incipient Kink Bands (IKBs) that are entities composed of dislocation loops lying in parallel basal planes and stacked on top of each other (Figure I.10) [54]. The IKBs are supposed to

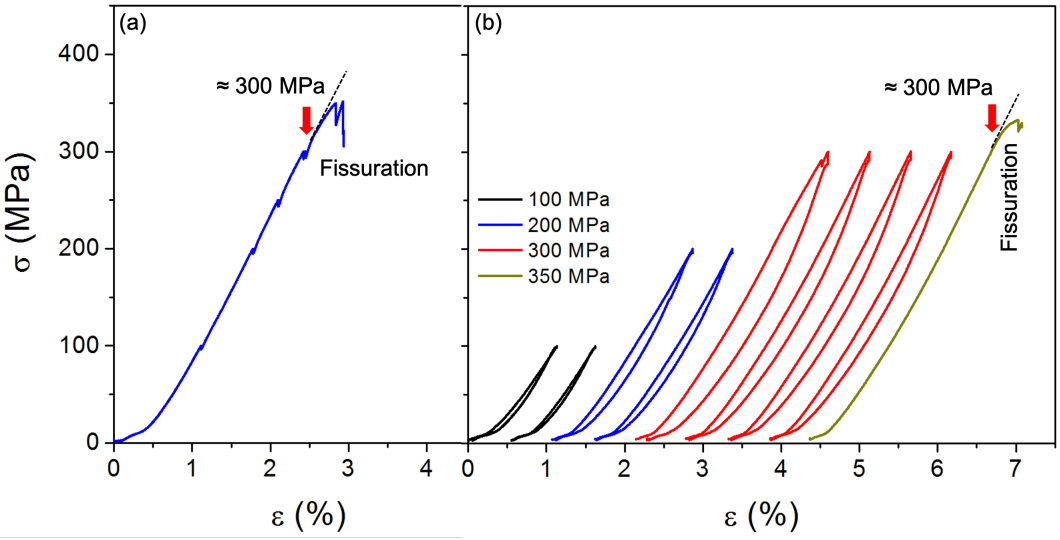

Figure I.9 – Stress-strain curves of Ti_2AlN [51]. (a) monotonous loading; (b) cycled loading.

nucleate and expand when load is applied and to collapse when load is removed. This "reversible" dislocation-based micro-mechanism is invoked to explain the above-mentioned energy dissipation observed in the elastic regime and the formation of Kink Band (KB) [53, 54]. KBs give rise to misorientation of the lattice with a so-called "stovepipe" shape [55, 56]. For high deformation, KBs lead to buckling and delamination cracks within individual grains [57]. Besides the fact, that IKBs have never been observed, the observation of open-loops at very low stress somehow contradicts this model involving a critical shear stress needed to overcome the energy barrier associated to dislocation nucleation. In addition, a mechanism, based on atomic-scale ripples in basal layers, called "ripplocation" has been recently invoked for explaining kinking in MAX phases, essentially from atomistic simulations [58, 59].

However, an aspect for understanding the mechanical behavior of MAX phases is that MAX polycrystals, fabricated by powder metallurgy techniques, exhibit very anisotropic microstructure with grains being highly elongated in the basal plane direction [60]. Considering this feature of MAX phases, it has been shown, by *in-situ* deformation coupled with neutron diffraction and microscopy observations that the MAX polycrystal can be described as an ensemble of soft and hard grains leading to a high local concentration of non-uniaxial stresses at GBs [51] (Figure I.11).

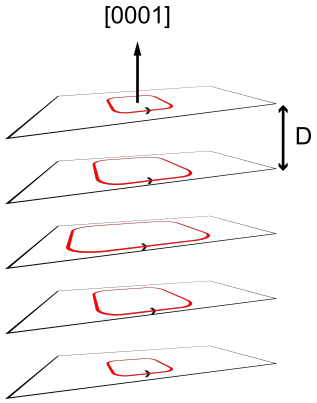

Figure I.10 – Scheme of Incipient Kink Band. Adapted from [53].

The reversible hysteretic behavior can therefore be explained by this microstructure anisotropy and the associated BAUSCHINGER effect [61], *i.e.* within the classical framework of crystal plasticity in polycrystals [51]. In other words, MAX phase deformation mechanisms usually explained by the IKB model – the reversible hysteretic loops observed, when MAX polycrystals are subjected to elastic load-unload cycles – can be as well explained by the complex response of the very anisotropic microstructure that generate strong variations of microstrains in all grains, even in the elastic regime [51].

It is well established that deformation at room temperature involves dislocation movement [54, 62]; these dislocations are $\langle a \rangle$-type basal dislocations ($\overrightarrow{b} = \frac{1}{3}\langle 1\,1\,\bar{2}\,0 \rangle$) and glide in the basal plane forming large dislocation pile-ups and walls [54, 60]. The latter may interact to form pairs of low-angle tilt GB (or kink boundaries) [57]. According to the KB formation model, mechanical properties of MAX phase materials is thus mainly ascribed to basal plane dislocations, which are able to freely glide without dislocation reactions, allowing dislocation wall formation [53]. Out-of-basal-plane dislocations have been observed by TEM in as-grown Ti_4AlN_3 [63] and in Ti_3SnC_2 [64]. These dislocations do not play a key role in the plastic deformation at room temperature in standard deformation conditions. On the contrary, numerous dislocation dipoles, alignments, nodes have been observed in room-temperature-deformed Ti_2AlN [62]. Such dislocation reactions may result in the formation of dislocation cells, as observed in Figure I.12 [62]. The presence of dislocation interactions and networks has to be considered in the comprehension of

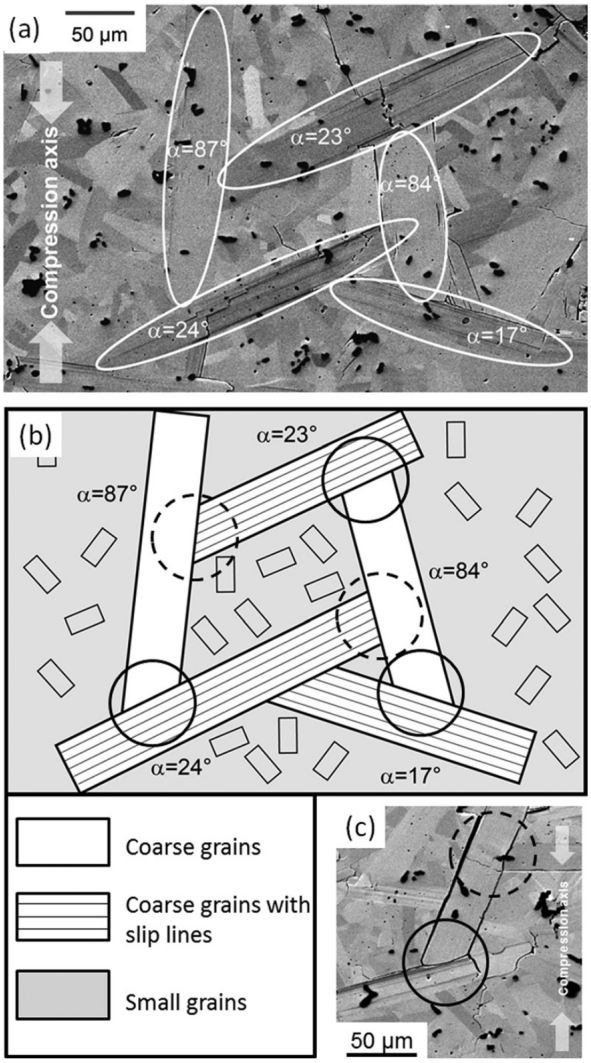

Figure I.11 – *Post-mortem* observations of the surface of Ti_2AlN deformed at room temperature and a schematic of the microstructure [51].

the deformation mechanisms. Dislocations were also observed to align along specific directions leading to segments with screw, 30°, 60° or edge character, indicative of an elevated lattice friction [62, 65]. In addition, it has been recently reported that the specific stacking of M_6X octahedrons and A-element layers is at the origin of non-SCHMID effects [66].

At high temperature, it has been observed that out-of-basal-plane dislocations are not anecdotal events and therefore cross-slip plays a key role in the deformation (see Figure I.13) [67]. This increase of available glide systems (basal, prismatic and pyramidal planes) is likely to promote significant ductility at high temperature.

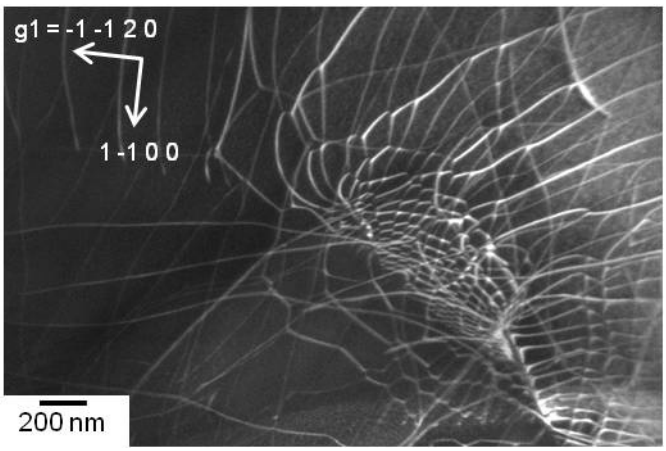

Figure I.12 – Dislocation network observed in Ti_2AlN deformed under confining pressure at room temperature [62].

These major changes in the plasticity mechanism are expected to play a key role in the appearance of the BDT with temperature notably with respect to the decrease of the yield strength with increasing temperature [67]. Note also that evidences of FRANK partial $\langle c \rangle$-dislocations associated with a diffusion mechanism of Cu into Ti_2AlC were recently reported in Ti_2AlC [49]. Such crystalline defects were not expected to be found in such material, because of energetic reasons due to the high c/a ratio.

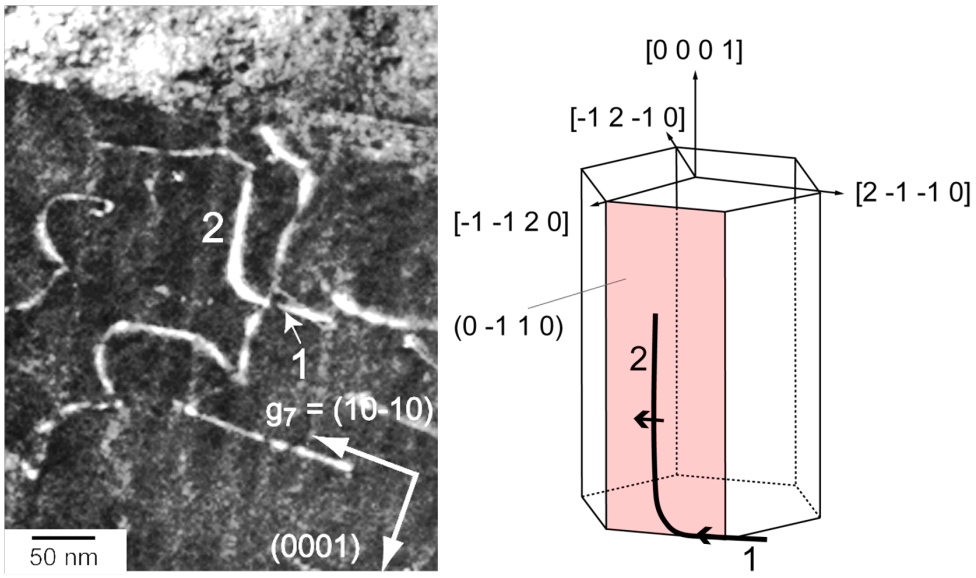

Figure I.13 – Cross-slip observed in Ti_2AlN deformed under confining pressure at 900 °C. Adapted from [67].

I.3 Towards the influence of strain-path changes on metal plasticity

This part briefly summerizes the research done during my 20 months of postdoctoral fellow (2014 – 2015) at Paul Scherrer Institut (PSI) in Switzerland. My research was the first part of the ERC Advanced Grant of Prof. Helena Van Swygenhoven (MULTIAX).

I.3.1 Strain-path changes

For some metals, plastic strain increases the stress required to continue the deformation. This phenomenon is called strain hardening. But when deformation is stopped, reversed or continued in other direction, the situation becomes more complex and less predictable. One could expect that a dislocation pile-up created during the first straining direction might partially or fully relax. Subsequent straining in another direction will cause new dislocation pile-ups. Therefore, it has become clear that the strain path can have important influences on the microstructural evolution. Because the structure-property relation is multiscale, an in-depth understanding requires a multiscale experimental approach. Such was the background of my postdoctoral research. Our main objective was to investigate what happens in metallic materials if the strain occurs in different directions or changes during deformation. Such questions could not be clarified using previously available methods and are for instance important for the production processes in the automotive sector. Furthermore, the project also developed new methods that can be used to study materials at large-scale facilities, such as the Swiss light source at the PSI.

I.3.2 Development of a novel biaxial machine

Most of the knowledge on mechanical behavior has been derived from conventional uniaxial tests. However industrial production of metallic components consists in many strain-path changes, which modify drastically their mechanical response. In

this framework, *in-situ* experiments can give valuable insights on deformation mechanisms which could appear or could be modified during strain-path changes.

In-situ mechanical testing under x-ray powder diffraction has become a frequently applied research method to study elastic and plastic anisotropy of metals, the evolution of microstructure and intergranular stresses, load transfer in multiphase materials, mechanical driven phase transformations etc... By taking the lattice as a strain gauge *i.e.* using the position of the Bragg peaks, the evolution of lattice strain is measured for individual grain families averaged over thousands of grains [68]. A few decades ago, *in-situ* mechanical testing was usually performed using optical microscopy. However, the low resolution and the small depth focus of optical instruments limit its suitability for micromechanical tests. Consequently, *in-situ* SEM observations are becoming indispensable for studying the evolution of surface microstructures during the experiments, giving complementary insights on mechanical behavior of the samples.

With the on-going miniaturization of engineering components there is an increasing need for novel deformation devices that can handle samples below the micrometer scale. For simple uniaxial deformation a variety of such devices has been developed in recent years. For instance, many test rigs for *in-situ* SEM and TEM observations are currently available on the commercial market. While *in-situ* miniaturized uniaxial deformation setups are nowadays relatively common, miniaturized multi-axial deformation devices are less frequent yet. For instance, there exist only few biaxial tensile set-ups combined either with SEM observations [69] or coupled with x-ray reflection diffraction [70, 71]. But there are none that combine nanometer scale deformation with *in-situ* microscopy observations or with synchrotron x-ray diffraction on small bulk materials.

My postdoctoral work consisted in the development of a new miniaturized *in-situ* biaxial deformation machine, which is not only compatible with synchrotron lines (transmission and reflection modes) but also with SEM observations (see Figure I.14). The latter allows to *in-situ* access an area of interest by digital image correlation. To face this technological challenge, different techniques have been de-

veloped. In particular the thinning of cruciform samples by pulsed laser ablation with ultra-short pulses (from the femtosecond to the picosecond) [72]. This new strategy essentially has the advantage of machining samples while minimizing damage, which makes it an excellent alternative to the focused ion beam milling.

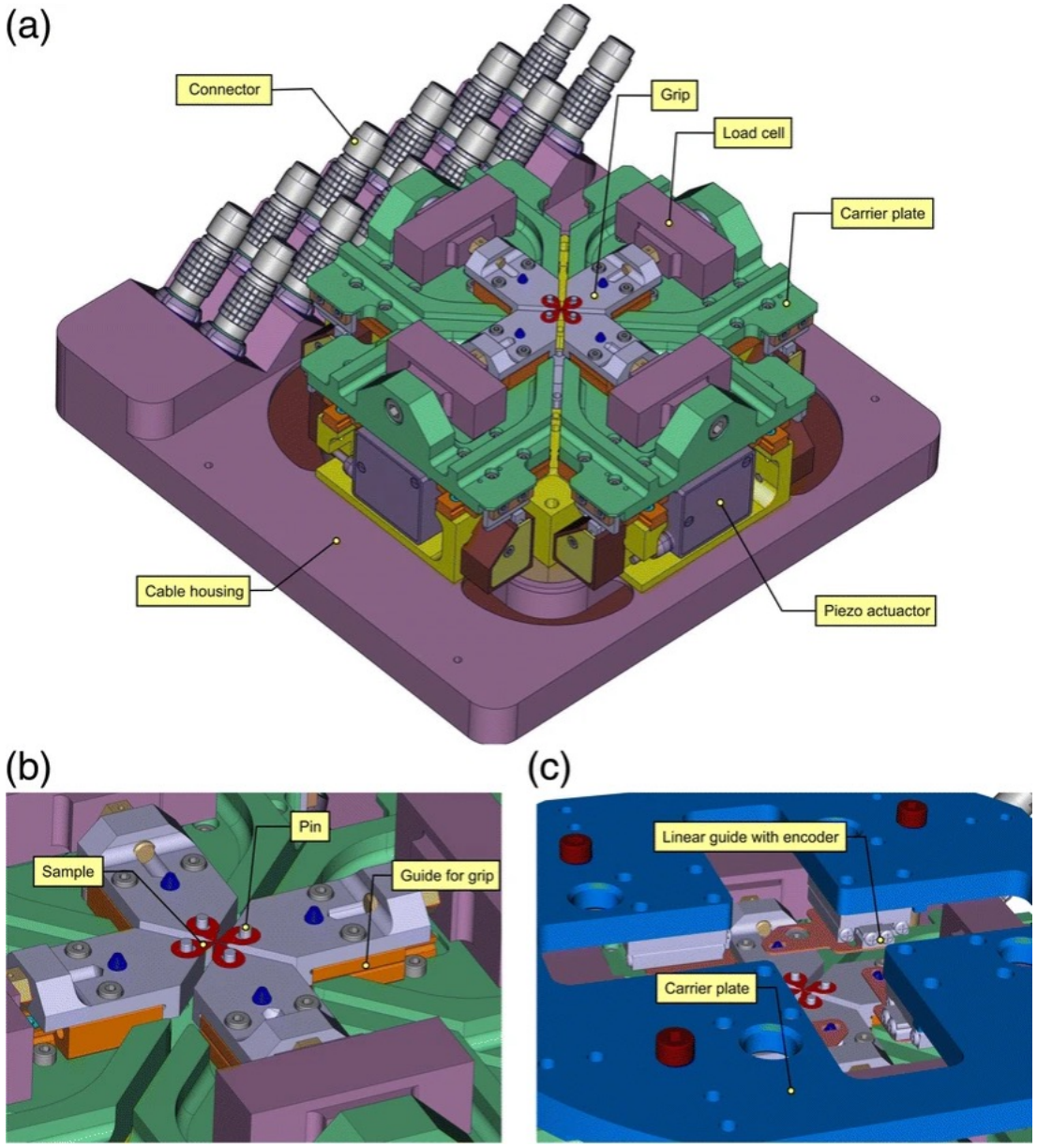

Figure I.14 – Schematic design of the *in-situ* biaxial deformation rig. From [73].

Such development was very challenging because of numerous constraints. Finally, it was a success in its own. The proof-of-principle was obtained at the end of my postdoctoral stay. Our *in-situ* x-ray diffraction experiments revealed that the

developed rig operates successfully [73]. This opened up new research frontiers on complex biaxial strain path changes and the continuation of the ERC project of Prof. Helena Van Swygenhoven.

Chapter II

Contribution of electron microscopy

Mechanical tests followed by microstructural investigations provide information to computationally predict mechanical performances of components. Electron microscopy is one of the most well-known techniques for analyzing deformation features of materials for allowing to understand their response to exterior solicitations. Two kinds of electron microscopes are generally used and bring complementary information: at macro/meso-scopic scale, the SEM [74] and at micro/nano-scale, the TEM [75].

II.1 Overview of electron microscopes

II.1.1 Transmission Electron Microscope

The TEM is one of the most well-known techniques for both observing and characterizing dislocations on one hand, at the sub-micron, and on the other hand, at the nano-scale, and more generally deformation defects in electron transparent thin foils (thickness of $\approx 100\,\text{nm}$ [76]). Preparation of such a thickness is both an art and a science. It needs devising suitable methods, as well as realizing/demonstrating them in a defined process with reproducibility. Also, utmost care is necessary in preparing and handling specimens, as they are extremely thin and hence prone to bending and breaking.

Determining the Burgers vector $\overrightarrow{b}$ of dislocation consists in obtaining two diffracting vectors (or $\overrightarrow{g}$) that put the observed dislocations out of contrast by tilting the lamella (necessary and sufficient condition) [75]. Mathematically, extinction

conditions for a dislocation are given by [75]:

$$\vec{g} \cdot \vec{b} = 0 \; ; \vec{g} \cdot \left(\vec{b} \times \vec{u} \right) = 0 \tag{II.1}$$

The line direction $\vec{u}$ is defined as the intersection of non-parallel planes containing the dislocation. It can be determined from the observations of the dislocation in different orientations of the thin foil. Note that for a stacking fault with $\vec{R}$ as fault vector, the extinction condition is [75]:

$$\vec{g} \cdot \vec{R} = 0 \tag{II.2}$$

Such after-deformation or *post-mortem* comprehensive dislocation studies at microscopic scale bring valuable information for extrapolating to the macroscopic response of materials and they can feed advanced numerical multiscale models [49, 65].

Among the difficulties encountered, here is that most of our detailed knowledge has been extracted from *post-mortem* observations. *In-situ* mechanical testing combined with TEM is required for studying the instantaneous evolution of defects during exposure to stress. Such an experiment allows capturing footprints of deformation mechanisms responsible for the changing microstructure [77–80]. Although various approaches of mechanical testing inside a TEM exist today [77–79], *in-situ* TEM mechanical testing is experimentally very tough [81]. In addition to the difficult control of deformation conditions, the space available is generally less than one centimeter and statistics on physical mechanisms is very weak. TEM needs an electron transparent specimen with a thickness of $\approx 100\,\text{nm}$ with a useful field of view of few μm^2. It is usually said that if one is able to assemble all zones studied by TEM since its development in the forties, they would not even fill a thimble. Therefore, fundamental questions on the representativeness of observed phenomenon must be raised, when extrapolating discussions to a millimeter-size specimen.

II.1.2 Scanning Electron Microscope

Unlike TEM described in the previous part, SEM can both image and analyze bulk samples. Various information can be deduced from the analysis of signals (electrons and photons) emitted by the sample through the electron-matter interaction and coming from different depths. The affected volume is called "interaction pear" [74].

II.1.2.1 SEM imaging

Information on surface topography is provided by Secondary Electrons (SE), their energy is low. SE detectors are located either in the column or in the chamber. BackScattered electrons (BSE), with an energy comparable to the primary beam, give crystallographic information and they are linked to the chemistry of the material. They are used to generate orientation or even phase contrast micrographs on mirror polished sample.

II.1.2.2 Electron backscatter diffraction

Electron BackScatter Diffraction (EBSD) is a SEM technique providing quantitative microstructural information on the crystallographic nature of most crystalline materials (metals, minerals, semiconductors, ceramics). It enables to determine crystallographic orientations, grain size, misorientations at GB and the different phases of the material [82–85]

The sample is mounted in the SEM chamber, where the primary beam of electrons is focused on the studied area. The BSEs within the sample will be diffracted, if they are in Bragg incidence with the reflecting planes. For $\{h\,k\,l\}$, electrons diffract according to two diffraction cones, which are symmetrical with respect to the $(h\,k\,l)$ plane. The projection of these cones on the phosphorescent screen of the EBSD camera produces quasi-parallel hyperbolic lines similar to straight lines forming a band of Kikuchi [86]. The median axis of this band corresponds to the trace of the $(h\,k\,l)$ plane. The band pattern generates a diagram of Kikuchi, where angles between bands correspond to angles between crystal planes. Thus, automatic indexing of this diffraction pattern enables to determine crystallographic orientation

of grains. It should be noted that the sample is tilted at 70° from the horizontal in order to optimize the BSE yield.

Each point or area of the sample, impacted by the electron beam, produces a KIKUCHI pattern related to its crystallographic orientation. Recent cameras and acquisition software allow recording about 1600 points per second, making EBSD the fastest method for determining crystallographic orientation. In terms of resolution, EBSD has a spatial resolution between 20 and 70 nm. This resolution depends on the material and the accelerating voltage of the electrons. For example at 20 kV, it is around 50 nm for steel. Concerning angular resolution, it is approximately 0.05° (Oxford Instruments System). However, EBSD is limited in absolute angular resolution: the orientation of the crystal relative to the optical axis of the microscope is given from 1° to 2° [87]. This uncertainty is due to the specific geometry the technique (sample inclination at 70°).

In addition, one of the advantages of EBSD is the measurement of local misorientation, from which it is possible to estimate GND density [29, 88, 89]. The latter can be represented in the form of a map. GND density, ρ_{GND}, is calculated by:

$$\rho_{GND} = \frac{C\beta}{\| \overrightarrow{b} \| \delta x} \tag{II.3}$$

where

- C is a constant;
- β is the misorientation;
- δx is the step size used for the mapping.

II.2 From electron channeling contrast imaging to accurate electron channeling contrast imaging

Full characterization of crystalline defects is not only possible by performing TEM experiments on thin foil samples. SEM can access diffraction contrast on bulk materials with the phenomenon of electron channeling [74].

Electron channeling is due to electrons that channel down crystal planes *i.e.* paths, where electrons can penetrate to a higher depth before scattering (Figure II.1). Some orientations of the crystal will backscatter more electrons than others, giving rise to orientation contrast.

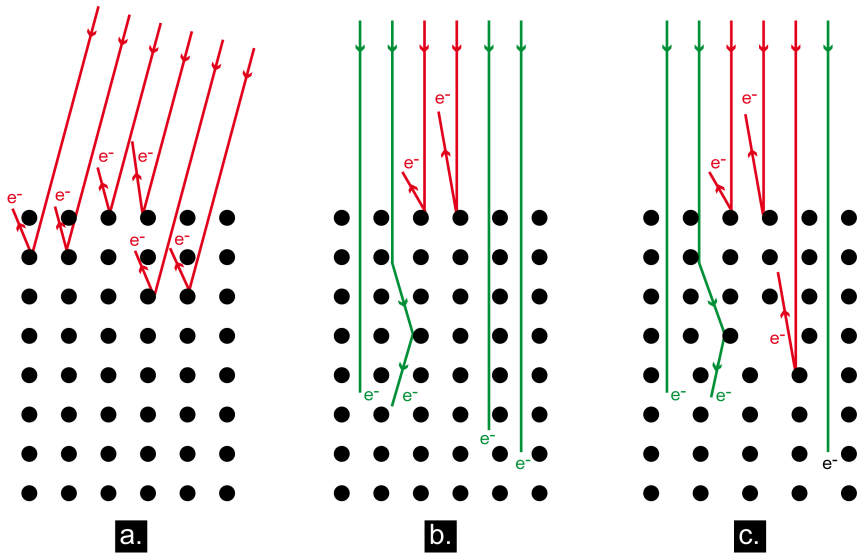

Figure II.1 – **a.** Closed channel (red); **b.** open channel (green) and **c.** conversion of an open channel to a closed channel.

Electron Channeling Contrast Imaging (ECCI) is a powerful technique for observing and characterizing defects in crystals. It is based on the fact that the yield of BSE depends drastically on the orientation of the crystal relative to the incident electron beam *i.e.* optic axis of the SEM. ECCI requires the crystal orientation to be controlled relative to optic axis in the range of 0.1°.

Historically, since the first observation (see Figure II.2) in 1967 by Coates of the so called Electron Channeling Patterns (ECP) – Kikuchi-like bands – formed by

BSE collected at low magnification on a single crystal, these patterns were used to determine precisely the orientation of the crystal of interest with accuracies in the range of 0.1° [90]. In the same year, Booker *et al.* proposed that by orienting the crystal in the SEM close to the BRAGG condition (the so-called two beam conditions) for a set of planes, one can contrast defects, such as dislocations, stacking faults etc. in the near surface region of bulk samples [91]. However, due to their poor spatial resolution (about a millimeter) ECPs cannot be collected from small grains of a polycrystalline material. For these reasons, many groups limited ECCI characterization to single crystals such as GaN, SiC [92, 93].

Figure II.2 – First ECP reported by COATES on Ge, when the bulk specimen was tilted 10° and −10° from the {1 1 1} direction. From [90].

The collection of Selected Area Electron Channeling Patterns (SACPs) obtained

by rocking the incident electron beam at a point on the surface of a given grain of the sample, first suggested by Coates, opens the way to characterize defects with individual grains in polycrystalline materials. However, in practice this point corresponds to an area of several microns, excluding ECCI characterization of small grains. Moreover, most of FEG-SEMs, until very recently, no longer offer the ability to rock the beam and so to collect SACPs.

Due to these limitations, the ECP/SACP technique has been over-shadowed by the development of EBSD pattern analysis, which offers high spatial resolution (about 30 nm) and very high data acquisition rates. Nevertheless, EBSD provides orientations on high tilted crystals (about 70°), and does not readily give the orientation with respect to the incident beam, which leads to absolute angular resolution limited to about 1°-2° [87]. This makes it difficult to set up specific channeling conditions and thus to observe defects with high contrast and carry out quantitative studies.

Despite this, an alternative approach using EBSD orientation analysis to predict the specimen stage tilts and rotations necessary to bring a crystal into optimum channeling conditions, known as Controlled Electron Channeling Contrast Imaging (cECCI) [94]. However, due to EBSD uncertainties, the exact deviation from the Bragg condition cannot be assessed and it remains difficult to achieve optimum contrast of defects.

To overcome these challenges, Guyon *et al.* developed an innovative procedure for rocking the electron beam on the high resolution Gemini electron column (Zeiss Auriga 40 FIB SEM), which has no dedicated SACP mode (Figure II.3) [95]. A SACP pivot point was created by combining control of the aperture alignment coils and the scanning coils of the SEM, using them in a manner quite different from their primary functions. Moreover, for the first time collection of SACPs from sub-micron sized areas was demonstrated, with a spatial resolution of 500 nm at a practical working distance of 10 mm (Figure II.4) [96].

Using this High Resolution-SACP (HR-SACP) tool combined with simulated EBSD patterns (Figure II.4), direct and precise channeling conditions for ECCI

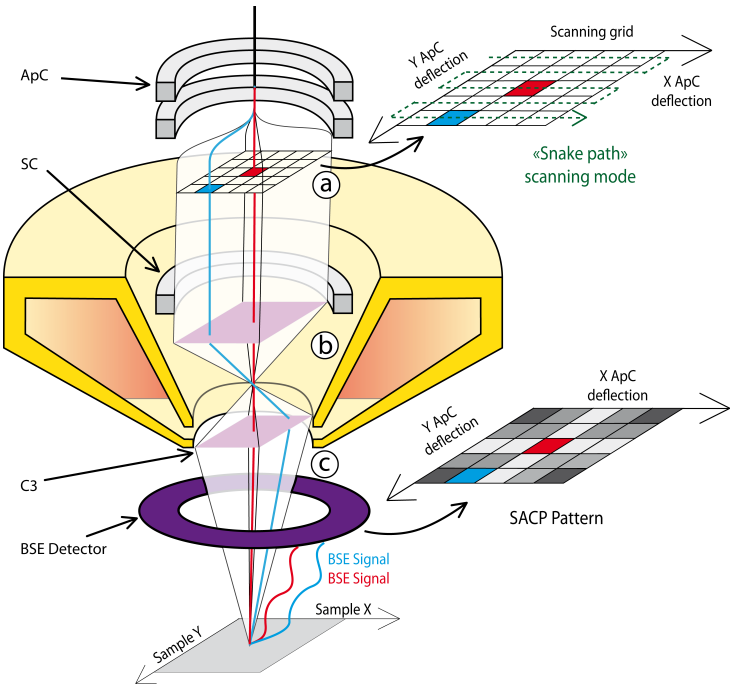

Figure II.3 – Gemini column cut scheme showing all the deflections that result in the beam rocking necessary for SACP collection. (a) Double deflection in the Aperture alignment Coils (ApC) results in beams parallel to the optic axis. (b) Deflection of the off-axis beam by the magnetic field of the Scanning coils (SC) and correction using the beam shift control to center the beam on sample pivot point. (c) Backscattered information collection and construction of the BSE map intensity according to the position on the ApC scanning grid. Distances between elements are not representative. From [95].

can be obtained via specimen stage tilts and rotations allowing to carry out TEM style contrast analysis for dislocation characterization in fine grained bulk materials [96, 97]. The first results obtained using this HR-SACPs assisted Accurate-ECCI (A-ECCI) new procedure, are illustrated in Figure II.4, where dislocations in fine-grained 2% Si IF-Steel were characterized in terms of Burgers vectors and line directions.

Recently, another promising ECCI procedure was reported: the Rotational ECCI [98]. It consists of acquiring series of BSE micrographs during the rotation of the sample. It facilitates fast observations of crystalline defects by imaging them with several channeling conditions.

In conclusion, it should be noted that only defects near the surface (around 100 nm deep) are observable. Consequently, ECCI offers the ability to execute diffraction contrast imaging inside a SEM, removing all of the limitations imposed

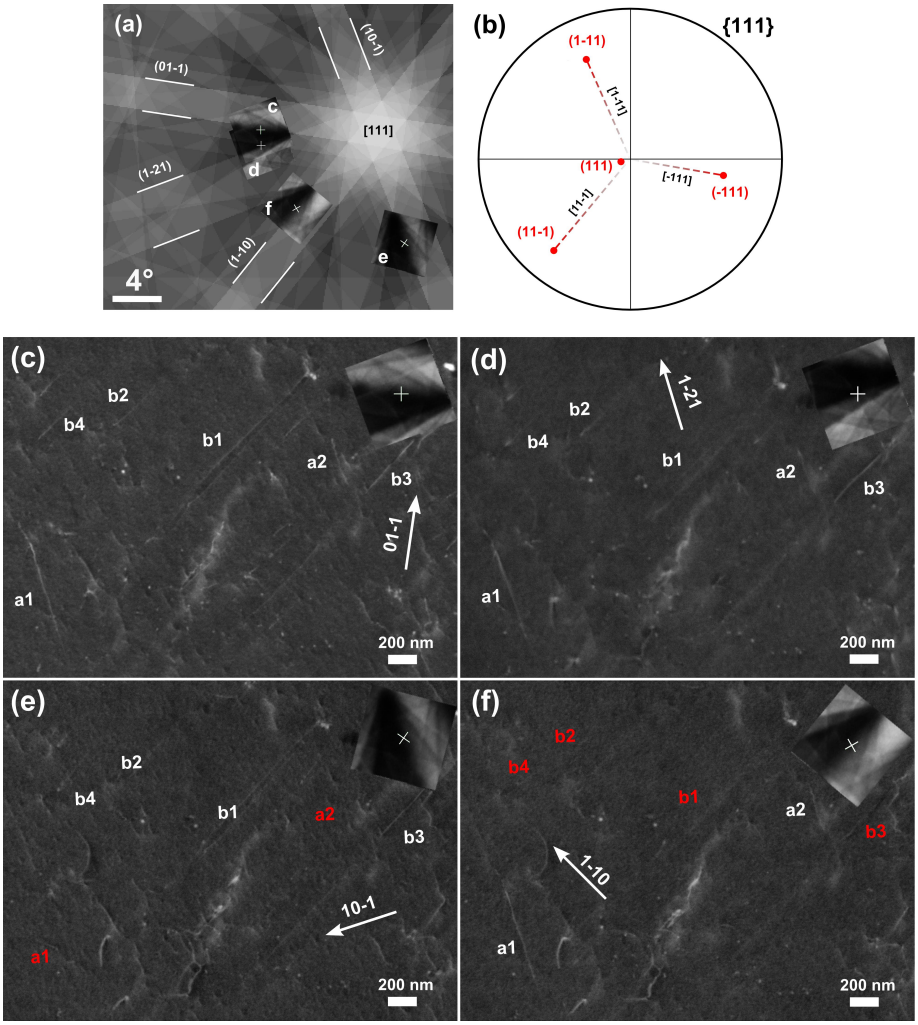

Figure II.4 – Characterization of dislocations in a grain of the 2% Si IF-steel. (a) Four HR-SACPs superimposed on a simulated EBSD pattern. (b) Stereographic projection showing the $\{1\,1\,1\}$ poles. The fading dotted lines represent the directions of the inclined $\langle 1\,1\,1\rangle$ screw dislocations and show how the channeling contrast from screw dislocations with these three $\langle 1\,1\,1\rangle$ line directions will decrease as the dislocations extend below the sample surface. (c–f) ECC micrographs of dislocations collected using the four channeling conditions shown in (a): (c) $\vec{g} = (0\,1\,\bar{1})$; (d) $\vec{g} = (1\,\bar{2}\,1)$; (e) $\vec{g} = (1\,0\,\bar{1})$; (f) $\vec{g} = (1\,\bar{1}\,0)$. Two dislocation line directions corresponding to $\vec{u} = \vec{b} = [1\,\bar{1}\,1]$ (dislocations a) and $[1\,1\,\bar{1}]$ (dislocations b) are seen. The dislocations are labeled in red where they disappear. From [96].

by TEM analysis with still sufficient imaging resolution to analyze individual dislocations.

Chapter III

Physics of ECCI and optimization of experimental conditions

This part briefly summarizes several theoretical results obtained during the doctoral work of Hana Kriaa (2015–2018). The objective is, on one hand, to improve the understanding of observed defect contrasts, and on the other hand, to optimize experimental conditions, to take maximum advantage of ECCI for capturing footprints of deformation mechanisms.

ECCI is based on the fact that the BSE yield depends on the orientation of the crystal relative to the incident electron beam *i.e.* optic axis of the SEM [91]. That is why, strain and defects, distorting crystal planes, produce changes in BSE intensity (I_{BSE}), leading to a contrast on a micrograph.

To understand the origin of ECCI contrasts, the dynamical theory of diffraction in 2-wave condition was adapted from the one of TEM [74, 75, 99]. Inside the crystal, electron beams are described by a superposition of Bloch waves. The different inelastic scattering events are divided into two categories: those scattered with angles (with respect to the incident beam) less than 90° (forward scattering) and those scattered at angles higher than 90° (back-scattering) [74]. In the multiple scattering model, the back-scattered and forward scattered wave are allowed to interact with each other.

By using the same model based on Bloch waves, simulations of I_{BSE} profiles done by Spencer *et al.* [100] and Wilkinson *et al.* [101] and their comparisons with experiments show that such profiles correspond to a white band with dark

edges, in the case of a perfect crystal. The same approach was also used by REIMER [74, 102] for a perfect crystal, where multiple diffusions are treated as incoherent.

III.1 Perfect crystal

In a crystal, the wave function Ψ is a solution of the time-independent equation of SCHRÖDINGER [103], where the atomic potential is written as a FOURIER series on the nodes, $\overrightarrow{h}$, of the reciprocal lattice [74]:

$$\nabla^2\Psi + \frac{2m_e}{\hbar^2}\left[E - \sum_h V_h \, \mathrm{e}^{2\pi \, \mathrm{i} \, \overrightarrow{h}\cdot\overrightarrow{r}}\right]\Psi = 0 \tag{III.1}$$

where:

- m_e: mass of an electron;
- E: kinetic energy of an electron;
- $\overrightarrow{r}$: position vector;
- V_h: complex FOURIER coefficients.

In the formalism of BLOCH waves, Ψ is given by [74]:

$$\Psi\left(\overrightarrow{r}\right) = \sum_i \varepsilon^{(j)} \sum_g C_g^{(j)} \, \mathrm{e}^{2\pi \, \mathrm{i}\left(\overrightarrow{k_0^{(j)}} + \overrightarrow{g}\right)\cdot\overrightarrow{r}} \, \mathrm{e}^{-2\pi q^{(j)} z} \tag{III.2}$$

where:

- (j) : the j-th wave;
- $\varepsilon^{(j)}$: excitation amplitude of the BLOCH wave $\Psi^{(j)}$;
- $C_g^{(j)}$: amplitude of diffracted waves with a wave vector $\overrightarrow{k_g^{(j)}} = \overrightarrow{k_0^{(j)}} + \overrightarrow{g}$;
- $\overrightarrow{k_0^{(j)}}$: wave vector of the j-th primary wave;
- $\overrightarrow{g}$: diffraction vector;

- $q^{(j)}$: attenuation parameter expressing the exponential attenuation of the wave amplitude with increasing depth z .

In order to determine the coefficients of the BLOCH function, in equation III.2, the two-beam condition is used *i.e.* only one set of planes is in channeling condition. Experimentally, such condition is satisfied when the incident beam is far from any intersections of pseudo-KIKUCHI bands [104].

The BSE signal of a slice of a thickness d z, located at a depth z, is given by [74]:

$$\frac{\mathrm{d}\,\eta}{\mathrm{d}\,z} = N\sigma_B \left[\Psi^*\Psi + \left(1 - \sum_j |C_0^{(j)}|^2\, \mathrm{e}^{-4\pi q^{(j)} z}\right)\right] \tag{III.3}$$

where:

- N: atom number per unit of volume;
- σ_B: cross section of backscattering;
- $\Psi^*\Psi$: probability for the BLOCH wave to be backscattered at a depth z;
- the last term in parentheses in equation III.3 describes the electrons that are removed from the BLOCH wave field by scattering before reaching the slice d z.

The BSE coefficient (η_{OC}) is proportional to I_{BSE}. It is obtained by integrating the equation III.3 in the total depth of interaction, *i.e.* between $z = 0$ and $z \to +\infty$. The subscript OC refers to the total I_{BSE} due to the orientation contrast, while both contributions due to atomic number and surface inclination are not taken into account [74]:

$$I_{BSE} \propto \eta_{OC} = \frac{N\sigma_B}{4\pi}\xi_0' \left(-\frac{\omega + \frac{\xi_0'}{\xi_g'}}{1 + \omega^2 - \left(\frac{\xi_0'}{\xi_g'}\right)^2} + \frac{\omega}{1 + \omega^2 + \left[(1+\omega^2)\,\frac{\xi_0'}{\xi_g}\right]^2}\right) \tag{III.4}$$

where:

- ξ_0' and ξ_g': absorption lengths;

- ξ_g: extinction distance;
- $\omega = s\xi_g = g(\theta - \theta_B)\xi_g$: tilt parameter ;
  - s: deviation parameter of the incident beam respect with the Bragg condition;
  - θ: angle between the incident beam and the diffracting plane $(h\,k\,l)$;
  - θ_B: angle between the incident beam and the diffracting plane $(h\,k\,l)$ in Bragg condition.

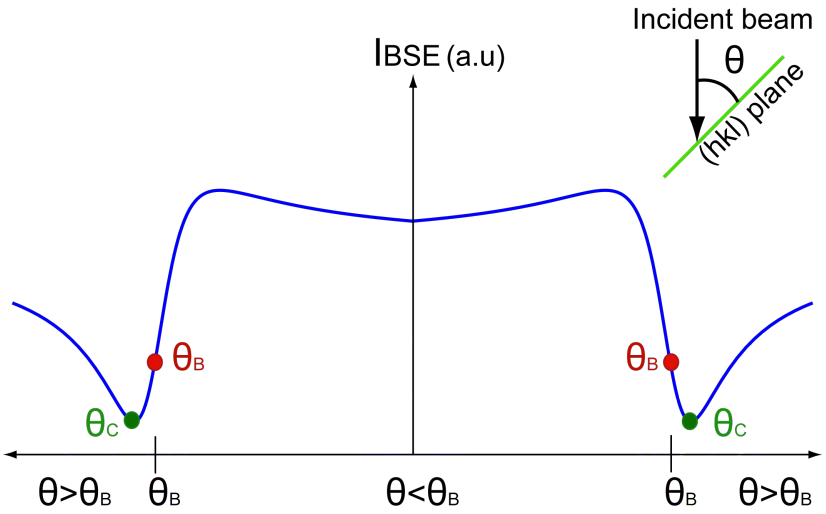

Figure III.1 – Variations of the BSE intensity with the angle between the incident beam and the diffracting plane $(h\,k\,l)$. The Bragg condition corresponds to $\theta = \theta_B$ and $\theta = \theta_c$ is the channeling condition.

The variation of I_{BSE} with θ according to equation III.4) is shown in Figure III.1. This curve corresponds to a profile of I_{BSE} crossing an isolated pseudo-Kikuchi band (see Figure II.2). It is important to note that the minimum of I_{BSE} is not localized at $\theta = \theta_B$, but at $\theta = \theta_c \neq \theta_B$. This corresponds to the so called "channeling condition".

III.2 Imperfect crystal

III.2.1 Planar defects

In addition to dislocations, GBs and SFs play a crucial role in plasticity as well. As first approximation, they can be considered as planar defects.

An interface separates a crystal into two distinct regions. Generally, one defines the upper crystal as fixed and the lower one as shifted by a vector $\overrightarrow{R}(\overrightarrow{r})$ and inclined at an angle β around an axis $\overrightarrow{v}$. In order to simplify, we restrict our study, on the one hand, to the specific cases of translation boundaries (*i.e.* $\beta = 0$) such as SFs, and on the other and, to flat interfaces (*i.e.* parallel to a crystallographic plane), such as coherent TBs. Note that a coherent TB can be described as cumulative SFs (each of them translating the crystal of $\overrightarrow{R}$) on adjacent planes. Therefore, $\overrightarrow{R}(\overrightarrow{r})$ is not constant moving away from the TB plane (but constant along it), thus giving a $\overrightarrow{R}(\overrightarrow{r})$ not directly connected to the crystal lattice.

III.2.1.1 Theoretical approach

Let us assume that an isolated inclined planar defect (angle ζ from the surface) separates a perfect upper crystal with a translated lower one, as schematized in Figure III.2.

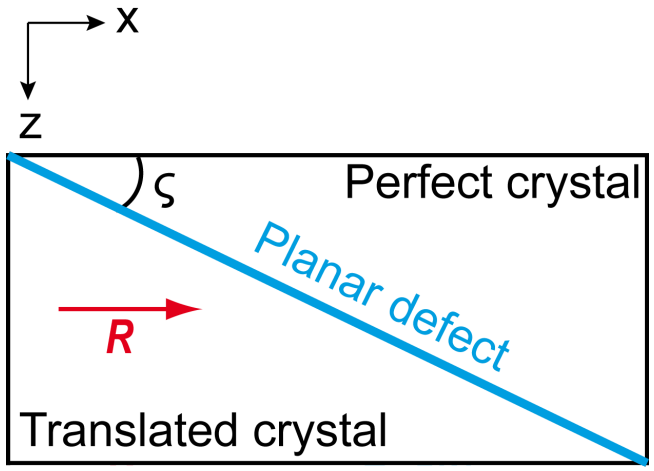

Figure III.2 – Schematic of an inclined planar defect with an angle ζ from the surface of observation.

Atoms in the lower crystal are translated collectively by a vector $\overrightarrow{R}$ (assumed to be constant along the plane of the defect *i.e.* $\overrightarrow{R}(\overrightarrow{r}) = \overrightarrow{R}$) with respect to the upper crystal. It is convenient to introduce another modified tilt parameter, ω', such as [105]:

$$\omega' = \omega + \omega_{DP} = \omega + \left(\overrightarrow{g} \cdot \overrightarrow{R}\right) \xi_g \tag{III.5}$$

Therefore, ω_{DP} is the tilt parameter due to the translation of the lower crystal with the upper one. Note that ω_{DP} is null in the upper crystal.

For a column localized at a position x, whose inclined planar defect is at a depth z_{DP}, the BSE intensity is given by [105]:

$$\begin{aligned}
\eta_{tot}(\omega) &= \int_0^{z_{DP}} \frac{\partial \eta(\omega, z)}{\partial z} \,\mathrm{d}\, z + \int_{z_{DP}}^{\infty} \frac{\partial \eta(\omega', z)}{\partial z} \,\mathrm{d}\, z \\
&= \eta_{sup}(\omega) + \eta_{inf}(\omega') \\
&= \int_0^{z_{DP}} \frac{\partial \eta(\omega, z)}{\partial z} \,\mathrm{d}\, z + \int_0^{\infty} \frac{\partial \eta(\omega', z)}{\partial z} \,\mathrm{d}\, z - \int_0^{z_{DP}} \frac{\partial \eta(\omega', z)}{\partial z} \,\mathrm{d}\, z \\
&= \eta_{sup}(\omega) + \eta'_{inf}(\omega') - \eta''_{inf}(\omega')
\end{aligned} \tag{III.6}$$

where:

- η_{sup}: contribution of the upper crystal with an equivalent thickness of z_{DP};
- η_{inf}: contribution of the translated lower crystal with an infinite thickness;
- η'_{inf}: contribution of the lower crystal with an infinite thickness;
- η'_{inf}: contribution of the lower crystal with an equivalent thickness of z_{DP}.

From Figure III.2, z_{DP} is given by:

$$z_{DP} = x \tan(\zeta) \tag{III.7}$$

where:

- x: abscissa, where I_{BSE} is calculated. Origin is taken at the intersection of the planar defect with the surface;
- ζ: angle between the planar defect and the surface of observation.

The term η_{sup} in equation III.6 is the contribution to I_{BSE} of the upper crystal with a thickness of z_{DP}. By considering equation III.7, all displacement along x leads to an increase of z_{DP}, and then, the thickness of the upper perfect crystal. Analytically, we can note that η_{sup} is written as:

$$\eta_{sup}(\omega, z_{DP}) = \int_0^{z_{DP}} \frac{\partial \eta(\omega)}{\partial z} \, \mathrm{d}\, z = \eta_{OC}(\omega) + T(\omega, z_{DP})$$
$$\text{with} \quad \lim_{z_{DP} \to \infty} T(\omega, z_{DP}) = 0 \tag{III.8}$$

where:

- η_{OC}: BSE coefficient independent of z_{DP}. Its expression is given by equation III.4;
- T: term of the BSE signal dependent on ω and z_{DP}.

Figure III.3 shows $\eta_{sup}(\omega)$ profiles for several thicknesses, z_{DP}, of a perfect crystal. It is obvious that these intensity profiles have several regimes and the origin lies in the competition competition between transmission and channeling of electrons. For small thickness ($\approx 0.2\xi_g$), no band is observed, thus favoring transmission. For thickness around $1.6\xi_g$, the curve has the same evolution as the one given by equation III.4, describing electron channeling. However, for intermediate thicknesses, the competition between transmission and channeling leads to a transitory regime, where oscillations are observed at the curve edges.

Substituting equation III.7 into equation III.6, it is possible to write η_{tot} as a function of x and $\overrightarrow{g} \cdot \overrightarrow{R}$. Therefore, several cases can be distinguished (Figure III.4):

- $\overrightarrow{g} \cdot \overrightarrow{R} \neq 0$: the curve decreases with oscillations. The latter disappear for $x = X$. Note that X decreases with increasing ζ.

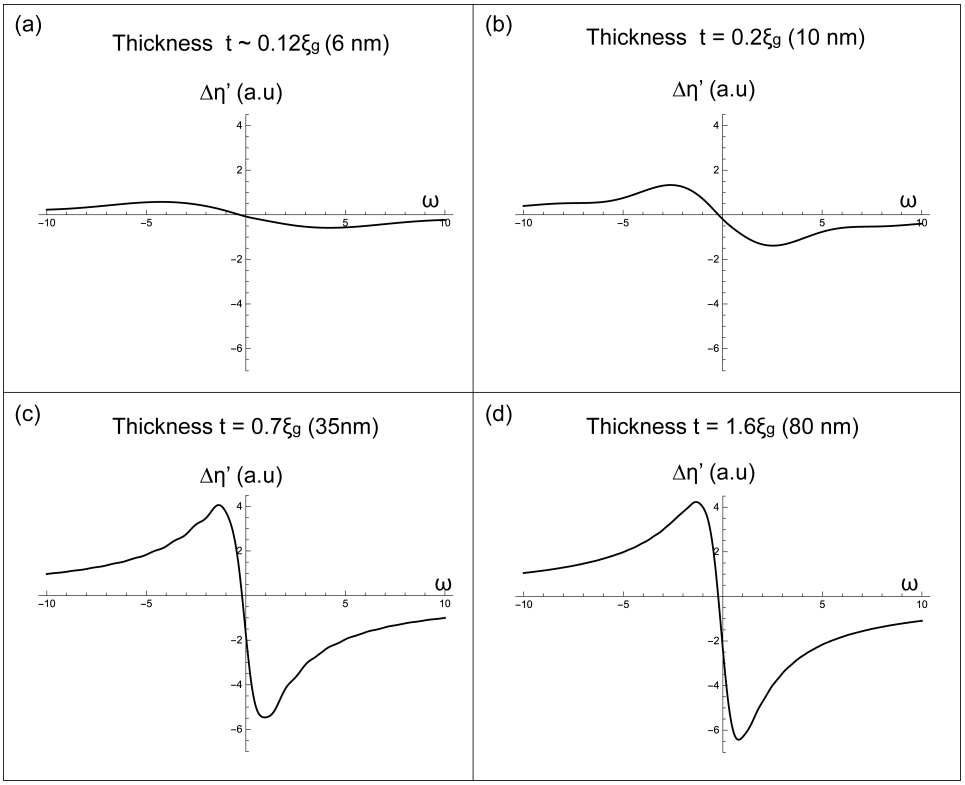

Figure III.3 – BSE intensity profile of an edge of a pseudo-band of KIKUCHI for several thicknesses (z_{DP} called t here) of a perfect crystal. From [105].

- $\overrightarrow{g} \cdot \overrightarrow{R} = 0$: the curve is constant and no contrast is distinguished from the background. Such condition corresponds to the extinction condition of SF. Note that it is similar to that one in TEM (equation II.2).

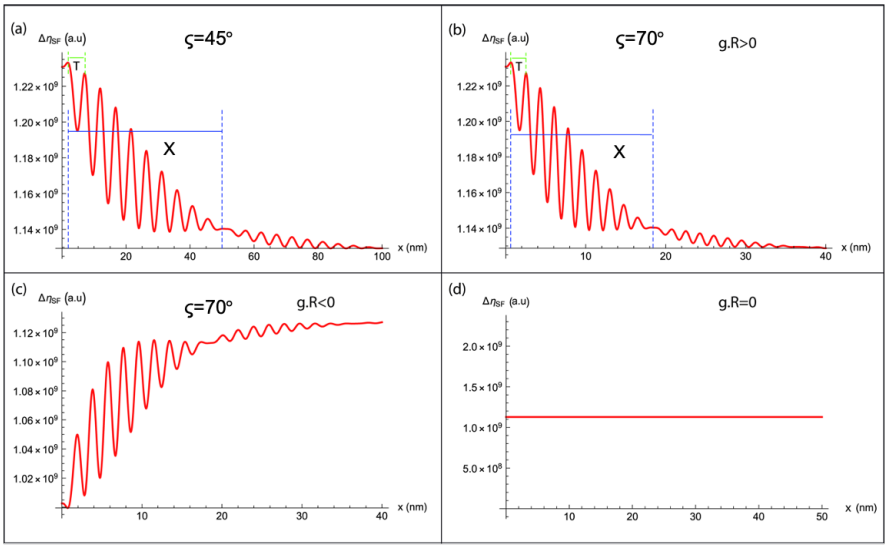

Figure III.4 – BSE intensity profiles calculated as a function of x. From [105].

It is important to note, that a coherent TB is a particular GB with very low energy (Figure I.3). As already explained previously, $\overrightarrow{R}$ is not constant moving away from the TB plane (but constant along it), thus giving a $\overrightarrow{R}(\overrightarrow{r})$ not directly connected to the crystal lattice. Therefore, $\overrightarrow{g} \cdot \overrightarrow{R}$ is never null.

III.2.1.2 Confrontation with experiment in the case of a twin boundary

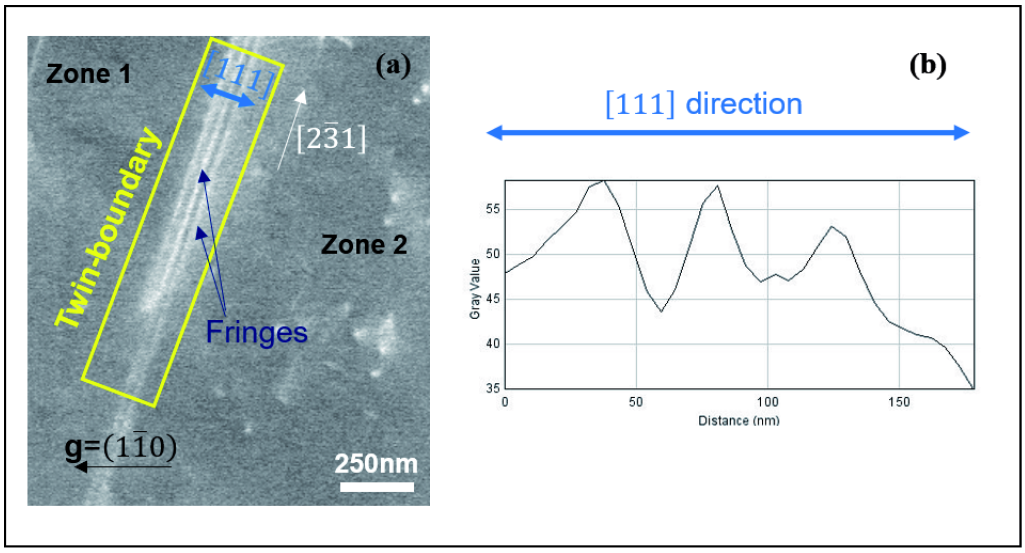

Figure III.5 – ECC micrograph of a TB observed in a TiAl alloy. From [105].

Figure III.5 shows an ECC micrograph of a TB in (1 1 1) observed in a TiAl alloy. The TB separates two γ grains (labeled zone 1 and zone 2 in Figure III.5). Observations planes of both grains are respectively (4 5 7) and (0 1 3). The common direction between both grains is $[2\,\bar{3}\,1]$. Therefore, the TB is inclined by 11° with respect to the surface of the sample.

As shown in the experimental profile of Figure III.5, the previous model reproduces qualitatively the main features observed: at the intersection between the TB and the observation surface, the contrast is bright. Then, intensity oscillations are observed, while moving away from the TB (toward increasing x in Figure III.4).

III.2.2 Dislocations and their configurations

Let us consider a column at the distance x from a dislocation, localized at $x = 0$, at the depth $z = z_D$, with a line parallel to the surface (Figure III.6).

Contrary to SFs, $\overrightarrow{R}$ for dislocations is not constant but it depends on (x, z) [4]. Hence, $\overrightarrow{R}$, at the depth z_D can be written in series of TAYLOR:

$$\overrightarrow{R}(x,z) = \overrightarrow{R}(x,z_D) + \frac{\partial \overrightarrow{R}(x,z_D)}{\partial z}(z - z_D) \tag{III.9}$$

By introducing equation III.9 in equation III.2, and by supposing that distorsions are linear at the vicinity of the depth z_D (Figure III.6, the problem is simplified in the study of a new deviation parameter, s', such as [106]:

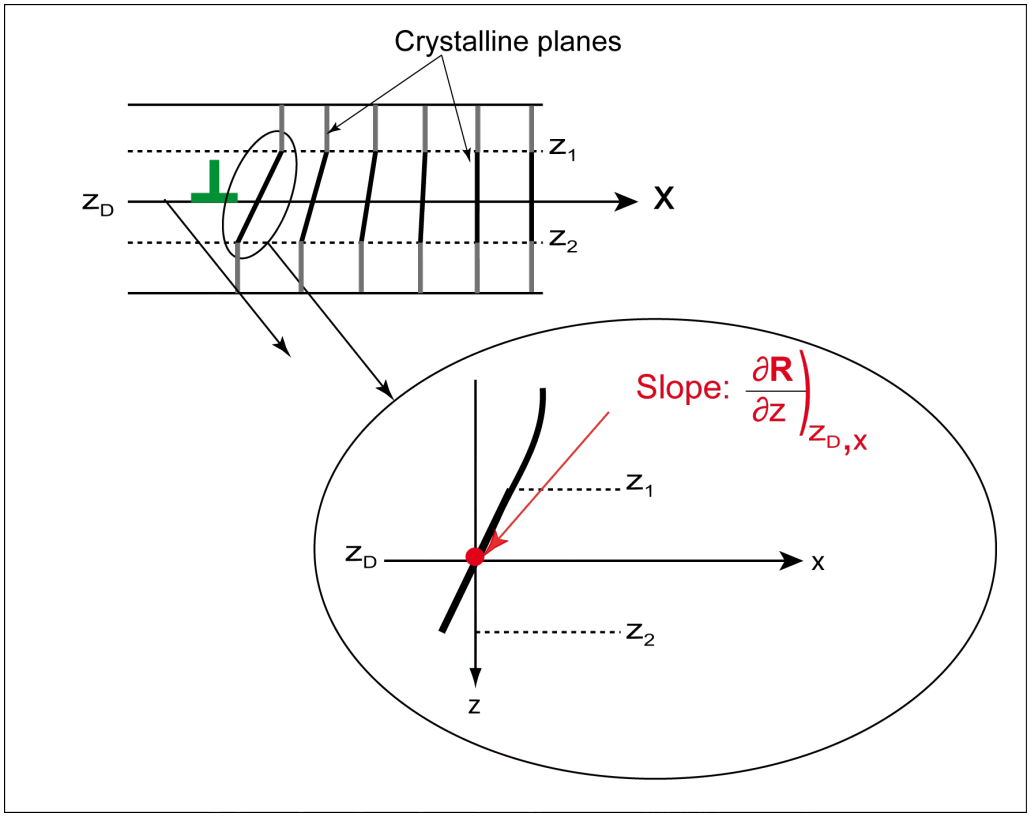

Figure III.6 – Schematic of an edge dislocation parallel to the surface and localized at a depth z_D. Distorted planes, perpendicular to the surface, are localized at a distance x for the dislocation core.

$$s' = s_{exp} + s_D \text{ with } s_D = \overrightarrow{g} \cdot \frac{\partial \overrightarrow{R}}{\partial z}_{z=z_D} \tag{III.10}$$

s_{exp} is the deviation from the exact BRAGG position in a perfect crystal and it can be measured experimentally [104]. The dot product $\overrightarrow{g} \cdot \frac{\partial \overrightarrow{R}}{\partial z}_{z=z_D}$ represents the deviation s_D due to the variations of the angle between the primary beam and the

distorted planes around the dislocation core. Far from the dislocation, the crystal is seen as perfect *i.e.* the deviation s_D becomes null. By substituting s by s' in equation III.4, we can take into account the effect of the presence of a dislocation line on the intensity profile, given by:

$$I_{BSE} \propto \frac{N\sigma_B}{4\pi}\xi'_0 \left(-\frac{\left(s_{exp} + s_D(x)_{z=z_D}\right)\xi_g + \frac{\xi'_0}{\xi'_g}}{1 + \left(s_{exp} + s_D(x)_{z=z_D}\right)^2 \xi_g^2 - \left(\frac{\xi'_0}{\xi'_g}\right)^2} \right) + \frac{N\sigma_B}{4\pi}\xi'_0 \left(\frac{\left(s_{exp} + s_D(x)_{z=z_D}\right)\xi_g}{1 + \left(s_{exp} + s_D(x)_{z=z_D}\right)^2 \xi_g^2 + \left[\left(1 + \left(s_{exp} + s_D(x)_{z=z_D}\right)^2 \xi_g^2\right)\frac{\xi'_0}{\xi_g}\right]^2} \right) \tag{III.11}$$

Therefore, with equation III.11, it is possible to study the variations of I_{BSE} with x (distance from the dislocation core).

III.2.2.1 Screw dislocation

At a distance x from the dislocation core (localized at $x = 0$), crystalline planes are distorted. The displacement field, $\overrightarrow{R}_{screw}$ is given in cartesian coordinates by [4]:

$$\overrightarrow{R}_{screw} = \frac{\overrightarrow{b}}{2\pi}\tan^{-1}\left(\frac{z - z_D}{x}\right) \tag{III.12}$$

The derivative of $\overrightarrow{R}_{screw}$ respect with the depth z, at the vicinity of the turning point ($z = z_D$) is given by:

$$\left(\frac{\mathrm{d}\,\overrightarrow{R}_{screw}}{\mathrm{d}\,z}\right)_{z=z_D} = \left(\frac{\overrightarrow{b}}{2\pi x\left(1 + \left(\frac{z-z_D}{x}\right)^2\right)^2}\right)_{z=z_D} = \frac{\overrightarrow{b}}{2\pi x} \tag{III.13}$$

With this reasoning, the substitution of equation III.13 in equation III.11 leads to obtain variations of BSE signal as function of x and as experimental parameters $\overrightarrow{g}$ and s_{exp}. For the case of $s_{exp} = 0$, variations are shown in Figure III.7 and those for s_{exp} slightly positive are shown in Figure III.8.

For $\overrightarrow{g}$ and $-\overrightarrow{g}$ with $s_{exp} = 0$, profiles of dislocations are antisymetric: a hallow then a peak experimentally corresponding to dark and white edges of dislocation

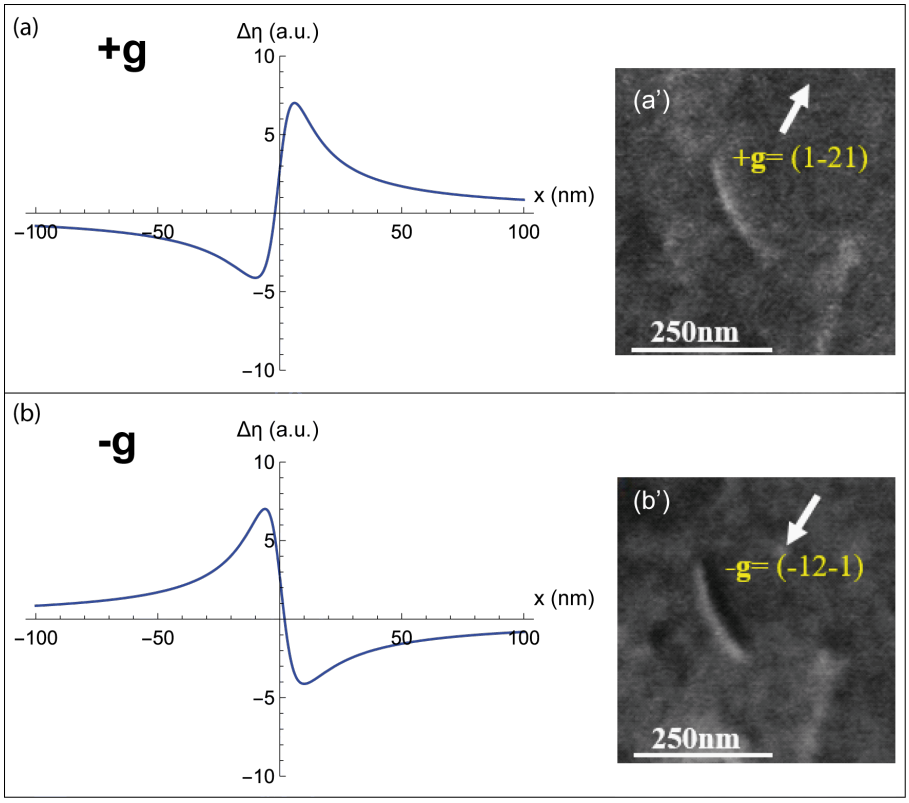

Figure III.7 – Profiles of I_{BSE} for a screw dislocation parallel to the surface with $s_{exp} = 0$; (a) $+g$ and (b) $-g$. (a') et (b') experimental ECC micrographies. From [106].

contrast. Moreover, when changing from $\overrightarrow{g}$ to $-\overrightarrow{g}$, these extrema are inverted: peak becomes hollow, and vice-versa.

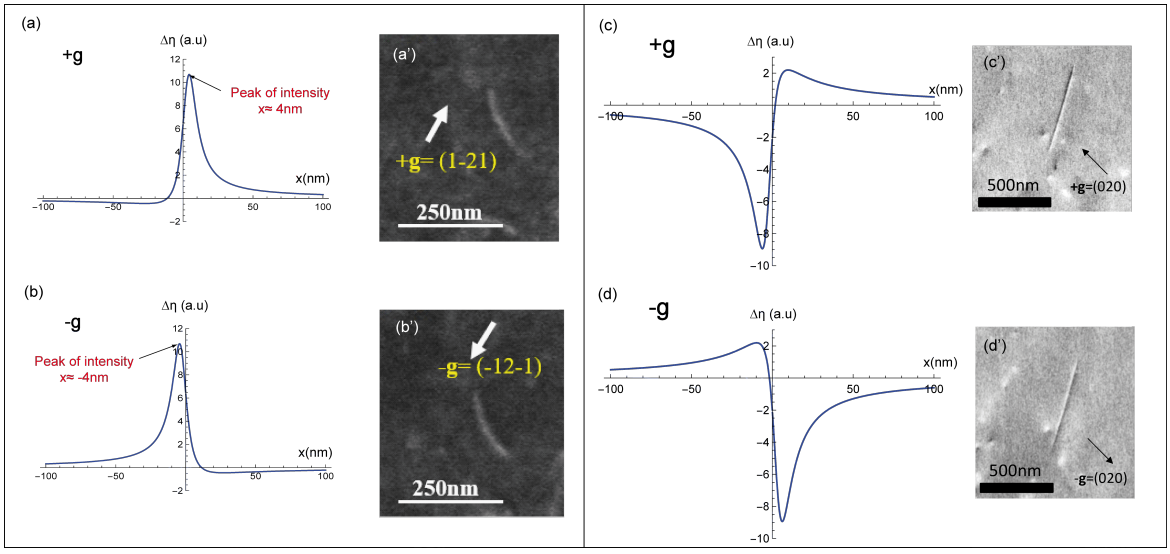

Figure III.8 – Profiles of I_{BSE} for a screw dislocation parallel to the surface with $s_{exp} > 0$; (a) $+g$ and (b) $-g$. (a'), (b')) experimental ECC micrographies. From [106].

For s_{exp} slightly positive *i.e.* $s_{exp} = 0.01\,\mathrm{nm}^{-1}$ (Figure III.13) and for either $\overrightarrow{g}$ or $-\overrightarrow{g}$, the intensity profile shows one peak only. The latter does not coincide with the real position of the dislocation, *i.e.* $x = 0$, but it is located at $x = 4$ nm. Moreover, this peak changes side while inverting $\overrightarrow{g}$. This result is analogous in TEM [62] and it is generally used for characterizing dislocation dipoles (Figure III.9) [104, 107].

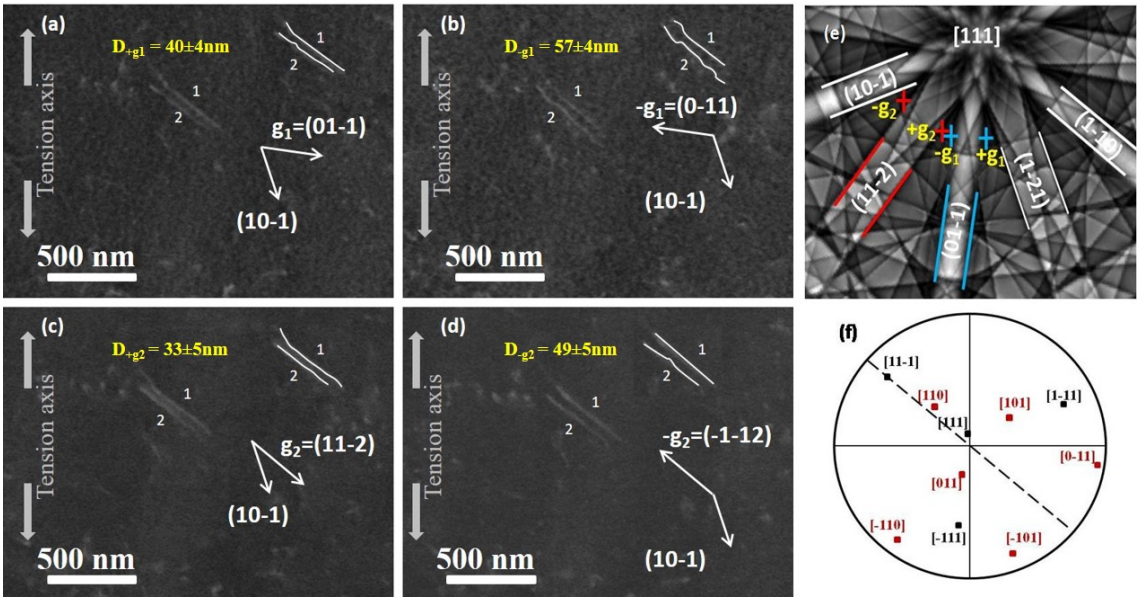

Figure III.9 – First ECCI characterization of a dislocation dipole in an IF steel. From [104].

III.2.2.2 Edge dislocation

For an edge dislocation parallel to the surface, it is analogous to the case of a screw dislocation. Intensity profiles are similar, as well. However, $\overrightarrow{R}_{edge}$ is written as [4]:

$$\overrightarrow{R}_{edge} = \frac{\overrightarrow{b}\,\beta}{2\pi}\left(\beta + \frac{\sin 2\beta}{2(1-\nu)}\right) + \frac{\overrightarrow{b}\wedge\overrightarrow{u}}{2\pi}\left(\frac{1-2\nu}{2(1-\nu)}\ln|r| + \frac{\cos 2\beta}{4(1-\nu)}\right) \qquad \text{(III.14)}$$

III.2.2.3 Extinction conditions

Theoretical calculations allow to demonstrate the extinction conditions well-known in microscopy (equation II.1). Note that such criteria are experimentally applicable for ECCI but they were not proved theoretically. Calculated dislocation intensity

profiles are shown in Figure III.10. Note that in the case of an edge dislocation, a residual contrast is observed when $\overrightarrow{g} \cdot \left(\overrightarrow{b} \times \overrightarrow{u}\right) \neq 0$. This behavior is similar to those observed in TEM.

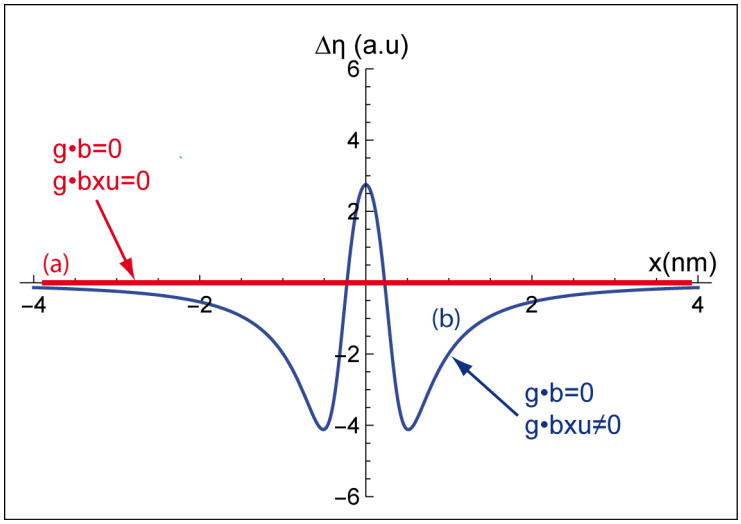

Figure III.10 – Extinction conditions. From [106].

Despite this undeniable limitation, ECCI has the major advantage of providing access to a large regions of interest, allowing more statistically relevant studies to be carried out. Some examples will be presented in the following chapters.

Chapter IV

Evolution of crystalline defects close to a real interface

Most of our detailed knowledge on dislocation-interface interactions are extracted from *in* and/or *ex-situ* TEM [108, 109]. However, these studies have drawbacks, such as areas of observation limited to a few tens of μm^2 and modification of the microstructures due to the preparation of a thin foil [76, 110]. Besides TEM, *in-situ* mechanical testing coupled with x-ray diffraction (particularly Laue microdiffraction) [111, 112] or with EBSD can provide features of operating mechanisms that can feed full-field models [113]. However, both techniques are sensitive to variations of GND density only [114] and particularly for Laue microdiffraction, it requires devising techniques for sample preparation [72]. Therefore, one part of the problem is passed over in silence (*i.e.* SSD).

It is clear that current techniques have reached their limits. We have to deal with the following conflict: if the technique (Laue or EBSD) is statistically representative, some information will be missing and if the technique allows capturing all the information (TEM), its statistical representativeness will be very low. Therefore, full comprehension of dislocation-interface interactions requires a new experimental approach, in order to study localized deformation in the vicinity of an interface and to characterize evolution of microstructures.

These studies were initiated at the end of the doctoral work of Hana Kriaa (2015–2018) and then extended during the doctoral work of Frederic Habiyaremye (2018–2022). The underlying methodology of this research is that intrumented

nanoindentation is combined with A-ECCI characterization before and after deformation.

IV.1 Procedure of a localized deformation test by instrumented nanoindentation

IV.1.1 Instrumented nanoindentation testing

Instrumented nanoindentation testing is a localized deformation test on a bulk specimen. It consists, as in the case of hardness measurements, in penetrating a tip inside a material in order to deduce its mechanical properties. The evolution of the applied force and its penetration depth in the material are measured continuously, over a load-unload cycle. Applied loads remain low, ranging from a hundred µN to a hundred mN.

The curve in Figure IV.1 represents the typical evolution of the applied force with the displacement inside the material. It is divided into two distinct parts. The load corresponds to the penetration of the indentation tip up to the maximum depth h_{max}. The unload characterizes the withdrawal of the tip with the presence of a residual imprint of depth h_r. The parameter h_c is called depth under contact (or true depth of penetration) h_s and A_P are the elastic deformation out of contact. and the projected area, respectively. All these parameters are schematized in Figure IV.1.

During imposed force nanoindentation tests, displacement jumps can be observed. These bursts, corresponding to sudden displacements of the indenter into the sample without increasing the load, are commonly called *pop-ins*. A pop-in results in a horizontal plateau on the force-depth curve (Figure IV.1) starting at the depth h_p and at the load P. Note that during a controlled displacement test, pop-ins correspond to sudden drops in force. In all observations, the deformation before the pop-in is reversible, so that it is considered as purely elastic. Therefore, the first pop-in marks the onset of irreversible deformation, so that it has very often been

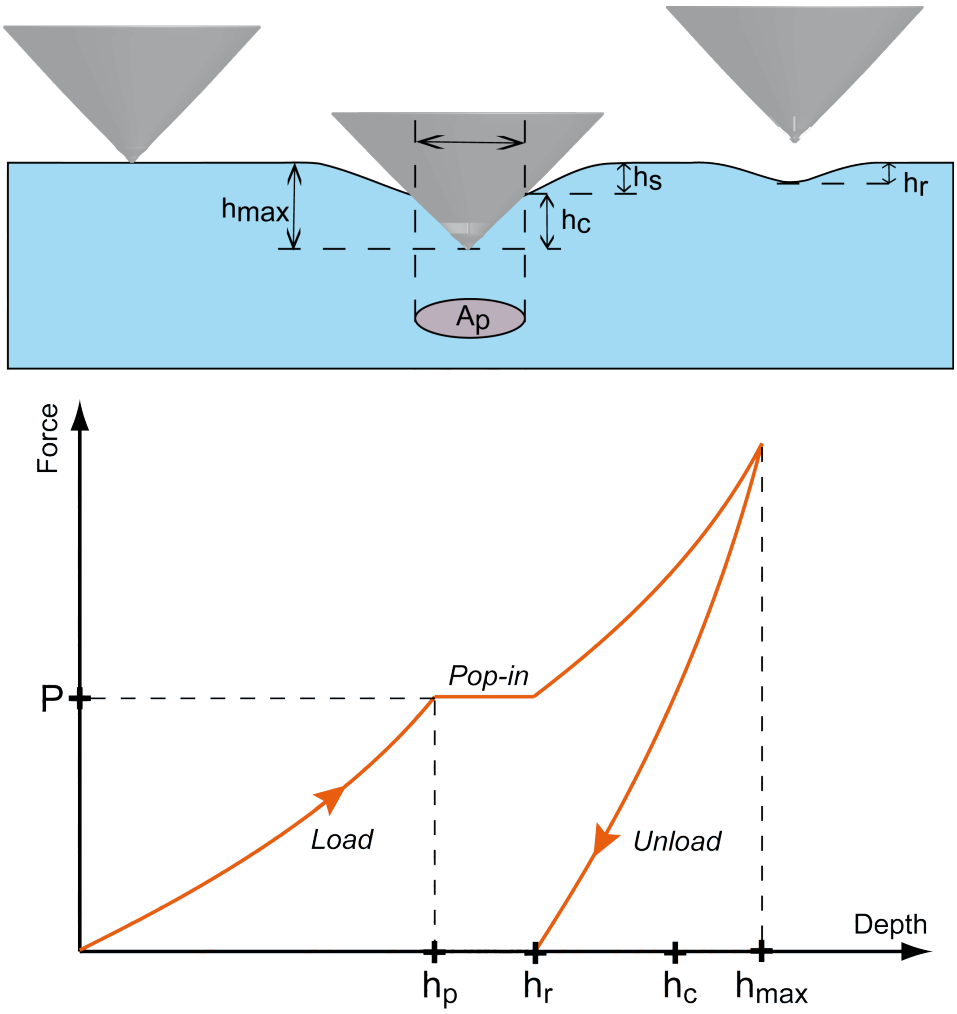

Figure IV.1 – Typical nanoindentation curve with a pop-in and schematic of important parameters. Adapted from [115].

linked to the nucleation of dislocations [115]. Proposed mechanisms suggest homogeneous nucleation of dislocations, activation of sources of dislocations, rupture of a surface film or interaction of a film with the underlying dislocation structure. Thus, the pop-in is seen as the event, which marks the sudden transition from an elastic regime to a continuous elastoplastic regime. In addition, the complex interactions of stress fields due to configurations of dislocations and indentation account for the large scatter in the measured value of the pop-in load P [116].

The elastic part of the nanoindentation curve *i.e.* before pop-in, can be described by the Hertz theory of contact [117, 118]. This theory models the elastic contact between a sphere and a plane by assuming elastic deformation and very

small penetration depth respect with the contact radius. Therefore, F is related to the penetration depth h as follows [115]:

$$F = \frac{4}{3} E^* a^{\frac{1}{2}} h^{\frac{3}{2}} \tag{IV.1}$$

where:

- E^*: reduced elastic modulus given by:

$$\frac{1}{E^*} = \frac{1-\nu_i^2}{E_i} + \frac{1-\nu_s^2}{E_s} \tag{IV.2}$$

  with E and ν are the elastic modulus and POISSON's ratio respectively. Subscripts i and s refer to the indenter and the sample respectively.

- a: radius of a spherical indenter.

IV.1.2 Procedure for studying deformation mechanisms in the vicinity of a real GB

The first step consists in selecting the GB of interest and characterizing it by EBSD. Initial crystalline defects are also characterized by A-ECCI before deformation. Note that in the case of LAGBs, A-ECCI is the most adapted technique for observing them in standard conditions.

As soon as the GB is well characterized, localized deformation tests are performed near the GB by nanoindentation using a BERKOVICH tip *i.e.* a triangle-based pyramid. A network of indents can therefore be programmed.

In order to easily localize the indent network, indents are high load (20 mN) are programmed as horizontal and vertical lines at about 100 µm from the network of interest. These indents are clearly visible with SEM. Finally, some indents are observed by A-ECCI. Note that because of low loads, residual indents of interest are very small *i.e.* about few tens of nm. By following this procedure, it is now possible to link local mechanical properties with the evolution of microstructures near GBs.

In the next parts, we will focus on two cases:

1. deformation mechanisms near a TB in a TiAl alloy;

2. deformation mechanisms near a LAGB in a medium entropy alloy.

IV.2 Deformation mechanisms near a twin boundary in a TiAl alloy

IV.2.1 Presentation of TiAl alloys

Titanium aluminide alloys have attracted considerable attentions due to their unique combination of properties such as high specific strength and stiffness, good creep properties and resistance against oxidation and corrosion [119, 120], which make them suitable candidate materials for high temperature structural use [121, 122]. Blades of the low-pressure-turbine in the last generation of aircraft engines (GEnx – General Electric Next-generation – and LEAP – Leading Edge Aviation Propulsion) are made by cast GE (General Electric) titanium aluminide alloy – 47Al-2Cr-2Nb (at.%) – replacing Ni-superalloys two times heavier. This significantly contributes to the decrease of fuel consumption and CO_2 emission.

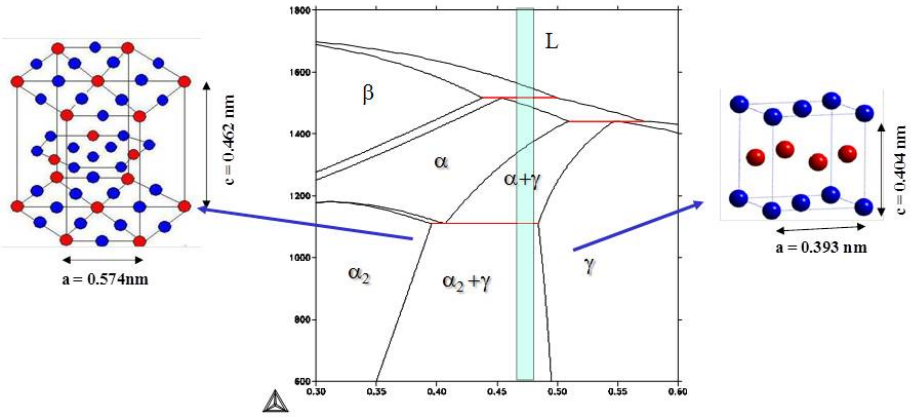

Figure IV.2 – Binary Ti-Al diagram. From [123].

The binary diagram of Ti–Al alloys have several phases [123] (Figure IV.2). Mainly two of them are ordered at room temperature: γ as the major phase and α_2 as a minor phase.

- The α_2 phase is hexagonal with a DO19 structure. $(0\,0\,0\,1)$ planes have the Ti_3Al composition but along a normal direction to $(1\,1\,\bar{2}\,0)$, a substructure appears and it can be defined as a staking of an alternation of Ti planes and TiAl planes;

- the γ phase is tetragonal with a L10 structure. It can be described as a stacking of Ti and Al planes along $[0\,0\,1]$. But the stacking along the other directions $[1\,0\,0]$ and $[0\,1\,0]$ are formed of an alternation of mixed TiAl planes. Therefore, the three $\langle 1\,1\,0\rangle$ directions are not equivalent: $[\bar{1}\,1\,0]$ is constituted of one type of atoms, while $[\bar{1}\,0\,1]$ and $[0\,\bar{1}\,1]$ are composed of an alternation of either Ti atoms or Al atoms.

Some other phases can be present, such as the high temperature β phase with the BCC structure and its ordered $B2$ variant. A broad range of engineering alloys, with baseline compositions of Ti-(42–49)Al-(0.1–10)X (at.%) with X = Cr, Nb, V, Mn, Ta, Mo, Zr, W, Y, Si, C and B, has emerged in the past, two decades ago.

The single phase γ-TiAl based alloys, like many intermetallic phases, suffer from both poor ductility and fracture toughness. Considerably improved ductility and toughness can be achieved in $(\gamma+\alpha_2)$ dual-phase alloys. The microstructures of dual-phase alloys are complex but can be roughly classified into four groups (Figure IV.3) [124, 125]:

- Near-γ (NG): constituted of γ equiaxed grains with a few α_2 grains at at grain boundaries and triple junctions (Figure IV.3.a);

- DuPlex (DP): constituted of a mixture of monolithic γ grains and small lamellar colonies of $(\gamma+\alpha_2)$ (Figure IV.3.b);

- Nearly Lamellar (NL): mainly constituted of big lamellar colonies and small γ grains (Figure IV.3.c);

- Fully Lamellar (FL): organized in big lamellar $(\gamma+\alpha_2)$ colonies (Figure IV.3.d).

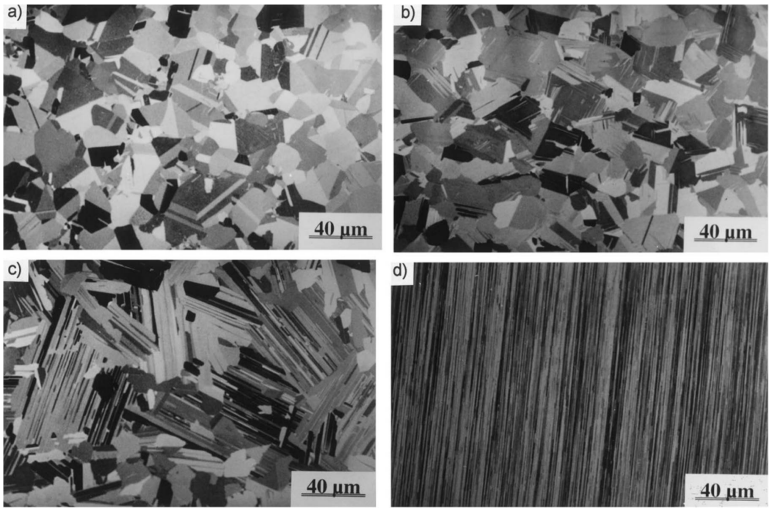

Figure IV.3 – Micrographs of the different microstructures of Ti-48Al-2Cr: (a) near-γ; (b) duplex; (c) nearly lamellar; and (d) fully lamellar. From [126].

Among these microstructures, FL alloys have the best high temperature performances, whereas DP alloys are suitable for balanced properties between room temperature plasticity and high strength and good creep resistance at high temperature.

IV.2.2 Deformation mechanisms of TiAl based alloys

In dual phase TiAl alloys, plastic deformation mainly occurs on the $\{1\,1\,1\}$ planes of the γ phase [127] by dislocation glide and it is strongly related to the ordered L10 structure. From Figure IV.4, one can see that along the $\langle\bar{1}10]$-directions there is only one sort of atoms (Ti or Al). These dislocations are called ordinary dislocations and their BURGERS vectors are $\langle 1\,0\,0\rangle$, $\frac{1}{2}\langle 110]$ types. By contrast Ti-atoms and Al-atoms interchange in $\langle 011]$-directions and the so called superdislocations are $\frac{1}{2}\langle 112]$ (twinning dislocations) and $\langle 101]$. These two types of superdislocations can undergo various dissociations into superpartial and partial dislocations and the associated planar faults.

$\frac{1}{2}\langle 110]$, $\langle 011]$ and $\frac{1}{2}\langle 112]$ type dislocations are lying in $\{1\,1\,1\}$ planes and participate in plastic deformation of the γ phase (Figure IV.4). $\langle 1\,0\,0\rangle$ dislocations seem participate in deformation at high temperature only. In addition mechanical twinning along $\frac{1}{6}\langle 1\,1\,\bar{2}\rangle\{1\,1\,1\}$ occurs and it does not alter the ordered L10 structure of the γ-TiAl. $\frac{1}{2}\langle 110]$, $\langle 011]$ and $\frac{1}{2}\langle 112]$ type dislocations are lying in $\{1\,1\,1\}$ planes

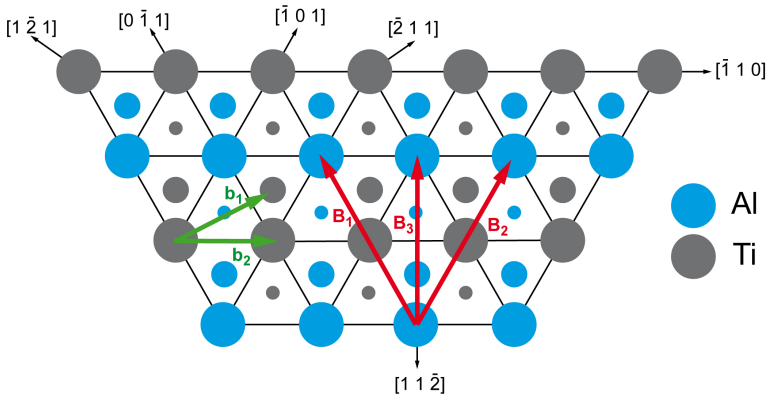

Figure IV.4 – Potential slip systems of the L10 structure, schematic drawing of a three-layer sequence of atom stacking on the (1 1 1) plane shown by small, medium and large circles. $\vec{b_1} = [1\,0\,0]$, $\vec{b_2} = \frac{1}{2}[\bar{1}\,1\,0]$ are BURGERS vectors of ordinary dislocations. $\vec{B_1} = [0\,\bar{1}\,1]$, $\vec{B_2} = [\bar{1}\,0\,1]$ and $\vec{B_3} = \frac{1}{2}[\bar{1}\,\bar{1}\,2]$ are BURGERS vectors of superdislocations.

and participate in plastic deformation of the γ phase (Figure IV.4).

In the α_2 phase, the possible slip modes are $\{1\,0\,\bar{1}\,0\}\langle\bar{1}\,\bar{2}\,1\,0\rangle$ prism slip, $(0\,0\,0\,1)\langle\bar{1}\,\bar{2}\,1\,0\rangle$ basal slip and pyramidal $\langle 1\,1\,\bar{2}\,\bar{6}\rangle$-slip with very different values of critical shear stress [127].

This brief overview shows that deformation mechanisms of TiAl-based alloys are very complex, because many fields of materials science are necessary for exploring their behaviors. The strong interplay between phases, microstructures, crystallography and chemistry forces researchers to carry out studies at different scales for taking advantages of these marvelous compounds.

IV.2.3 Evolution of microstructures near a twin boundary

The region in Figure IV.5 is composed on two grains separated by a true TB of the system $[1\,1\,\bar{2}](1\,1\,1)$: A (left) and B (right) with surface orientation respectively as $\sim(4\,5\,7)$ and $\sim(0\,1\,3)$ (Figure IV.5.a). Before deformation, dislocations in grain A are highly inclined with the surface. They are either isolated or piled up into walls. BURGERS vectors (determined from extinction conditions of equation II.1) are consistent with $\pm\frac{1}{2}[1\,1\,0]$. One Nano-Twin (NT) of system $[1\,1\,\bar{2}](1\,1\,1)$ is observed as well. No good channeling conditions were reachable in grain B, so that dislocations were not fully characterized.

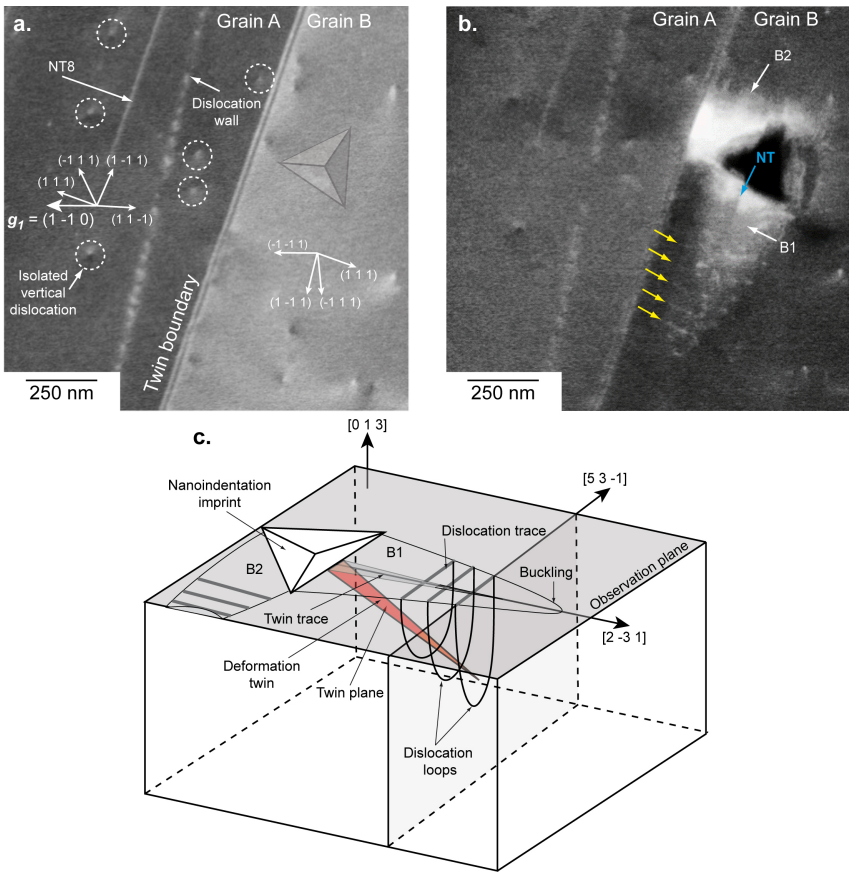

Figure IV.5 – Region of interest observed by A-ECCI before (a.) and after (b.) µN-nanoindentation. Grain A (surface orientation: (4 5 7)) and grain B (surface orientation: (0 1 3)) are separated by a true TB of the system $[1\,1\,\bar{2}](1\,1\,1)$. (c.) 3D scheme explaining the formation of the pile-up areas B1 and B2. From [128].

The ECCI micrograph after deformation is shown in Figure IV.5.b with its scheme in IV.5.c. A Berkovitch indent with a charge of 500 µN was performed in grain B near the TB. Around this imprint, two pile-up areas (B1 and B2 in Figure IV.5.b) are observed. Parallel to the TB in the pile-up B1 a stack of parallel dislocations is observed (yellow arrows in Figure IV.5.b). In addition, a contrast similar to that of a NT of the system $[1\,1\,\bar{2}]$ (1 1 1) (blue arrow in Figure IV.5.b) is observed inside B1. In the neighboring grain A, no change is observed compared to the initial state, even if the TB is locally deformed, where B2 is in contact. Apart from the two pile-up areas, no other defect is observed.

In many materials, such pile-up areas are associated to canalization of deformation, generally originating in the accommodation of twins [4] or KB [60]. Although the accommodation of twins $\frac{1}{6}\langle 11\bar{2}]$ {1 1 1} by ordinary $\frac{1}{2}\langle 110]$ {1 1 1} dislocations

has already been reported by TEM experiments in Ti-Al alloys [129, 130], no mechanism has been proposed.

From these results, the following scenario can be proposed (Figure IV.5.b):

- Under the indent, the $[1\,1\,\bar{2}]$ $(1\,1\,1)$ NT is formed.
- The stress concentration at the tip of the $[1\,1\,\bar{2}]$ $(1\,1\,1)$ NT causes nucleation of ordinary $\pm\frac{1}{2}$ $[1\,1\,0]$ dislocation loops gliding in $(1\,\bar{1}\,1)$ plane. It thus forms an ellipsoid surrounding the NT to form a pile-up area.
- The pile-up expends by adding dislocation loops at its extremity.
- Then, the pile-up extends until it encounters an obstacle, such as a TB.
- At the interception between B2 and the TB, a stress concentration appears thus causing a local deformation of this interface.

In summary, nanoindentation tests combined with A-ECCI observations before and after deformation have been able to shed new light on deformation mechanisms of Ti-Al alloys:

- At room temperature, twinning appears to be the main mechanism to accomodate plastic strain.
- A TB is an obstacle to the propagation of the deformation leading to stress concentration at the intersection with TB. For higher loads, it can lead to micro-cracking [130–132].

IV.3 Study of fundamental deformation mechanisms near a low-angle grain boundary in a medium entropy alloy

IV.3.1 Presentation of high and medium entropy alloys

Medium Entropy Alloys (MEA) and High Entropy Alloys (HEA) consist of two to four and at least five elements, respectively, with almost equiatomic concentrations [133, 134]. Among these new classes of materials, CrMnFeCoNi and one of its ternary equiatomic derivatives, CrCoNi, are currently attracting increasing interest in literature [135, 136] due to their excellent damage resistance at low and very low temperatures. CrCoNi has an exceptional combination of tensile strength (1.3 GPa), ductility (up to 90%) and good fracture toughness (275 MPa/m$^{\frac{1}{2}}$ at 77 K, Figure IV.6) [137, 138]. Therefore, CrCoNi is a promising alloy for low temperature applications [139].

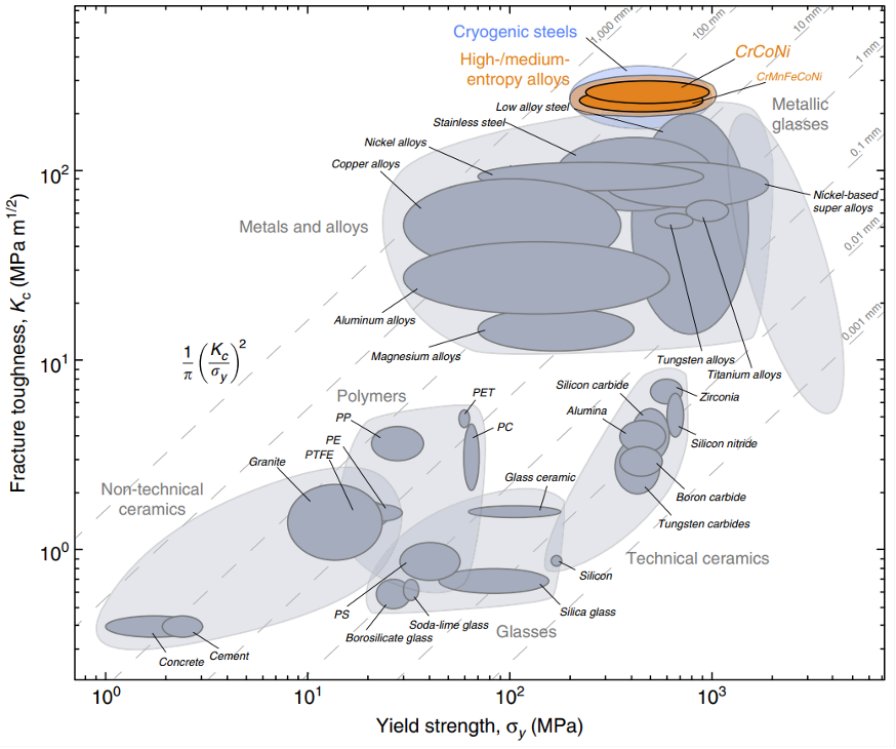

Figure IV.6 – Ashby map of the fracture toughness versus the yield strength. From [133].

One of the explanations for the exceptional damage tolerance of CrCoNi is its low stacking fault energy ($\sim 22\,\mathrm{mJ\,m^{-2}}$ [140]) and its high shear modulus [141], thus favoring high work hardening rates. Low stacking fault energy promotes partial dislocation glide and it prevents cross slip, but also it promotes mechanical NT. This last deformation mechanism introduces coherent interfaces acting as barriers to the glide of dislocations and it results in a dynamic HALL-PETCH effect without reducing the ductility [137, 140, 142, 143]. From a more general point of view, reinforcement due to GBs and growth twins (HALL-PETCH reinforcement) in CrCoNi has been shown to be particularly effective with a HALL-PETCH slope ranging from 240 to $600\,\mathrm{MPa/m^{\frac{1}{2}}}$ [11, 144–146]. However, although modeling studies have recently been reported in literature [146, 147], there is still a lack of understanding regarding the relative contributions of different types of boundaries to the yield strength *i.e.* interactions of dislocations with different types of interfaces such as LAGBs, coherent TBs and general HAGBs.

IV.3.2 Links between mechanical response and microstructure

IV.3.2.1 Pop-in load variations with distance from a LAGB

The studied LAGB (Figure IV.7) is a mixed LAGB. It separates two subgrains (A and B) with a disorientation of $\sim$0.3° with surface of $\sim(0\,0\,1)$. ECCI micrograph of Figure IV.7.b. shows that the LAGB is composed of stacking of dislocations spaced in average of 60 nm. This order of magnitude can be found by invoking equation I.6 with $\vec{b} = \pm\frac{a}{2}\langle 1\,1\,0\rangle$ as BURGERS vector.

A network of 56 indents was performed around the LAGB of interest. Among these imprints, 15 imprints closest to the LAGB (yellow curve in Figure IV.7.a) were selected. Distribution of their pop-in load is represented as a function of the distance from the LAGB in Figure IV.7.b). For imprints the most distant from the LAGB, the distribution is centered around 158 µN as mean value. The observed dispersion (standard deviation: 23 µN) can be attributed to differences in initial local density

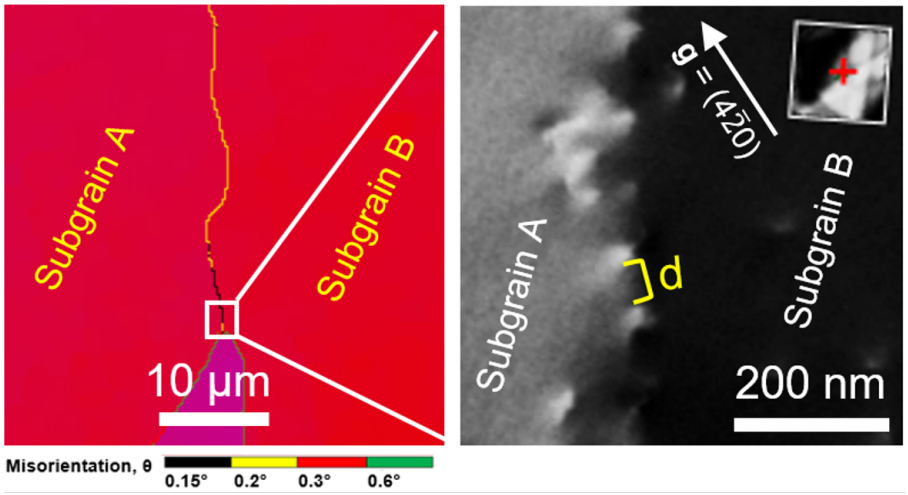

Figure IV.7 – Characterization of LAGB of interest: (a) misorientation map ; (b) ECCI micrograph of the LAGB acquired with $\vec{g}$ =(4 $\bar{2}$ 0). From [148].

of defects [149]. It is interesting to notice that the three imprints the nearest to the LAGB (n°: ♯5, ♯4 and ♯3) either do not show any pop-in (♯4 and ♯5), or have pop-in load lower than the mean value (♯3). Consequently, a detailed comparison of the evolution of the microstructures before and after deformation for these indents is required in order to establish a relation with their local mechanical behavior.

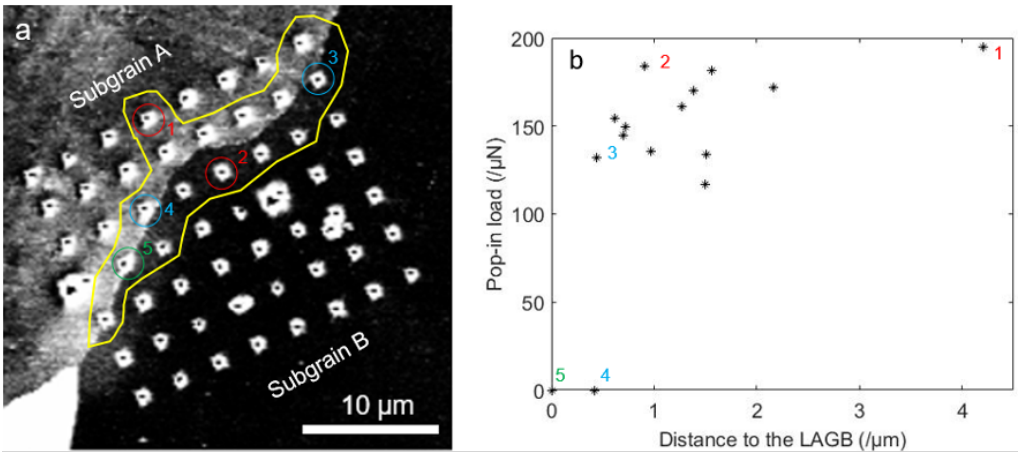

Figure IV.8 – Network of nanoindentation imprints near the LAGB. The yellow curve encircles the imprints used for plotting the pop-in load with the distance from the LAGB, shown in b. Numbers show imprints analysed in the following. From [148].

IV.3.2.2 Evolution of microstructures

By comparing nanoindentation curves, loads of the initial pop-in and the configurations of dislocations for the imprints made inside subgrains (Figure IV.9), on the

LAGB (Figure IV.10) and near the LAGB on both sides (Figures IV.11 and IV.12), it is observed, that the LAGB affects the local micromechanical response and the underlying fundamental deformation mechanisms. Changes in the microstructure can be summarized as follows.

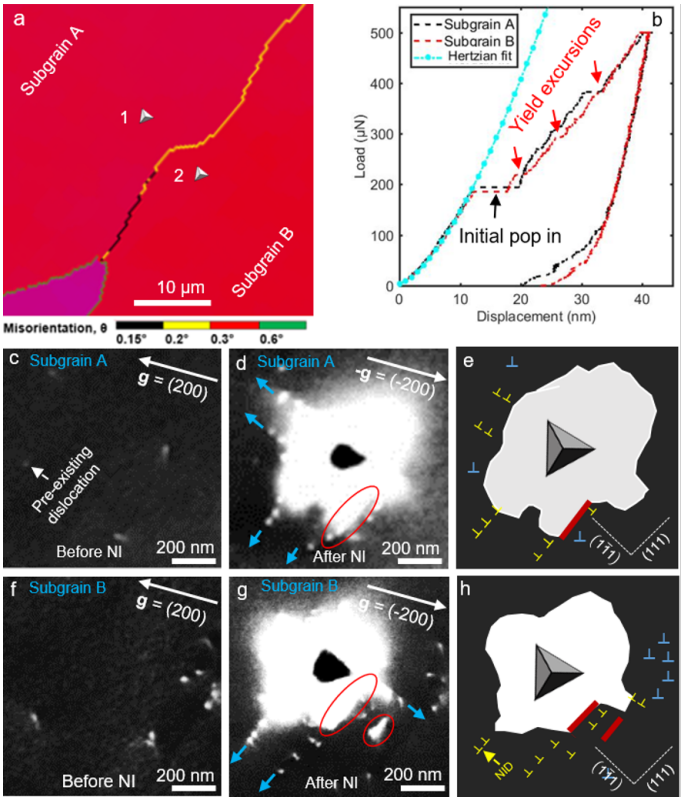

Figure IV.9 – (a) Positions of the indents in the subgrains A and B superimposed onto the EBSD map (indents ♯1 and ♯2 in Figure IV.7.a.). (b) Nanoindentation curves in subgrains A and B. The initial elastic loading stage follows the HERTZ contact theory. (c-h) Microstructural evolution as a result of nanoindentation in regions with a low initial local dislocation density (c-d) are ECC micrographs before and after nanoindentation in the subgrain A, respectively. (e) is a schematic of (d). (f-g) are ECC micrographs before and after deformation within subgrain B. (h) is a schematic of (g). The white dashed lines in (e and h) show the traces of the $(1\,1\,1)/(1\,1\,\bar{1})$ and $(1\,\bar{1}\,1)/(1\,\bar{1}\,\bar{1})$ planes. The red ellipses in (d) and (g) and red thick lines in (h) and (e) mark the traces of stacking faults. NI and NID stand for NanoIndentation and Nanoindentation Induced Dislocation, respectively. Blue arrows in (d) and (g) show pile-ups directions. From [148].

On micrographs before deformation, pre-existing threading dislocations are visible. After deformation, pile-ups of Nanoindentation-Induced Dislocations (NIDs) along the traces of $\{1\,1\,1\}$ planes and SFs or NTs are observed. This is consistent with expected deformation mechanisms of CrCoNi. Concerning indents near the LAGB (Figures IV.11 and IV.12 indents ♯3 and ♯4), a slight motion of the latter is

visible at the intersection with pile-ups. Furthermore, one NID appears on the other side of the LAGB (Figure IV.12 indent ♯3). For the indent on the LAGB (Figure IV.10 indent ♯5), NIDs are randomly distributed and only one short NID pile-up is observed on one edge of the indent.

Generally, micromechanical responses under an indenter in most situations depend on the local microstructure, such as the density of the defects, their configuration and the local chemical composition. A LAGB consists of a particular configuration of dislocations. Plasticity is initiated on contact by the glide of these dislocations, because it is not necessary to nucleate new ones. This explains the absence of initial pop-in on the nanoindentation curve (Figure IV.10). On the other hand, nucleation of new dislocations is necessary to initiate plasticity away from the LAGB and the elastoplastic transition on the nanoindentation curve is thus marked by a pronounced pop-in.

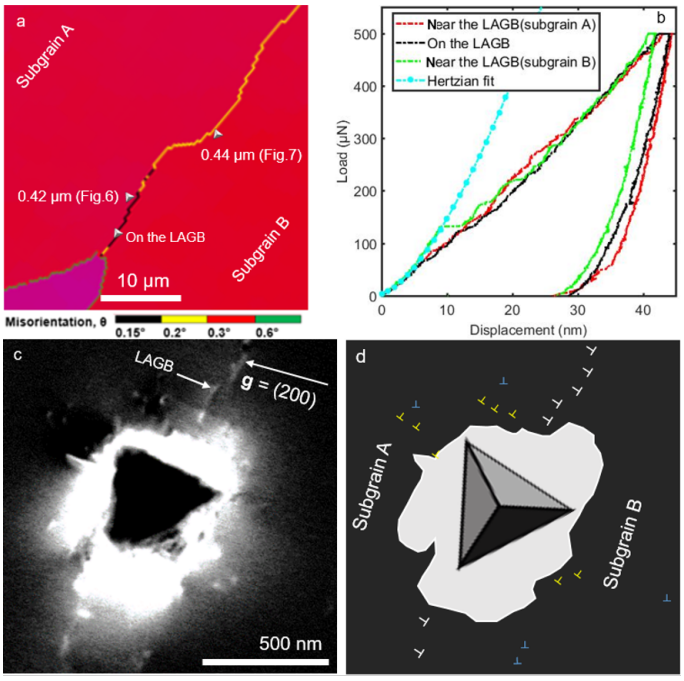

Figure IV.10 – (a) Positions of the indents superimposed on the subgrain orientation map. (b) Load-displacement curves of nanoindentation tests performed at the LAGB (♯5), 0.42 µm from the LAGB in subgrain A (♯4), and 0.44 µm in subgrain B (♯3). The initial elastic loading follows the Hertz contact theory (light blue curve). (c) ECC micrograph of indent ♯5 performed at the LAGB and (d) corresponding schematic. From [148].

For both imprints near the LAGB in both sub-grains A (Figure IV.11) and B (Figure IV.12), their micromechanical responses are extremely different, although

they are at the same distance from the boundary ($\approx 0.4\,\mu m$) and have been positioned in areas with similar dislocation densities before nanoindentation. Imprint ♯4 located in subgrain A (Figure IV.11), does not show any pop-in and it deviates upon contact with the curve of HERTZ (equation IV.1). Concerning imprint ♯3 (Figure IV.12), a pop-in is observed and its load is lower than the average value. There are three reasons. First, the local organization (discrete nature, character and position of dislocations) and the curvature of the LAGB are different for imprints ♯3 and ♯4. Second, the two indents are not symmetrical respect with the LAGB plane *i.e.* the tip of the BERKOVICH indenter has not been rotated around its axis between the indentations. Third, the deformation mechanisms are also different as evidenced by the different microstructures around the residual imprints.

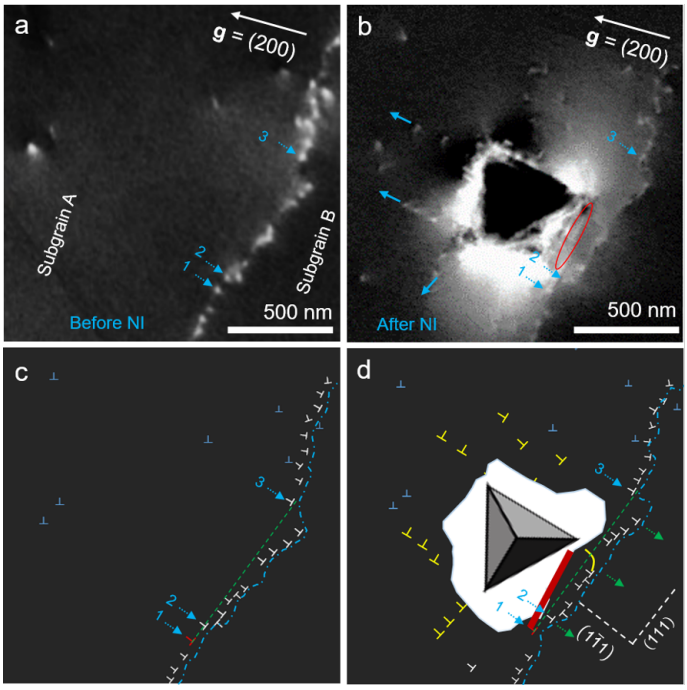

Figure IV.11 – (a,b) ECC micrographs before and after nanoindentation showing the evolution of the dislocation configurations in the subgrain A at 0.42 µm from the LAGB (indent ♯4. (c,d) schematics of (a,b). The red ellipsis in (b) and red line in (d) show a stacking fault. The blue arrows in (b) show directions along which the NID pile ups extend. The blue dashed lines in (c) and (d) show the trace of the LAGB before and after deformation. The green straight lines allow to compare the positions of the LAGB dislocations 1, 2, and 3 before and after nanoindentation while the green arrows show the direction of the slight motion of LAGB dislocations. From [148].

It is interesting to note that imprints ♯5 and ♯4 on and near the LAGB in the subgrain A, respectively, do not show pop-in and deviate at low loads from the

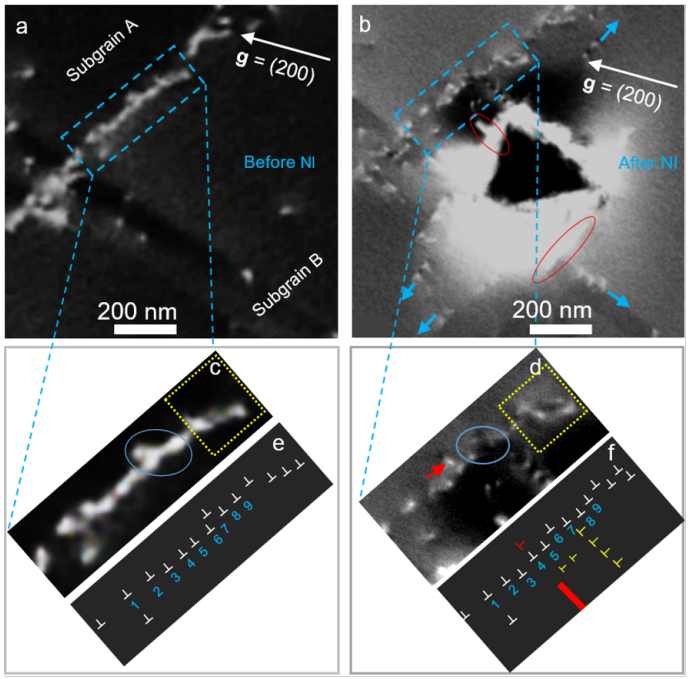

Figure IV.12 – Interactions between NIDs and the dislocations constituting the LAGB. (a-b) ECC micrographs before and after nanoindentation, respectively (indent ♯3). (c-d) Enlargement ECC micrograph of a portion of the LAGB before and after nanoindentation and (e-f) are their corresponding schematics. The red ellipses highlight stacking faults. Blue ellipses show dislocations that form a '>' like shape. From [148].

Hertz law (equation IV.1), even if they show changes in their microstructure after nanoindentation. For imprint ♯4, the absence of pop-in can be related to the subsurface structure of LAGB dislocations. Indeed, if the LAGB is inclined towards the nanoindentation axis below the sample surface and deeper than the extinction depth of the ECCI (≈100 nm), the stress field under the indenter may have interacted with the inclined LAGB dislocations. Therefore, plasticity is accommodated by glide and multiplication of these pre-existing LAGB dislocations.

It has been proposed in HEA-MEA literature that the dendritic microstructure of single crystals and especially their LAGB density, resulting from different processing routes and parameters, may be at the origin of the significant dispersion observed for the CRSS of HEA and MEA of the Cr-Mn-Fe-Co-Ni system [150]. In the present study, our observations at the dislocation scale clearly confirm these hypotheses and show that even a LAGB with a very small disorientation angle of ≈0.24° profoundly modifies the local micromechanical response and deformation mechanisms.

Chapter V

Mesoscale and statistical comparison between polycrystalline plasticity models and experiments

In metals, elementary mechanisms, such as dislocation glide, operate at the atomic scale or even at the electronic scale; typically, ångström and picosecond. These mechanisms can strongly influence the macroscopic response at the laboratory scale, *i.e.* centimeter and second. For example, *ab-initio* simulations of dislocation cores in BCC metals have shown non-Schmid effects, which could explain an asymmetry between traction and compression at the macroscopic scale [151–153].

To understand and ultimately control the mechanical behavior of metallic materials with respect to their microstructures, one has to face this incredibly complex multiscale problem that can extend over more than 10 orders of magnitude over time and in space. This is why, advanced theoretical and experimental tools are constantly being developed, aiming to relate relevant length scales and to understand involved mechanisms. This is the framework of postdoctoral works of Meriem Ben Haj Slama (2018–2020) and Kaustubh Venkatraman (2020–2022).

V.1 Development of *in-situ* deformation testing coupled with ECCI

Developing new experimental techniques allowing to understand and to predict mechanical properties of materials becomes a necessity for the materials science community in order to follow the fast evolution of our society. In this framework, this chapter reports the development of macroscopic uniaxial tensile testing of a bulk polycrystalline specimen combined with *in-situ* observations at the dislocation scale of changes in deformation microstructures at several stress states. Observations at the dislocation scale are carried out by A-ECCI in order to follow the evolution of the defects and their interactions with GBs for several regions of interest during macroscopic loading.

V.1.1 Specimen geometry

Bulk specimen were cut from a 1.78 mm thick rolled sheet of β-Ti21S alloy provided by Titanium Metals Corporation (Toronto, ON, Canada). The exact chemical composition of the material is Ti-15.97Mo-2.79Nb-2.99Al-0.26Fe-0.2Si. Quench at 843 °C for 14 min was applied before air cooling. Tensile samples were cut parallel to the rolling direction using water jet cutting (80 mesh, 3500 bar) to avoid heating and changes in the microstructure.

Developed in 1989, Ti21S is a purely β-metastable titanium alloy with a BCC structure [154, 155]. Its main characteristics are high temperature resistance, creep resistance, good cold formability, corrosion/oxidation and good thermal stability for applications up to 593 °C. It is also a popular candidate material for both aerospace and biomedical applications.

In-situ tensile tests were performed at room temperature with a DEBEN machine (Suffolk, UK) equipped with a 1 kN force cell. Measurements were carried out under an imposed force and with a strain rate of $3.3 \times 10^{-4}\,s^{-1}$. Samples were mechanically polished with a 1 µm diamond paste, followed by chemical mechanical polishing with a colloidal silica suspension in order to produce a very flat surface and to minimize

hardening due to conventional polishing. Finally, a 2 h ion polishing in a PECS II machine (GATAN, Pleasanton, CA, USA) was performed with a 3 keV beam, to improve the surface quality, so that a higher signal/noise ratio can be achieved for the BSE signal.

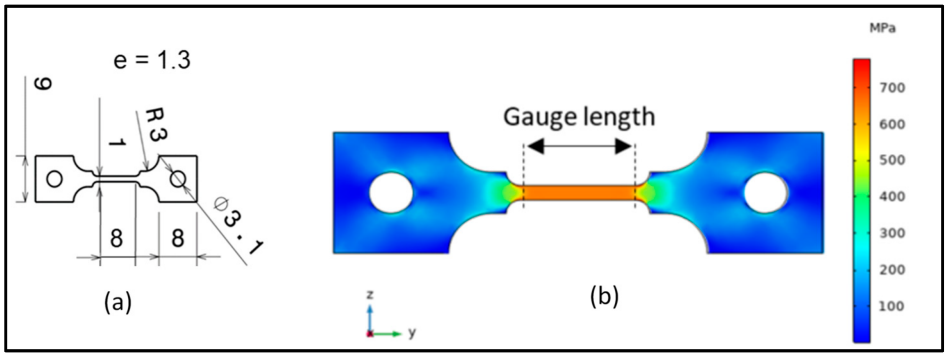

Figure V.1 – (a) Tensile sample geometry and sizes (mm); (b) Elastic deformation simulation on COMSOL. From [156].

Figure V.1 shows the geometry and dimensions of a tensile sample, which have been designed to fit into the tensile machine. A simulation of the elastic regime was carried out with COMSOL [157] in order to confirm that the stress field is macroscopically uniaxial and homogeneous in the gauge length.

Figure V.2 shows the assembly of the tensile machine and the sample inside the SEM. The configuration allows an inclination of about 15° inside the chamber with the BSE detector inserted.

V.1.2 Testing procedure

For the *in-situ* tensile test coupled with ECCI observations, as shown in Figure V.3, the three steps were followed:

1. Observations of a maximum number of areas before any loading (position 1 on the curve of Figure V.3);

2. A preliminary load, up to the macroscopic yield stress, in order to locate the different areas of interest, where deformation mechanisms are activated (seven areas have been selected to be studied under other stress states) (positions 2 and 3 on the curve of Figure V.3);

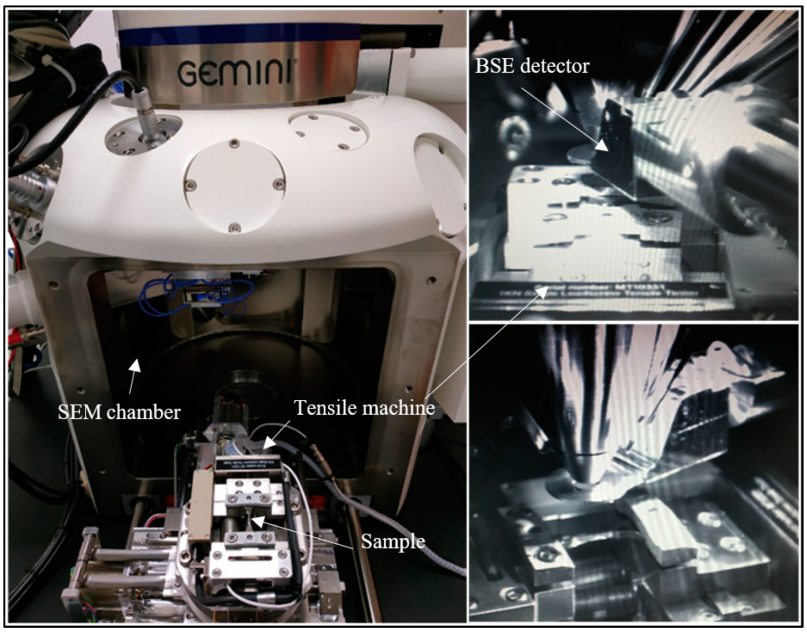

Figure V.2 – Assembly of the tensile machine/sample inside the SEM; when SEM chamber is opened (left image) and inside the closed SEM chamber with the BSE detector inserted (right images). From [156].

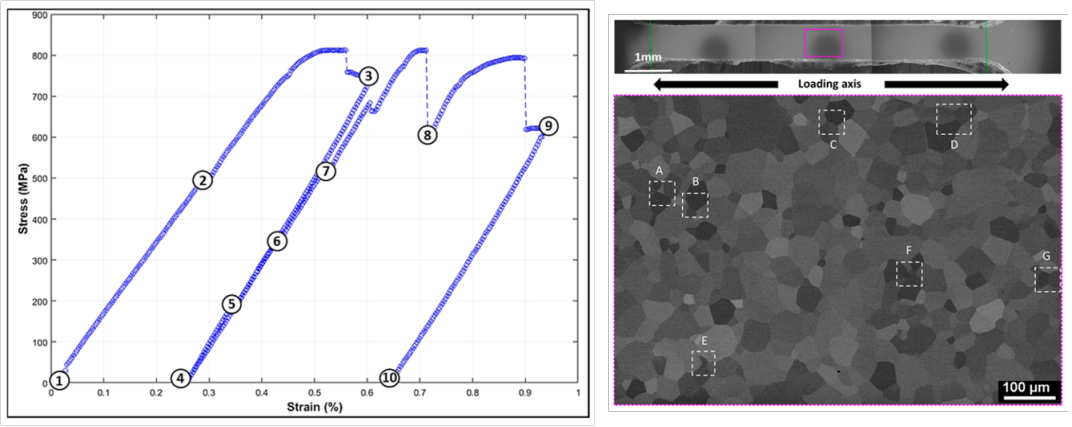

Figure V.3 – Left: *in-situ* obtained stress-strain curve of the Ti21S showing the positions where observations were made: before loading (1), during elastic deformation (2: no defect formation was observed), at the beginning of the plastic domain (3), and for six intermediate states of the second tensile cycle before unloading (four to 10). The dashed vertical lines correspond to the relaxation after plastic deformation. Right: observed area of $600 \times 450\,\mu m^2$ with the seven zones of interest in white dashed frames. From [156].

3. A second cycle, which was holded at intermediate stress states to perform ECCI of each area of interest (positions 4 to 10 on the curve in Figure V.3). Characterizations were made after 15 min of relaxation.

Observed areas were chosen to be in the middle of the gauge length. It is also

chosen far from the edges in order to avoid any edge effect. Seven zones with several slip/dislocation trace configurations are identified, as shown in Figure V.4.

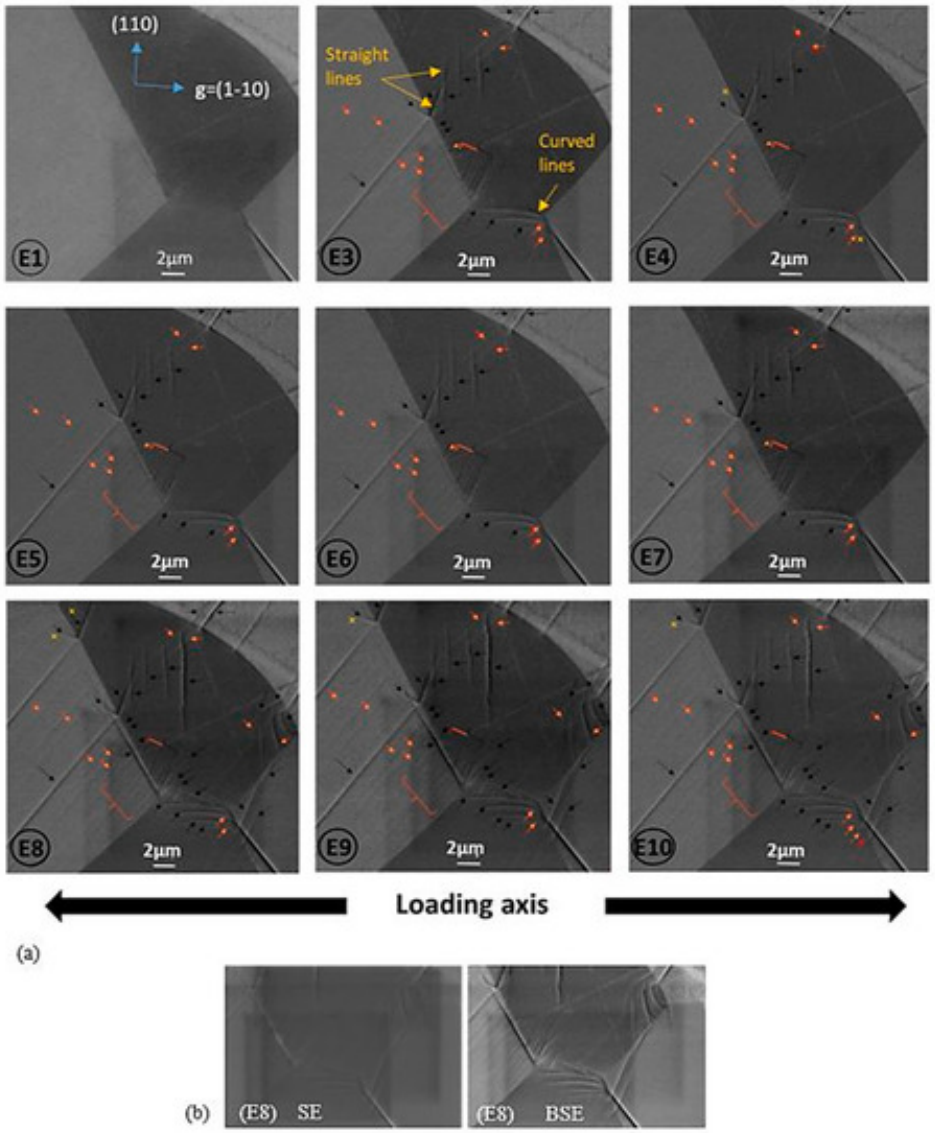

Figure V.4 – (a) BSE micrographs in channeling condition (with $\vec{g}=(1\,\bar{1}\,0)$) in the grain of interest) presenting the evolution of the defect structure corresponding to each deformation step of the tensile curve. The letter refers to the zone (E) and the number refers to the load state from the curve. Black arrows indicate slip lines, orange arrows indicate dislocations and yellow crosses indicate an increase in dislocation length; (b) Example of SE vs BSE images from zone (E8). From [156].

For each of the 7 selected zones, channeling contrast was optimized, in order to obtain good channeling conditions simultaneously on both sides of GBs. Given these working conditions, the diffraction vector is $\overrightarrow{g}=(1\,\bar{1}\,0)$.

We report, here, observations for zone E, chosen because it contains several de-

formation features, since the objective of this part is mainly to explore the potential of the *in-situ* experiment. Figure V.4 shows the evolution of the defect structure associated with different loading states for zone E; the letter refers to the zone (E) and the number refers to the state of charge of the curve. No defect is found before loading. When it is plastically deformed, several glide systems are activated and dislocations are visible. Note that dislocations are easily distinguished from surface slip traces, because they are not contrasted on micrographs acquired with the SE detector, while they are visible with the BSE detector.

Therefore, we have successfully combined *in-situ* macroscopic tensile testing of a bulk polycrystalline sample with microstructure observations. For the first time, we can track the evolution of crystalline defects under stress. This pioneers the potential of *in-situ* experiments coupled with ECCI, which becomes now very popular in the materials science community [158–160].

In conclusion, such experiment makes possible to cover large areas of interest, offering statistically relevant multiscale information to deepen deformation mechanisms. The observed slip/dislocation configurations explore an interesting route for exploring and determining involved mechanisms.

V.2 Statistical comparison between models and experiments

Majority of models reveal that each configuration has its own behavior, especially with regard to dislocation interactions, from which a large number of simulations are required for characterizing all possible mechanisms. Analysis of individual configurations by molecular dynamics (*e.g.* [161–164]) does not generally take or cannot take into account the influence of surrounding microstructure on local mechanisms. For example, activation of a particular slip system in a grain or interaction of a dislocation with a GB is dependent on elastic fields induced by neighboring grains, GBs, triple points and other possible defects, such as solutes or precipitates.

Few studies attempted to provide an overview of constitutive laws and theories

for modeling polycrystal plasticity [165, 166], none of them provided quantitative comparisons and statistics between these different modeling methods, which could shed new light on the inherent mechanisms. In this part, a combined experimental/theoretical approach is proposed to fill this gap.

By using information provided by *in-situ* ECCI, it is possible to examine the effect of anisotropic elastic and plastic properties on the local slip and dislocation activity distribution within grains at different stages of deformation and gather statistical information for identifying or tuning relevant micromechanical and microstructural variables that influence the material behavior.

V.2.1 Few words on the atypical plasticity of BCC metals

β-Ti21S has a BCC structure, so that it is expected that Burgers vector of dislocations is among the four dense $\langle 1\,1\,1 \rangle$. As BCC metals, such dislocations are supposed to glide in the most dense planes *i.e.* $\{1\,1\,0\}$. But packing density of $\{1\,1\,0\}$ is similar to the packing of $\{1\,1\,2\}$ and $\{1\,2\,3\}$. It has been reported from trace analyses on BCC metals that slip occurs mainly on $\{1\,1\,0\}$, $\{1\,1\,2\}$ and in some particular cases on $\{1\,2\,3\}$ planes [167]. In total, β-Ti21S has 48 slip systems available to accommodate plastic deformation. Note that at the atomic scale, slip traces consist of several atomic step combinations [168].

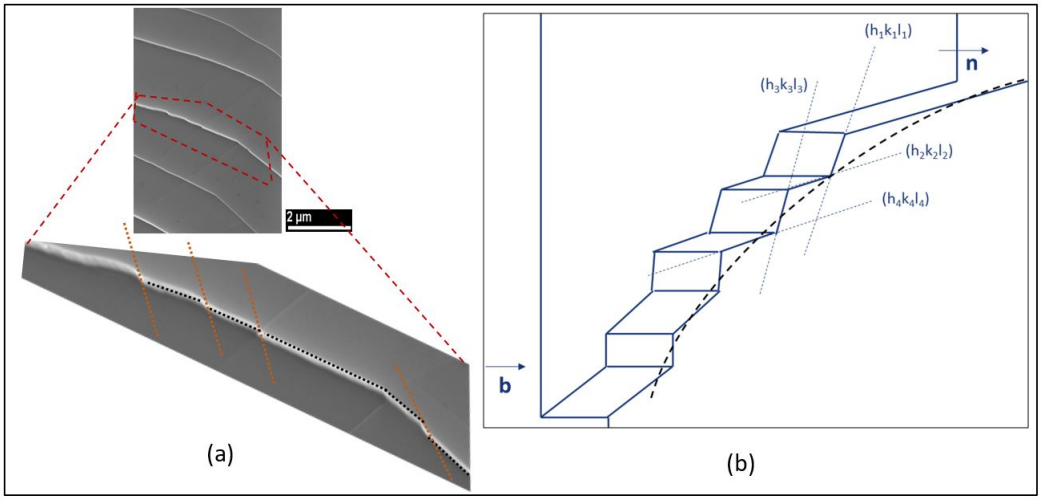

Figure V.5 – (a) SE micrographs showing curved slip lines resulting from pencil glide phenomenon and (b) a corresponding schematic representation. From [156].

Due to the multiplicity of slip planes of BCC, it is challenging to clearly identify glide planes at low temperature. Indeed, screw segments can easily cross-slip on several planes containing the same $\langle 1\,1\,1 \rangle$ as zone axis. Therefore, slip lines are curved and this phenomenon is called "pencil glide" [169–171]. By examining such curved lines at high magnification (Figure V.5), it appears that they form a stair-like shape, which results in a curved appearance when the images are taken at a lower magnification [156]. Therefore, BCC metals disobey the Schmid-Boas law, so that several modifications were proposed [172–174].

V.2.2 Feature engineering from *in-situ* ECC micrographs

Prior to any comparison, extracting relevant information from experiment data sets is necessary. Indeed, this step (*i.e.* feature engineering) is crucial. It consists in transforming experimental data into useful information that can be used afterwards. In this frame work, a novel method was developped for automated slip trace detection and analysis based on the Hough transform algorithm and apply it to ECC micrographs. This is further augmented with an automation procedure for the determination of slip-trace crystallography in conjunction with orientation data acquired via EBSD. Automation is required for faster indexation of the slip traces and for more reliable statistical studies. In concrete terms, each slip line – where coordinates of both extremities are (x_1, y_1) and (x_2, y_2) – is discretized into K points, whose the coordinates of the k^{th} points is given by [175, 176]:

$$x_k = \frac{[2^k - (2^k - 1)]x_1 + (2^k - 1)x_2}{2^k}; y_k = \frac{[2^k - (2^k - 1)]y_1 + (2^k - 1)y_2}{2^k} \tag{V.1}$$

In order to match the EBSD data with ECCI micrographs, a correlation vector, $\overrightarrow{\Pi}$ can be defined as [175, 176]:

$$\overrightarrow{\Pi} = \sum_{i=1}^{3} r_i \vec{f}_i = \sum_{i=1}^{3} \cos(\Delta\kappa_i)\vec{f}_i \tag{V.2}$$

where:

- $\vec{f_i}$ is a base vector for each family of glide planes *i.e.* $\vec{f_1} = (1,0,0)$ stands for $\{1\,1\,0\}$, $\vec{f_2} = (0,1,0)$ stands for $\{1\,1\,2\}$ and $\vec{f_3} = (0,0,1)$ stands for $\{1\,2\,3\}$;
- r_i is the i^{th} component of $\overrightarrow{\Pi}$ written in the base $(\vec{f_1}, \vec{f_2}, \vec{f_3})$;
- $\Delta\kappa_i$ is the difference between angle measured by EBSD and angle measured on ECCI micrographs for the glide plane family i, both with respect to a common direction as reference (*e.g.* the loading direction)

Because of some ambiguities to the uncertainties on the angle estimation, it is more convinient to define another correlation vector as [175, 176]:

$$\overrightarrow{\Pi'} = |\overrightarrow{\Pi} - \max[r_i] J_{3,1}| \tag{V.3}$$

where $J_{3,1}$ is a matrix of one with one column and three rows.

Therefore, the total number of counts, υ, corresponding to each family of slip planes for K points on P detected lines is [176]:

$$\overrightarrow{\upsilon}(\overrightarrow{\Pi'}) = \sum_{k=1}^{P\times K} \overrightarrow{\upsilon_k}(\overrightarrow{\Pi'}); \overrightarrow{\upsilon_k} = \frac{1}{K} \text{ or } \frac{1}{2K} \tag{V.4}$$

Finally, the probability, $\mathcal{P}_i$ of observing a slip line corresponding to a given slip plane family, i [176]:

$$\mathcal{P}_i = \frac{\upsilon_i(\overrightarrow{\Pi'})}{\sum_i \upsilon_i(\overrightarrow{\Pi'})} \tag{V.5}$$

This automation procedure is applied to different regions of interest on a β-Ti21S sample loaded *in-situ* in tension. Multiple regions of interest are analyzed. The acquired slip distribution statistics reveals that the majority of the slip traces belong mainly to the $\{1\,1\,2\}$ and $\{1\,2\,3\}$ slip families as shown in Figure V.6.

V.2.3 Comparison with micromechanical modeling

The deformation response of the observed regions of interest is also simulated using a several models/codes, with expected agreement of increasing predictions: Sachs [177], VPSC [178, 179], EVPS [180, 181] CPFFT [182, 183]. The slip system ac-

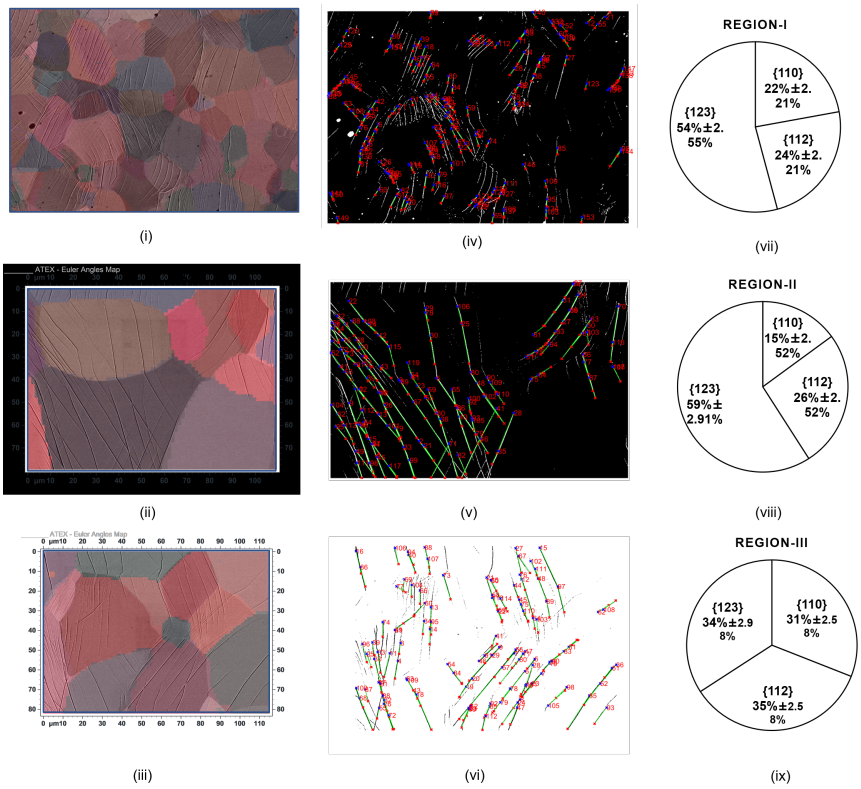

Figure V.6 – Images (i) – (iii) are EBSD maps of the deformed region of interest with the ECC micrographs of the slip traces superimposed on the EBSD maps. (iv), (v) and (vi) are the results from the automated slip line detection algorithm for these deformed regions and (vii), (viii) and (ix) are the slip family distributions obtained from these regions of interest. Adapted from [175, 176].

tivity distribution from each codes is compared with the slip distribution statistics observed experimentally. The plasticity parameters for β-Ti21S are taken from the literature [184]. Quantitative results are given in Table V.1.

From this statistical comparison, it is clear that for small plastic strains (<0.25 %) under uniaxial tensile loading, the SCHMID law is satisfied statistically. Under these circumstances, changes in CRSS are minimal and accommodation of incompatible deformation between grains has not yet become important.

Moreover, by minimizing the sum of least squared differences of $\mathcal{P}_i$ obtained either by experiments (exp) or by simulations ($simul$) for several initial CRSS ratios, *i.e.* [176]:

$$\chi = \sum_i (\mathcal{P}_i^{(exp)} - \mathcal{P}_i^{(simul)})^2 \tag{V.6}$$

Models	Error percentage
Sachs (constraint of uniform stress)	14%
VPSC (mean field)	14%
EVPSC (mean field)	10%
CPFFT (full field)	12%

Table V.1 – Statistics of predicted slip events in agreement with experimental determination. From [175].

the initial CRSS values can be also adjusted to match the slip-distribution statistics experimentally (Figure V.7) [176].

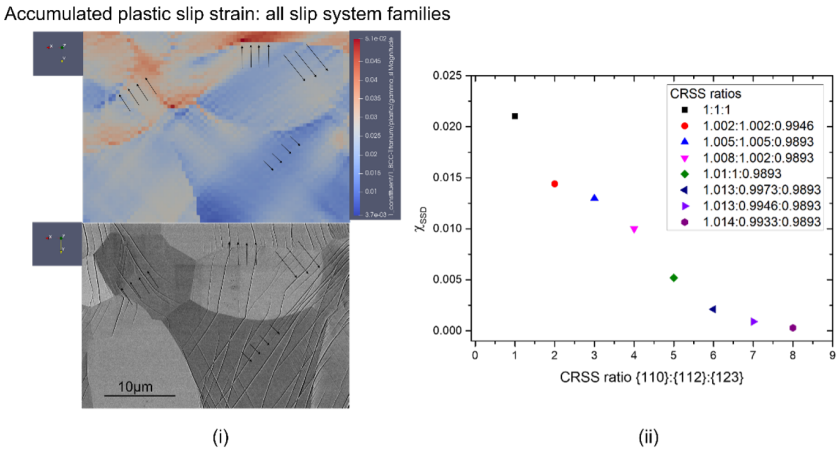

Figure V.7 – (i) The accumulated plastic slip distribution for all slip families compared to the slip-lines visible in the deformed region of interest. (ii) Sum of squared difference, (χ_{SSD}) plot for different CRSS ratios. From [176].

As the statistical distributions are being obtained from multiple points on a detected slip line, this makes the data obtained statistically relevant. It aims to be first steps towards data mining processes and model parameter optimization using a variety of different techniques [185–188].

V.2.4 Dimensionality reduction to classify different GB slip transfer regimes

Complex interactions between dislocations and GBs have a significant influence on the macroscopic properties. Therefore, it is important to understand operating

mechanisms via statistical approach for identifying important parameters originating GB-dislocation interactions. In long term, such an approach aims to build statistical criteria that can be implemented in crystal plasticity modeling and also guide microstructure tailoring. Concerning slip transfer, features span several internal length scales and hence it is difficult to develop rigorous quantification procedures that enable the visualization of correlations that exist between the different underlying parameters. In this context, a Principal Component Analysis (PCA) approach was developed [189]. PCA is a method of multivariate statistics, which consists in transforming correlated variables into new decorrelated variables, thus allowing to reduce the number of variables and to make the information less redundant. Mathematically, the problem consists in finding the eigen values and the eigen vectors of a matrix constituted with the slip-transfer metrics such as slip transmission factor ($f_{G\alpha G\beta}$), three angular variables and three geometric parameters associated with slip transfer.

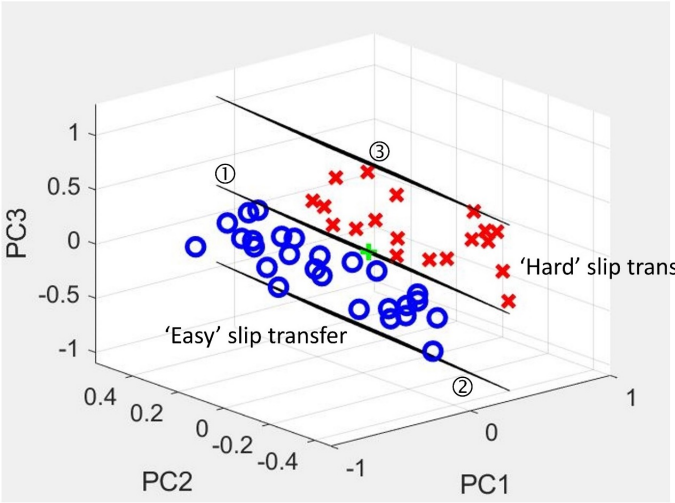

Figure V.8 – Clustering of the slip-transfer regimes in three-dimensional principal component space. Plane ① represents the separation between the two slip transfer regimes and planes ② and ③ represent the bounds for the easy and hard slip transfer regimes, respectively. From [189].

Some results from the PCA are shown in Figure V.8. Each point corresponds to a GB plotted in the principal component space. Here, the slip transmission factor $f_{G\alpha G\beta}$, defined as: (where $n_{G\alpha}$ and $n_{G\beta}$ denote the number of slip events in grains

$G\alpha$ and $G\beta$, respectively)

$$f_{G\alpha G\beta} = \begin{cases} \frac{n_{G\alpha}}{n_{G\beta}}, & \text{if } n_{G\alpha} < n_{G\beta} \\ \frac{n_{G\beta}}{n_{G\alpha}},, & \text{if } n_{G\beta} < n_{G\alpha} \end{cases} \tag{V.7}$$

is used as a classifier, with the aim of distinguishing several slip transfer regimes. The mean value of $f_{G\alpha G\beta}$ (here equal to 0.7) is related to the ease of slip transfer between the interacting grains. More precisely, a value greater than 0.7 indicates that the two interacting slip systems share the applied stress equally by the activation of close to equal number of slip systems and are classified as *easy* slip transfer events. For values less than 0.7, one of the interacting slip systems is accommodating a larger part of the applied stress, as a result of which higher number slip traces are activated for this particular slip system. They are classified as *hard* slip transfer events.

From Figure V.8, a clustering of those slip transfer regimes is obvious and they are separated by planes ①, ② and ③. As a conclusion of the procedure, the slip-transfer events can be classified based on a linear function of the input variables weighted by the loadings corresponding to each of the slip-transfer metrics. This lower-dimensional representation of the slip-transfer data can be used for estimating the slip transmission factor, $f_{G\alpha G\beta}$, for a range of active slip-systems involved in slip-transfer close to a given GB.

Chapter VI

On the importance of popularization

Both current crises (COVID pandemic and global warming) reveal the necessity of popularizing science. Not only for arousing interest for scientific careers, but also for assisting decision makers in their choices and for developing the analytic mind of populations. It is the reason why science popularization is the oldest program of UNESCO (United Nations Educational, Scientific and Cultural Organization), as crucial aspect of the democracy [190]. But it is true to say that this kind of pedagogy is under-developed in France and not well recognized by our institutions.

To perpetuate the results of my research in virtuous dynamics around the transfer of knowledge and know-how between research and society, my popularization actions are, among others, focused on two aspects, as detailed in the followings.

VI.1 Popularization for participating to scientific progress and their benefits

This action is mentioned in the article 27 of the Universal Declaration of Human Rights: "Everyone has the right freely to participate in the cultural life of the community, to enjoy the arts and to share in scientific advancement and its benefits" [191]. As scientists, we aim to change the world, but it is our responsibility to explain how we change it. The place of science in our society makes scientific knowledge the essential baggage of any future citizen, both in terms of knowledge and methods or values. Therefore, I give popularization lectures entitled *The mysteries of materials deformation in the fantasy* to high-schools. By using some famous

fantasy films/books such as *Game of Thrones* from G.R.R. Martin and *The Lord of the Rings* from J.R.R. Tolkien, I give basics of plasticity, microscopies and metallurgy. The targeted audience is the general population (adults and teenagers) without any knowledge in materials sciences (see Figure VI.1). Since 2021, my talks received the support of the French Society of Physics (SFP).

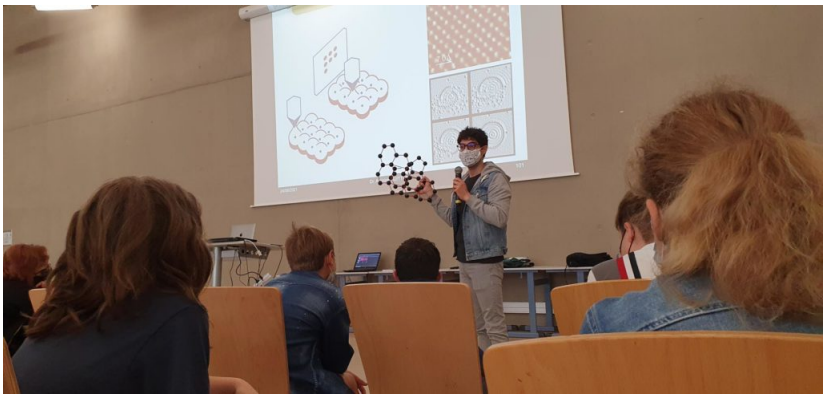

Figure VI.1 – 24/06/2021: invited talk in Vauban High-School (Luxembourg-City, Luxembourg). Photo taken by Adrien Heinzelmeier.

In addition, I do radio podcasts on science popularization (during Christmas holidays 2021: week, 7h40 and 9h40; weekend: 8h40 – from January 2022: each weekend at 7h20) entilted "La Lorraine des Sciences" ($\approx$ 3 min) at France Bleu Lorraine-Nord (see Figure VI.2).

Figure VI.2 – 03/12/2021: podcast recording at France Bleu Lorraine-Nord.

Subjects are for example:

- mechanics and microstructures of chocolate.
- how to help Santa Claus to glide in the chimney?
- what is the cold?
- etc

An experience very enriching!

VI.2 Popularization for arousing interest for scientific careers

We must admit that few students wish to become scientists and even less materials scientists. This field is unknown because it does not appear to them sufficiently important and significant. It seems "out of date" and obsolete. Therefore, intense work must be done in first years of university studies. That is why, I give some lectures in front of students. For example, from 2021, my lecture entitled *Save the world with materials science!* is included in the 1st year of BUT (Bachelor Universitaire et Technologique)-GMP. Here, I give basics of research in materials science in the framework of the current energetic transitions. The targeted audience is the students with a light scientific background.

Of course, I am aware that all these actions will not be enough. But they merit to initiate dynamics that I hope being transferred to my colleagues.

Conclusions and projects

Unearthing the missing links between, on one hand, the history of a material (its microstructure), and on the other hand, its mechanical properties and therefore its performances, is the fundamental question of materials science. Understanding how microscopic mechanisms operating against GBs evolve, while loading macroscopically a specimen and observe their series of consequences to the macroscopic scale is currently of high relevance. Indeed, mesoscale and statistical approaches are necessary to bring information allowing linking the multiscale aspects of the mechanical behavior of materials (Figure VI.3).

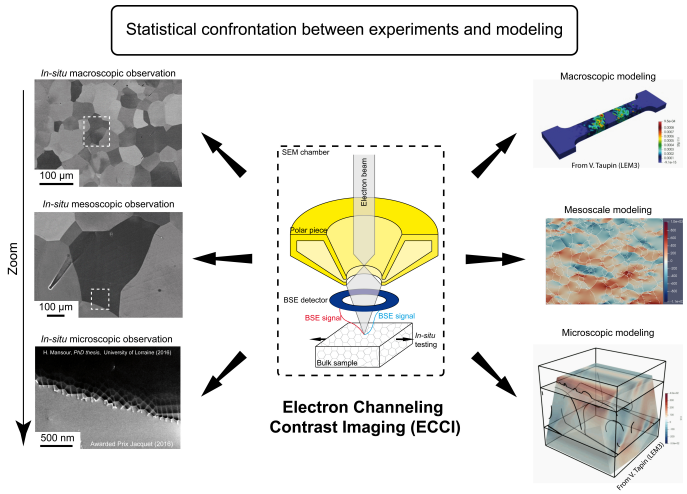

Figure VI.3 – The full potential of ECCI for multiscale confrontations between experiments and simulations.

All these aspects will have to be further explored by new frontier between ex-

periments and modeling, as motto for the next cutting-edge experiments advancing materials science especially in the customization of the microstructures according to desired performances. In this framework, some of my on-going projects or submitted are briefly described in the following.

Projects

Not available online.

Résumés en français

Résumé de mes travaux doctoraux (2010 – 2013)

Mécanismes de déformation des phases MAX

L'un des principaux défis de l'ingénierie est la nécessité d'élaborer de nouveaux matériaux qui permettent de répondre à l'évolution rapide de la société, des besoins et des nouvelles technologies. Par exemple, dans un contexte de sobriété énergétique, l'amélioration des moteurs d'avions doit passer par l'augmentation de leur température de fonctionnement. Les matériaux ainsi utilisés doivent donc être à la fois toujours plus légers et plus résistants aux hautes températures. Durant les années 90, Barsoum et *al.* de l'université Drexel à Philadelphie ont été amenés à étudier le Ti_3SiC_2 [42]. Ils ont montré que ce matériau est rigide, léger, facilement usinable, fabriqué à partir de matériaux peu coûteux, résistant à l'oxydation, aux chocs thermiques et capable de rester solide à des températures au-delà de 1300 °C dans l'air. Ils ont ainsi élaboré une cinquantaine de composés possédant des propriétés similaires. Ils ont nommé ces matériaux les phases MAX, faisant référence à leur composition (M : métal de transition ; A : élément du groupe A et X : carbone et/ou azote).

Avant toute exploitation industrielle des phases MAX, une meilleure compréhension de leurs mécanismes de déformation est essentielle. Il est couramment admis

que la déformation plastique des phases MAX est due au glissement de dislocations dans les plans de base s'organisant en empilements et murs. Ces derniers peuvent former des zones de désorientation locale appelées *kink bands*. Cependant, les mécanismes élémentaires et le rôle exact des défauts microstructuraux sont encore mal connus. C'est dans ce cadre que s'est inscrit mon travail de thèse : étudier par diverses techniques expérimentales et à différentes échelles les mécanismes de déformation des phases MAX polycristallines en général, et de la phase Ti_2AlN en particulier. À l'échelle macroscopique, deux types d'expériences ont été menés. Des essais de compression *in-situ* à température et pression ambiantes couplés à la diffraction neutronique ont permis de mieux comprendre le comportement des différentes familles de grains dans le Ti_2AlN polycristallin [51]. Des essais de compression sous pression de confinement ont également été réalisés de la température ambiante jusqu'à 900 °C [60, 62, 67]. À l'échelle mésoscopique, les microstructures des surfaces déformées ont été observées par Microscopie Électronique à Balayage (MEB) et Microscopie à Force Atomique (AFM). Ces observations complétées par des essais de nanoindentation ont montré que la forme des grains et leur orientation par rapport à la direction de sollicitation gouvernent la plasticité de ces matériaux. Finalement à l'échelle microscopique, des études détaillées par Microscopie Électronique en Transmission (MET) des échantillons déformés sous pression de confinement a révélé la présence de configurations de dislocations inédites dans les phases MAX. À la vue de ces résultats nouveaux, les propriétés mécaniques des phases MAX ont été rediscutées [62, 65, 67].

Résumé de mes travaux postdoctoraux (2014 – 2015)

Effets des changements de chemins de déformation sur la plasticité des métaux

La plupart de nos connaissances sur le comportement mécanique des métaux provient essentiellement d'essais uniaxiaux conventionnels. Cependant la production industrielle de composants métalliques implique de nombreux changements de chemins de

déformation, qui modifient drastiquement leur réponse mécanique. Dans ce cadre, les essais de déformation *in-situ* peuvent apporter de précieux renseignements sur les mécanismes de déformation qui pourraient apparaître ou pourraient être modifiés durant des changements de chemins de déformation. La miniaturisation continue des composants d'ingénierie entraîne inexorablement l'augmentation des besoins de nouveaux dispositifs de déformation à l'échelle microscopique. Mon travail post-doctoral a consisté au développement d'une nouvelle machine miniaturisée de déformation biaxiale *in-situ* qui est aussi bien compatible avec des lignes synchrotron (modes transmission et réflexion) mais également avec des observations MEB. Ces dernières nous permettent d'accéder de manière *in-situ* à la déformation dans notre zone d'intérêt par corrélation d'images numériques. Pour faire face à ce défi technologique, différentes techniques ont été développées. Notamment l'amincissement localisé des échantillons par ablation laser pulsé à pulses ultra-courts (de la femtoseconde à la picoseconde). Cette nouvelle stratégie présente essentiellement l'avantage d'usiner les échantillons en minimisant l'endommagement, ce qui en fait une excellente alternative au canon à ions focalisés ou FIB (*Focused Ion Beam*) [72]. Par ailleurs, mes simulations en éléments finis ont permis de modéliser le comportement mécanique des échantillons utilisés dans la machine de traction biaxiale, permettant ainsi d'optimiser leur forme et leur taille. Nos études *in-situ* ont été réalisées aux lignes synchrotron MS et MicroXAS du Swiss Light Source (SLS) :

- à la ligne MS : des échantillons nanocristallins de nickel et d'aluminium ont été étudiés avec un faisceau X monochromatique ;
- à la ligne MicroXAS : des échantillons d'aluminium monocristallins et bicristallins sont analysés par microdiffraction Laue.

Les résultats expérimentaux sont alors discutés en parallèle avec ceux obtenus en simulations et permettent d'apporter des éclairages nouveaux sur l'influence des changements de chemins de déformation sur l'activation des systèmes de glissement de dislocations, les Joints de Grains (JdG) ainsi que sur la formation de contraintes résiduelles [73].

Résumé de mes travaux comme maître de conférences (depuis 2015)

Étude des mécanismes de déformation par imagerie de canalisation des électrons

Bien que la mécanique des matériaux soit agée de plus d'un siècle, elle reste encore confrontée à de nombreux défis conceptuels. Il faut, en effet, relier deux échelles extrêmes : l'échelle de l'échantillon (c.-à-d. macroscopique) et l'échelle des mécanismes fondamentaux (c.-à-d. microscopique). De plus, les statistiques d'observations sont généralement extrêmement faibles, si bien que d'une part l'incertitude est élevée et d'autre part la représentativité des mécanismes est très discutable.

Dans le cadre d'une part des recherches doctorales de Hana Kriaa (2015–2018) et de Frederic Habiyaremye (2018-2022) – co-directions avec Dr. Nabila Maloufi – et d'autre part des recherches postdoctorales de Meriem Ben Haj Slama (2018-2020), j'ai initié la combinaison d'essais mécaniques (nanoindentation et de traction *in-situ*) d'échantillons massifs avec une technique de caractérisation à l'échelle des dislocations : l'imagerie par contraste de canalisation des électrons (*Accurate Electron Channeling Contrast Imaging*: A-ECCI) [128, 148, 156]. L'A-ECCI est une procédure non destructive, qui a été développée au LEM3 avant mon arrivée [95, 96]. Elle offre la possibilité de fournir, à l'intérieur d'un MEB, une imagerie par contraste de diffraction de type MET des défauts de sous-surface (jusqu'à une profondeur d'environ 100 nm) sur un échantillon massif centimétrique avec des résolutions encore inégalées. Ainsi, nous avons été les pionniers à relier l'aspect multi-échelle de la plasticité des matériaux (de l'échelle de la dislocation à l'échelle de l'échantillon) [156].

La première partie de mon travail a consisté à comprendre la physique du contraste des défauts dans le but d'optimiser les procédures expérimentales (recherche doctorale de Hana Kriaa 2015–2018, co-direction avec Dr. Nabila Maloufi) [104–106]. Ceci m'a naturellement conduit à proposer d'explorer le potentiel de l'A-ECCI

afin suivre l'évolution des microstructures de déformation.

Avec les chercheurs postdoctoraux que j'ai encadrés (recherches postdoctorales de Meriem Ben Haj Slama 2018–2020 et de Kaustubh Venkatraman 2020–2022), nous avons développé une méthode de détection automatisée, basée sur un algorithme de transformée de Hough, des traces de glissement (dislocations et marches en surface) apparaissant lors de la déformation *in-situ* d'un alliage de Ti cubique centré (Ti21S) [175, 176]. La distribution des systèmes de glissement actifs obtenue à partir d'une loi micromécanique à champ complet a ensuite été comparée statistiquement à la distribution des systèmes de glissement observée expérimentalement par A-ECCI. Notre méthode nous a notamment permis d'ajuster les cissions projetées critiques en comparant les statistiques des distributions de glissement (sur environ 3000 points), obtenues d'une part par la loi micromécanique, et d'autre part expérimentalement. Ainsi ces comparaisons statistiques entre les modèles de plasticité cristalline et les expériences se veulent être une première étape vers l'ingénierie des fonctionnalités.

Mon projet scientifique d'HDR

Approches expérimentales, mésoscopiques et statistiques de la plasticité dans les polycristaux

Déformation des matériaux : un défi multi-échelle et statistique

Développer de nouveaux matériaux et comprendre comment ils se déforment est le principal défi des chercheurs pour suivre et prédire l'évolution rapide de notre société. Par exemple, dans un cadre de réduction des coûts énergétiques, l'augmentation des performances mécaniques des matériaux est conditionnée à l'amélioration constante des techniques expérimentales conduisant à de nouvelles connaissances sur leurs mécanismes fondamentaux de déformation. Bien que la recherche en plasticité des matériaux soit âgée de plus d'un siècle, il est juste de dire qu'elle recèle encore de nombreux secrets, notamment en raison des difficultés à extrapoler des modèles

simplistes à des échantillons réels, loin des cas idéaux. Cottrell a résumé ce conflit en qualifiant la théorie de l'écrouissage plastique comme "*the first problem to be attempted by dislocation theory and may be the last to be solved*" [3].

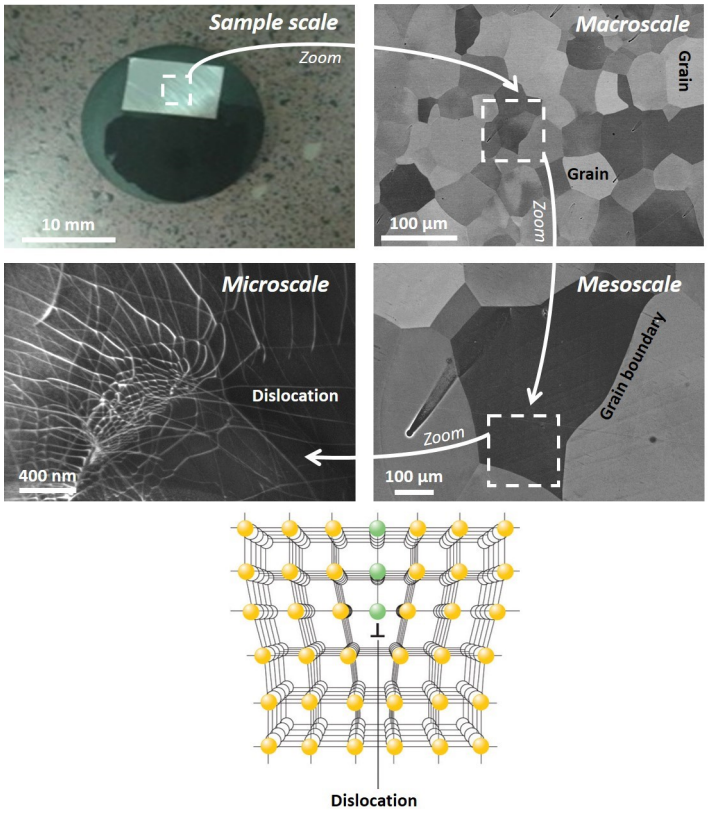

Transitions d'échelles en Sciences des Matériaux.

En effet, la mécanique des matériaux doit encore faire face à de nombreux problèmes conceptuels. Nous devons ainsi relier deux échelles extrêmes : l'échelle de l'échantillon (c.-à-d. Macroscopique) et l'échelle des mécanismes fondamentaux (c.-à-d. Microscopique). De plus, la statistique des observations est généralement extrêmement faible de sorte que d'une part l'incertitude est importante et d'autre part la représentativité des mécanismes est très discutable. La statistique de Cocheran explique parfaitement ce problème [192] : si un phénomène est observé à partir d'un échantillonnage d'expériences, alors il est impossible d'être sûr à 100 % que le phénomène observé soit une représentation complète et exacte du comportement étudié. Par exemple, en considérant un niveau de confiance de 90 %, cela signifie qu'en répétant l'expérience un certain nombre de fois, 90 % du temps les mêmes

résultats seront obtenus. En raison de ces problèmes conceptuels, des études significatives et statistiques sont alors nécessaires pour établir des modèles représentatifs basés sur le lien entre des paramètres importants à basse échelle et des propriétés à plus grande échelle.

La plupart des matériaux utilisés sont généralement polycristallins [9]. Ces derniers se composent de millions de monocristaux appelés grains. Les grains ont des orientations différentes du réseau atomique et ils sont séparés des grains voisins par des interfaces appelées JdG. Il est bien établi que la déformation irréversible (ou plastique) d'un échantillon provient principalement de la nucléation et de la propagation de plus de centaines de milliards par cm^3 de défauts linéaires micrométriques (voire nanométriques) du réseau cristallin régulier appelé dislocations [4]. Les dislocations se déplacent dans le grain et interagissent les unes avec les autres ou avec les JdG. Ces derniers peuvent agir de plusieurs manières : puits, pièges, obstacles et sources de dislocations. La combinaison d'études expérimentales et de simulations donne des informations précieuses sur les mécanismes fondamentaux de déformation.

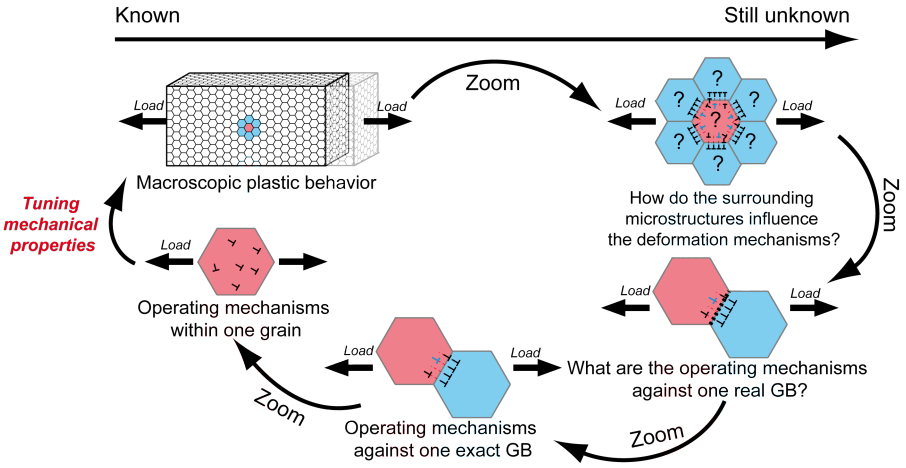

Derniers défits de plasticité des matériaux.

De nos jours, on sait presque comment une dislocation interagit avec un JdG modèle, mais comprendre la réponse de plusieurs JdG réels (contenus dans un véritable échantillon polycristallin massif) après avoir reçu de nombreuses dislocations reste un défi scientifique majeur. Le mystère devient inextricable, quand on considère, qu'il y a plus de centaines de milliards de dislocations par cm^3 d'échantillon

interagissant entre eux et avec des milliards de JdG... Encore plus inextricable, si l'on veut prendre en compte l'influence de la distribution des JdG, d'autres types d'interfaces, de la forme du grain, de l'orientation du grain et des défauts, c.-à-d. sa microstructure. En raison de cette complexité inhérente, les scientifiques des matériaux doivent relier deux échelles extrêmes : l'échelle de l'échantillon (ou macro-) et l'échelle de dislocation (ou micro-).

Il est évident que ces deux mondes interagissent, mais leurs connexions restent extrêmement difficiles à comprendre en raison du besoin d'extrapolations.

Apport de la modélisation

La modélisation micromécanique apporte de nouvelles perspectives. De telles stratégies de calcul nécessitent des équations constitutives, qui doivent être "alimentées" avec des critères et des paramètres expérimentaux, capturant des mécanismes opératoires.

Il est clair que la réponse d'un grain d'intérêt dans un échantillon polycristallin ne peut être comprise individuellement sans tenir compte de son voisinage.

Deux types de configurations de dislocation sont distingués, dont à la fois l'évolution de la densité et leurs interactions spécifiques peuvent être modélisées [28] : les densités de dislocations géométriquement nécessaires (GND) entraînent une désorientation d'un volume élémentaire de référence afin d'accommoder géométriquement la déformation de l'échantillon (effet longue portée). L'autre type de dislocations est appelé dislocations stockées statistiquement (SSD). Ces dernières ne contribuent pas à la désorientation du réseau cristallin, mais elles peuvent entraîner l'épinglage des dislocations (effet à courte portée).

Les résultats expérimentaux à une échelle intermédiaire, c.-à-d. mésoscopique, peuvent être utilisés pour améliorer nos connaissances sur la plasticité polycristalline et pour améliorer les modèles à l'échelle des grains [30–36]. Ils fournissent, en effet, des données de validation pour des simulations numériques avancées qui prédisent le comportement mécanique des polycristaux, vis-à-vis de l'évolution des densités de dislocation à l'intérieur des grains et de leurs interactions avec les JdG. Les outils

de modélisation comprennent des modèles de dynamique des dislocations discrètes (*Discrete Dislocation Dynamics* : DDD), de plasticité cristalline (*Crystal Plasticity* : CP) basés sur des éléments finis (*Crystal Plasticity based on Finite Elements* : CPFEM) ou des algorithmes de transformées de FOURIER rapide (*Crystal Plasticity based on Fast FOURIER Transform* : CPFFT) ou des approches de champ moyen (par exemple, des modèles auto-cohérents tels que le *ViscoPlastic Self-Consistent* (VPSC) et les modèles auto-cohérents élasto-visco-plastique (*Elasto-Visco-Plastic Self-Consistent* : EVPSC) [37]. Des études récentes ont été menées dans le but de coupler des modèles à des expériences telles que CPFEM (ou CPFFT) avec l'EBSD (*Electron BackScatter Diffraction*), ou CPFEM avec corrélation d'image numérique haute résolution *High-Resolution Digital Image Correlation* : HRDIC). Ces approches couplées peuvent fournir des informations sur les textures, la configuration de densité de GND, la localisation des déformations plastiques et le transfert à travers les JdG, etc [38–41]. Parmi les résultats, de telles méthodes couplées de modélisation-expérimentale montrent qu'il est possible de lier l'évolution microstructurale au comportement contrainte-déformation. Cependant, ces expériences sont encore marginales et souffrent toutes de nombreuses contraintes rendant les interprétations non fiables.

Limite des techniques existantes

La MET est l'une des techniques les plus connues pour observer et caractériser les dislocations dans des lames minces transparentes aux électrons (épaisseur de ≈ 100 nm avec un champ de vision utile de quelques µm) [75, 76]. Des études détaillées des dislocations à l'échelle microscopique apportent, en effet, des informations précieuses pour l'extrapolation de la réponse mécanique macroscopique des matériaux et peuvent alimenter des modèles numériques avancés de plasticité cristalline [49, 60, 62, 65, 67]. Les essais mécaniques *in-situ* au MET sont bien connus pour étudier l'évolution des défauts cristallins sous contrainte [77–80]. Différentes approches de test mécanique à l'intérieur d'un MET existent. Néanmoins, les essais mécaniques en MET *in-situ* sont expérimentalement difficiles et ne reflètent pas

nécessairement la réponse macroscopique d'un matériau [81]. Outre le contrôle difficile des conditions de déformation, l'espace disponible à l'intérieur de la chambre du microscope est généralement inférieur à un centimètre cube et les statistiques sur les mécanismes physiques sont faibles. En effet, le MET nécessite l'utilisation de lames minces transparentes aux électrons d'une épaisseur de ≈100 nm avec un champ de vision utile de quelques µm. Par conséquent, des questions fondamentales concernant la représentativité des phénomènes observés doivent être soulevées lors de l'extrapolation des discussions à un échantillon de taille millimétrique ou plus (échelle centimétrique, test macroscopique).

En plus du MET, des essais mécaniques couplés à la diffraction des rayons X (en particulier la diffraction de Laue) ou à l'EBSD peuvent fournir des informations précieuses sur les mécanismes fondamentaux pouvant ainsi alimenter des modèles [51, 72, 83, 85, 88, 111, 112, 114]. Cependant, ces deux techniques ne sont sensibles qu'aux variations de la densité de GND. Par conséquent, une partie du problème est passée sous silence (c.-à-d. les SSD).

A travers ce panorama, il est clair que les techniques actuelles ont atteint leurs limites. Nous devons faire face au conflit suivant : si la technique (Laue ou EBSD) est statistiquement représentative, certaines informations seront manquantes et si la technique permet de capturer toute l'information (MET), sa représentativité statistique est très faible.

À l'aide de procédures originales rendues désormais possibles grâce aux progrès récents de la microscopie électronique, ces obstacles sont en passe d'être surmontés. Tel est le contexte de mon travail.

Le MEB est un microscope électronique plus flexible par rapport au MET, essentiellement en raison de l'espace plus grand disponible dans la chambre. Le MEB peut accéder au contraste de diffraction sur des matériaux massifs avec le phénomène de la canalisation des électrons [90, 91]. La canalisation des électrons se produit quand les électrons suivent des chemins formés par les plans cristallins, pénétrant ainsi dans le matériau avant d'être rétrodiffusés. La profondeur de pénétration dépend, entre autres, de l'orientation cristalline, si bien que certains grains rétrodiffusent

plus d'électrons que d'autres, donnant ainsi lien à un contraste d'orientation. En exploitant ce phénomène, la technique ECCI permet d'observer et de caractériser les défauts cristallins dans un échantillon massif jusqu'à une profondeur d'une centaine de nanomètres sous la surface. Pour comprendre l'origine des contrastes ECCI, la physique de l'ECCI a été au cœur des mes premiers travaux au LEM3, afin de comprendre et d'optimiser les conditions expérimentales (recherche doctorale de Hana Kriaa 2015–2018, co-direction avec Nabila Maloufi) [104–106].

Approche expérimentale et mésoscopique des mécanismes de déformation au voisinage d'une interface réelle

Fort de ces travaux, j'ai initié, comme perspective de la thèse de Hana Kriaa, la Recherche sur l'exploration de la potentialité de l'A-ECCI pour suivre l'évolution des défauts cristallins combinée avec des essais de déformation localisée par nanoindentation au voisinage d'une interface (recherche doctorale de Frederic Habiyaremye 2018–2012, co-direction avec Nabila Maloufi) [128, 148]. L'essai de nanoindentation est un essai de déformation localisée sur un échantillon massif. Il consiste, comme dans le cas de la mesure de dureté, à faire pénétrer une pointe dans un matériau pour en déduire ses propriétés mécaniques. L'évolution de la force appliquée sur la pointe d'indentation et son enfoncement dans le matériau sont mesurés en continu, sur un cycle charge-décharge. Les charges appliquées restent faibles, allant de la centaine de micronewtons à la centaine de millinewtons. Cette combinaison expérimentale a ouvert la voie à l'étude des mécanismes proches d'un JdG unique sont discutés dans le cadre, d'une part, d'un alliage TiAl et d'autre part, d'un alliage à entropie moyenne.

Les alliages d'aluminure de titane ont attiré une attention considérable en raison de leur combinaison unique de propriétés telles qu'une limite d'élasticité élevée, de bonnes propriétés de fluage et une résistance à l'oxydation et à la corrosion qui en font des matériaux candidats appropriés pour applications aux hautes températures [120]. Citons par exemple, les pales de la turbine basse pression de la dernière génération de moteurs d'avion (GEnx, *General Electric Next-generation* et LEAP,

Leading Edge Aviation Propulsion) qui sont fabriquées en alliage d'aluminure de titane GE (*General Electric*) remplaçant ainsi les superalliages à base Ni, deux fois plus lourds. Nos essais de nanoindentation combinés aux observations A-ECCI avant et après la déformation ont pu suggérer qu'à température ambiante, le maclage semble être le mécanisme principal de déformation et qu'une paroi de macle est un obstacle à la propagation de la déformation entrainnant une concentration de contraintes au niveau de la paroi [128].

Concernant les alliages à entropie moyenne (MEA : *Medium Entropy Alloy*) et les alliages à haute entropie (HEA : *High Entropy Alloy*), ils se composent respectivement de deux à quatre et d'au moins cinq éléments, avec des concentrations presque équiatomiques. Parmi ces nouvelles classes de matériaux, le CrMnFeCoNi et l'un de ses dérivés ternaires équiatomiques, le CrCoNi, suscitent actuellement un intérêt croissant dans la littérature en raison de leurs excellentes tolérances aux dommages aux basses voire très basses températures [137]. En comparant les courbes de nanoindentation, les charges des *pop-in* initiaux et les configurations des dislocations pour les empreintes effectuées à l'intérieur des sous-grains, sur un JdG de faible désorientation et proche de ce dernier, on constate que le JdG de faible désorientation étudié affecte la réponse micromécanique locale et les mécanismes de déformation fondamentaux sous-jacents [148].

Comparaison statistique entre les expériences et les modèles mésoscopiques de plasticité polycristalline

Dans les métaux, les mécanismes élémentaires comme le glissement de dislocations, opèrent à l'échelle atomique voire à l'échelle électronique ; typiquement, l'ångström et la picoseconde. Ces mécanismes peuvent fortement influer sur la réponse macroscopique à l'échelle du laboratoire, c.-à-d. le centimètre et la seconde. Par exemple, des simulations *ab-initio* des cœurs de dislocations dans des métaux cubiques centrés ont mis en évidence l'apparition d'effets non-Schmid, qui pourraient expliquer une asymétrie entre la traction et la compression à l'échelle macroscopique [173]. Pour comprendre et finalement contrôler le comportement mécanique des matéri-

aux métalliques en ce qui concerne leurs microstructures traitées, il faut faire face à ce problème multi-échelles d'une complexité impressionnante qui peut s'étendre sur plus de 10 ordres de grandeur dans le temps et dans l'espace. C'est pourquoi des outils théoriques et expérimentaux avancés sont constamment développés, visant à relier les échelles de longueur pertinentes et à comprendre les mécanismes impliqués.

Dans ce contexte, j'ai ouvert la voie vers le développement d'essais macroscopiques de traction uniaxiale d'un échantillon massif combiné à des observations *in-situ* à l'échelle de dislocation de l'évolution des microstructures de déformation pendant le chargement à plusieurs états de contrainte [156]. Les observations à l'échelle des dislocations ont été réalisées par A-ECCI afin de suivre l'évolution des défauts et leurs interactions avec les JdG pour plusieurs régions d'intérêt pendant le chargement macroscopique. Nous avons, entre autres, développé une méthode de détection automatisée des traces de glissement (dislocations et marches en surface) apparaissant lors de la déformation *in-situ* d'un alliage de Ti cubique centré (Ti21S). La distribution des systèmes de glissement actifs obtenue à partir d'une loi micromécanique à champ complet a ensuite été comparée statistiquement à la distribution des systèmes de glissement observée expérimentalement par A-ECCI [175]. Notre méthode nous a notamment permis d'ajuster les cissions projetées critiques initiales en comparant les statistiques des distributions de glissement (sur environ 3000 points), obtenues d'une part par la loi micromécanique, et d'autre part expérimentalement. Ainsi ces comparaisons statistiques entre les modèles de plasticité cristalline et les expériences se veulent être une première étape vers l'ingénierie des fonctionnalités [176].

Retombées de mon projet

À travers cet aperçu synthétique, il est clair que la déformation des matériaux est un problème de voisinage multi-échelle et statistiquement complexe. Multi-échelle, car il faut être capable d'appréhender la plasticité à toutes les échelles où elle se déroule. Complexe car les microstructures environnantes influencent profondément la réponse des grains, et c'est la combinaison de tous les grains qui donne le comportement

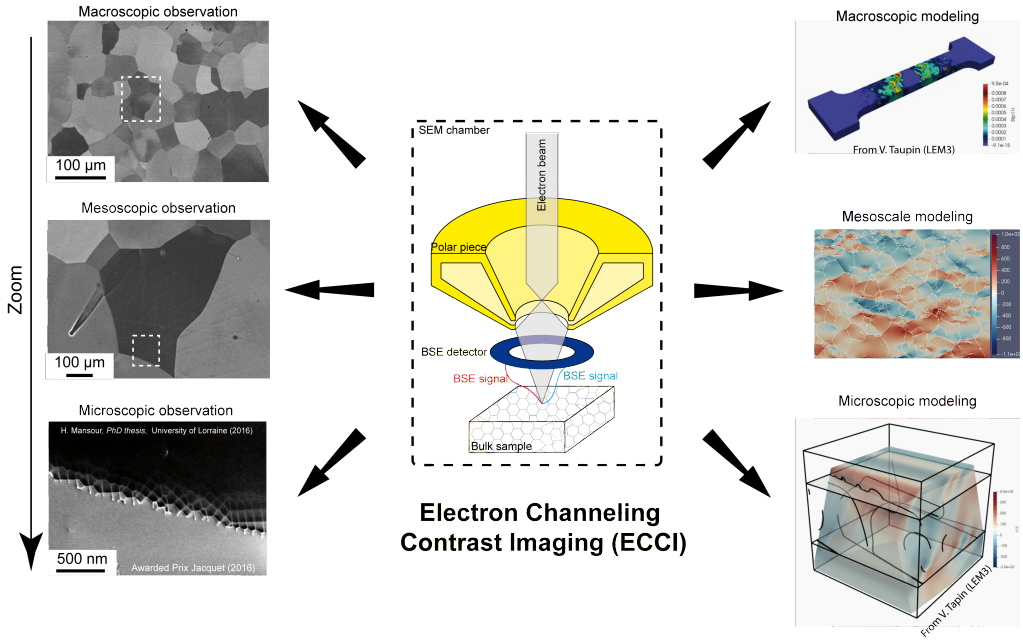

Ma stratégie pour comprendre la plasticité des matériaux.

macroscopique. D'un côté, la réponse macroscopique d'un échantillon est connue ; de l'autre côté, les mécanismes opérant à l'intérieur d'un grain sont plus ou moins bien compris. Mais tout l'enjeu dans la compréhension de ce qui se passe entre ces deux échelles. De plus, nous n'avons aucune idée si les mécanismes rapportés sont anecdotiques ou non, en raison des faibles statistiques d'observations. Il est vrai que plusieurs lois ou modèles ont déjà été proposés. Dans plusieurs cas, ils ont prouvé leur efficacité pour prédire quels mécanismes seront activés. Mais dans de nombreux autres, ils ne fonctionnent tout simplement pas.

Ainsi, je vise à améliorer les modèles constitutifs de plasticité en prenant en compte statistiquement la microstructure. En effet, comprendre comment évoluent les mécanismes de déformation lors du chargement macroscopique d'un échantillon et observer leur série de conséquences à l'échelle macroscopique est le chaînon manquant. Cette amélioration passera inéductablement par des algorithmes d'apprentissage profond. Expérimentalement, un large jeu de données sera nécessaire pour vérifier/corriger le modèle/les paramètres, afin de devenir très prédictif et ensuite être utilisé, à terme, pour la sélection de microstructures. En ce sens, l'ECCI et plus largement le MEB, aura une place prépondérante.

À partir de nos résultats, il sera possible d'étudier et voire même de comprendre la plasticité à toutes les échelles où elle se déroule, ouvrant ainsi de nouvelles pistes de recherche. Alors seulement, nous serons en mesure sélectionner judicieusement voire de personnaliser les microstructures en fonction des performances souhaitées, de la même manière que les fameux graphes d'Ashby pour la sélection des matériaux.

Curriculum vitae and teaching

Personal information

GUITTON, Antoine
Tenured Associate Professor
Université de Lorraine – CNRS – Arts et Métiers – Laboratory of studies of microstructures and mechanics of materials (LEM3)
Age: 34 years old
Nationality: French
orcid.org: 0000-0002-1508-787X
Webpage: www.antoine-guitton.fr

Education

2010 – 2013 *PhD in material physics*

Université de Poitiers, France

Directors: Prof. Anne Joulain, Prof. Ludovic Thilly, Prof. Christophe Tromas;

Reviewers: Prof. Michel W. Barsoum (Drexel University, USA); Prof. Florence Pettinari-Sturmel (Université de Toulouse III, Fance);

Examiners: Prof. Patrick Cordier (Université de Lille I, France); Dr. Véronique Gauthier-Brunet (Université de Poitiers, Fance); Prof. Helena Van Swygenhoven (EPFL/PSI, Switzerland).

2010 *Master in material physics*
Université de Poitiers, France

Research experience

From 2015 *Tenured Associate Professor*

Research: Université de Lorraine – CNRS – Arts et Métiers – LEM3, France

Teaching: Université de Lorraine – IUT (*Institut Universitaire et Technologique*) de Metz, GMP (*Génie Mécanique et Productique*: Mechanical engineering and automated production), France

2014 – 2015 *Postdoctoral Researcher*

Paul Scherrer Institut, Villigen, Switzerland

Supervisor: Prof. Helena Van Swygenhoven.

Topic: Multiaxial and multiscale plasticity in metals.

2010 – 2013 *Doctoral Researcher*

Université de Poitiers – CNRS – ISAE-ENSMA – Institut Pprime, Poitiers, France

Directors: Prof. Anne Joulain, Prof. Ludovic Thilly, Prof. Christophe Tromas;

Topic: Deformation mechanisms of MAX phases.

Research subjects: Fundamental deformation mechanisms of materials, Plasticity, Microstructures, Materials characterization, Metallurgy, Micromechanics, Hydrogen storage in metals, Scanning Electron Microscopy, Transmission Electron Microscopy, Development of experimental techniques, Neutron diffraction, Micro-Laue diffraction, Metals, Ceramics.

Research supervision

Doctoral researchers	H. Kriaa (2015 – 2018: ministerial grant, Université de Lorraine, co-direction with Dr. N. Maloufi), F. Habiyaremye (2018 – 2022: ministerial grant, Université de Lorraine, co-direction with Dr. N. Maloufi), A. Heinzelmeier (2020 – 2023: CNRS MITI grant, Université de Lorraine, co-direction with Prof. T. Grosdidier), J. Aubourg (2021 – 2024: CIFRE with JEOL SAS, Université de Lorraine, co-direction with Prof. E. Bouzy), R. Genin (2021 – 2024: LabEx DAMAS/INTERACTIFS grants, Université de Poitiers, co-direction with Prof. L. Pichon).
Postodoctoral researchers:	C. Zhang (2018 – 2019: Regional and EPFL funding), M. Ben Haj Slama (2018 – 2020: LabEx DAMAS and Regional funding), H. Kriaa (2018 – 2020: ATER and LabEx DAMAS funding), K. Venkatraman (2020 – 2022: LabEx DAMAS and Regional funding).

Teaching experience

In my opinion, teaching is very formative both on the human level and on knowledge. The contact with students, the management of a group, the presentation efforts are all experiences that allow me to usefully supplement my research work.

2021 – 2022	*IUT de Metz – GMP, France* $\approx$ 300 h **Topics:** continuum mechanics, fluid mechanics, metrology, microscopies **Audience:** 1st, 2nd and 3rd years of Bachelor.
2021	*Beijing Jiaotong University, China* 16 h (online) **Topics:** Electron microscopies: a powerful tool for understanding the fundamental deformation mechanisms of materials **Audience:** Master and doctoral researchers.

2020 – 2021 *IUT de Metz – GMP, France*

434 h (including ≈ 50 h of pedagogical responsabilies)

Topics: continuum mechanics, fluid mechanics, metrology, microscopies

Audience: 1st, 2nd and 3rd years of Bachelor.

2019 – 2020 *IUT de Metz – GMP, France*

464 h (including ≈ 50 h of pedagogical responsabilies)

Topics: continuum mechanics, fluid mechanics, metrology, microscopies

Audience: 1st, 2nd and 3rd years of Bachelor.

2018 – 2019 *IUT de Metz – GMP, France*

354 h (including ≈ 50 h of pedagogical responsabilies)

Topics: continuum mechanics, fluid mechanics, metrology, microscopies

Audience: 1st, 2nd and 3rd years of Bachelor.

2017 – 2018 *IUT de Metz – GMP, France*

316 h (including ≈ 50 h of pedagogical responsabilies)

Topics: continuum mechanics, fluid mechanics, metrology, microscopies, thermodynamics

Audience: 1st, 2nd and 3rd years of Bachelor.

2016 – 2017 *IUT de Metz – GMP, France*

299 h (including ≈ 30 h of pedagogical responsabilies)

Topics: continuum mechanics, fluid mechanics, metrology, thermodynamics

Audience: 1st and 2nd years of Bachelor.

2015 – 2016 *IUT de Metz – GMP, France*

359 h (including ≈ 20 h of pedagogical responsabilies)

Topics: fluid mechanics, metrology, thermodynamics

Audience: 1st and 2nd years of Bachelor.

Complementary to my teaching, I attach great importance to the popularization of

science. I am involved in several actions such as invited talks entitled *The mysteries of materials deformation in the fantasy* in high schools. My lectures received the support of the French Society of Physics (SFP) and they are now included in the 1st year of BUT (Bachelor Universitaire et Technologique)-GMP as an initiation to science.

- **2021:** Weekly podcasts at France Bleu Lorraine-Nord (Metz, France)
- **2021:** Lecture during the Science Day (Metz, France)
- **2021:** One-to-one with a researcher: research in materials science for energy transitions (Metz, France)
- **2021:** Interview on France Bleu Lorraine-Nord (regional radio) about materials science in energy transition: link to the podcast (in French)
- **2021:** Lecture at Collège-Lycée Vauban (Luxembourg-City, Luxembourg)
- **2020:** Chercheur.e dans ma ville and video on the research in materials science (with Dr. N. Gey): link to the video (in French)
- **2019:** Lecture during the Science day (Metz, France)
- **2018:** Lecture at Lycée Fabert (Metz, France)
- **2018:** Lecture during the Science day (Metz, France)
- **2018:** Lecture at Lycée de la Communication (Metz, France)
- **2017:** Lecture during the Science day (Metz, France)
- **2016:** Lecture at Université de Lorraine – IUT de Metz, MP (Metz, France)

Peer-reviewed publications

Updated list on my webpage: www.antoine-guitton.fr.

27. Brittleness of metallic ceramics: surface severe plastic deformation on Ti_2AlC and its $TiAl_3$ intermetallic composite.
A. Heinzelmerier, M. Novelli, A. Guitton, W. Yu, T. Grosdidier
TO BE SUBMITTED

26. Influence of the configurations of dislocations on the pop in load during nanoindentation in a CrCoNi medium entropy alloy.
F. Habiyaremye, A. Guitton, X. Lei, T. Richeton, S. Berbenni, G. Laplanche, N. Maloufi
TO BE SUBMITTED

25. Dimensionality reduction using principal component analysis to classify different grain boundary slip transfer regimes in BCC-titanium Ti21S: a feature engineering-based approach.
K. Venkatraman, V. Taupin, A. Guitton
UNDER REVIEW
⟨hal-03372274⟩

24. Reorganization of the microstructure gradient after uniaxial micro-tensile testing on thin wall Inconel 718 printed by laser powder bed fusion.
L. Decluse, M. Ben Haj Slama, S. Bahi, A. Guitton, P. Wood, N. Maloufi, A. Rusinek
IN REVISION
⟨hal-03381828⟩

23. Features of a nano-twist phase in the nanolayered Ti_3AlC_2.
J. Guénolé, V. Taupin, M. Vallet, W. Yu, A. Guitton
SCRIPTA MATERIALIA, 2022, 210, 114425
DOI: 10.1016/j.scriptamat.2021.114425
⟨hal-03207521⟩

22. Effects of A-site atoms in Ti2AlC and Ti_3SiC_2 MAX phases reinforced Mg composites: interfacial structure and mechanical properties.
W. Yu, X. Pi, W. Chen, M. Vallet, A. Guitton, L. Zhang
MATERIALS SCIENCE AND ENGINEERING A, 2021, 141961
DOI: 10.1016/j.msea.2021.141961
⟨hal-03323800⟩

21. Plasticity induced by nanoindentation in CrCoNi medium-entropy alloy studied by accurate electron channeling contrast imaging revealing dislocation-low angle grain boundary interactions.
F. Habiyaremye, A. Guitton, F. Schäfer, F. Scholz, M. Schneider, J. Frenzel, G. Laplanche, N. Maloufi
MATERIALS SCIENCE AND ENGINEERING A, 2021, 817, 141364
DOI: 10.1016/j.msea.2021.141364
⟨hal-03118990⟩

20. Tuning critical resolved shear stress ratios for BCC-Titanium Ti21S via an automated data analysis approach.
K. Venkatraman, M. Ben Haj Slama, V. Taupin, N. Maloufi, A. Guitton
MODELLING AND SIMULATION IN MATERIALS SCIENCE AND ENGINEERING, 2021, 29 (5), 055014
DOI: 10.1088/1361-651X/abfeb0
⟨hal-03119000⟩

19. Modelling electron channeling contrast intensity of stacking fault and twin boundary using crystal thickness effect.

H. Kriaa, A. Guitton, N. Maloufi
MATERIALS, 2021, 17 (7), 1696
DOI: 10.3390/ma14071696
⟨hal-03118996⟩

18. Electron Channeling Constrast Imaging characterization and crystal plasticity modeling of dislocation activity in Ti21S BCC materials.
M. Ben Haj Slama, V. Taupin, N. Maloufi, K. Venkatraman, A.D. Rollett, R.A. Lebensohn, S. Berbenni, B. Beausir, A. Guitton
MATERIALIA, 2021, 100996
DOI: 10.1016/j.mtla.2020.100996
⟨hal-03094460⟩

17. Frank partial dislocation in Ti_2AlC induced by matrix-Cu diffusion.
W. Yu, J. Guénolé, J. Ghanbaja, M. Vallet, A. Guitton
SCRIPTA MATERIALIA, 2021, 19, 34-39
DOI: 10.1016/j.scriptamat.2020.09.007
⟨hal-02940841⟩

16. Study of Mg-Al-Ca magnesium alloy ameliorated with designed Al8Mn4Gd phase.
C. Ma, W. Yu, X. Pi, A. Guitton
JOURNAL OF MAGNESIUM AND ALLOYS, 2020, 8, 1084-1089
DOI: 10.1016/j.jma.2020.08.009
⟨hal-03039711⟩

15. Processing and mechanical properties of Ti2AlC MAX phase reinforced AE44 magnesium composite.
X. Pi, W. Yu, C. Ma, X. Wang, S. Xiong, A. Guitton
MATERIALS, 2020, 13 (4), 995
DOI: 10.3390/ma13040995
⟨hal-02495138⟩

14. In situ macroscopic tensile testing in SEM and Electron Channeling Contrast Imaging: pencil glide evidenced in a bulk beta-Ti21S polycrystal.
M. Ben Haj Slama, N. Maloufi, J. Guyon, S. Bahi, L. Weiss, A. Guitton
MATERIALS, 2019, 12 (15), 2479
DOI: 10.3390/ma12152479
⟨hal-02392248⟩

13. Modeling dislocation contrasts obtained by accurate-Electron Channeling Contrast Imaging for characterizing deformation mechanisms in bulk materials.
H. Kriaa, A. Guitton, N. Maloufi
MATERIALS, 2019, 12 (10), 1587
DOI: 10.3390/ma12101587
⟨hal-02392249⟩

12. A dislocation-scale characterization of the evolution of deformation microstructures around nanoindentation imprints in a TiAl alloy.
A. Guitton, H. Kriaa, E. Bouzy, J. Guyon, N. Maloufi
MATERIALS, 2018, 11 (2), 305
DOI: 10.3390/ma11020305
⟨hal-02392252⟩

11. Fundamental and experimental aspects of diffraction for characterizing dislocations by electron channeling contrast imaging.
H. Kriaa, A. Guitton, N. Maloufi
SCIENTIFIC REPORTS, 2017 (9742)
DOI: 10.1038/s41598-017-09756-3
⟨hal-02392256⟩

10. Multi-scale approach for analyzing sub-boundaries induced during dislocational creep of uranium dioxide.
M. Ben Saada, N. Gey, A. Guitton, B. Beausir, X. Iltis, N. Maloufi
SF2M PROCEEDINGS, 2017
⟨hal-03039964⟩

9. Electron channeling contrast imaging: influence of diffraction conditions on the dislocation contrast.
H. Kriaa, A. Guitton, N. Maloufi
SF2M PROCEEDINGS, 2017
⟨hal-03039936⟩

8. On-axis TKD for orientation mapping of nano crystalline materials in SEM.
E. Brodu, E. Bouzy, J.J. Fundenberger, J. Guyon, A. Guitton, Y. Zhang
MATERIALS CHARACTERIZATION, 2017, 130, 92–96
DOI: 10.1016/j.matchar.2017.05.036
⟨hal-02392258⟩

7. A miniaturized biaxial deformation rig for in-situ mechanical testing.
S. Van Petegem, A. Guitton, M. Dupraz, A. Bollhalder, K. Sofinowski, M.V. Upadhyay, H. Van Swygenhoven
EXPERIMENTAL MECHANICS, 2017, 57 (4), 569–580
DOI: 10.1007/s11340-016-0244-0
⟨hal-02392260⟩

6. Dislocation modelling in Ti_2AlN MAX phase based on the Pierls-Nabarro model.
K. Gourriet, P. Carrez, P. Cordier, A. Guitton, A. Joulain, L. Thilly, C. Tromas
PHILOSOPHICAL MAGAZINE, 2015, 95 (23), 2539–2552
DOI: 10.1080/14786435.2015.1066938
⟨hal-01515323⟩

5. Picosecond pulsed laser ablation for microscale sample preparation.
A. Guitton, A. Irastorza-Landa, R. Broenimann, D. Grolimund, S. Van Petegem, H. Van Swygenhoven
MATERIALS LETTER, 2015, 160 (1), 589–591
DOI: 10.1016/j.matlet.2015.06.119
⟨hal-01514740⟩

4. Evidence of dislocation cross-slip in MAX phase deformed at high temperature.
A. Guitton, A. Joulain, L. Thilly, C. Tromas
SCIENTIFIC REPORTS, 2014, 4 (6358)
DOI: 10.1038/srep06358
⟨hal-01503720⟩

3. Effect of microstructure anisotropy on the deformation of MAX polycrystals studied by in-situ compression combined with neutron diffraction.
A. Guitto n, S. Van Petegem, C. Tromas, A. Joulain, H. Van Swygenhoven, L. Thilly
APPLIED PHYSICS LETTERS, 2014, 24 (241910)
DOI: 10.1063/1.4884601
⟨hal-01503721⟩

2. Pressure-enforced plasticity in MAX phases: from single grain to polycrystal investigation.
G.P. Bei, A. Guitton, A. Joulain, V. Brunet, S. Dubois, L. Thilly, C. Tromas
PHILOSOPHICAL MAGAZINE, 2013, 93 (15), 1784–1801
DOI: 10.1080/14786435.2012.755272
⟨hal-01501851⟩

1. Dislocation analysis of Ti_2AlN deformed at room temperature under confining pressure.
A. Guitton, A. Joulain, L. Thilly, C. Tromas
PHILOSOPHICAL MAGAZINE, 2012, 92 (36), 4536–4546
DOI: 10.1080/14786435.2012.715250
⟨hal-03041046⟩

Latest invited lectures

Updated list on my webpage: www.antoine-guitton.fr.

- Polycrystal plasticity revealed by Electron Channeling Contrast Imaging.
GPM – Rouen (France), July 2021

- Contribution of the Electron Channeling Contrast Imaging in polycrystalline plasticity.
ONERA – LEM – Châtillon (France), May 2021

- Statistical confrontation between in-situ Electron Channeling Contrast Imaging and mesoscale polycrystal plasticity models.
  4th Schöntal Symposium (*invited talk*) – Schöntal (Germany), March 2020

- Electron Channeling Contrast Imaging: a promising technique for materials science.
  UMET, TimeMan ERC-Project – Lille (France), November 2019

- Electron Channeling Contrast Imaging: theory, experiments and applications to materials science.
  École Polytechnique – Palaiseau (France), November 2019

- How to characterize comprehensively dislocations in a bulk specimen?
  Institut Pprime – Poitiers (France), October 2019

- Electron microscopies: a powerful tool for understanding the fundamental deformation mechanisms of materials.
  Beijing Jiaotong University – Beijing (China), September 2019

- Recent progress on Scanning Electron Microscopy for understanding fundamental deformation mechanisms of materials.
  16th SFμ conference (*invited talk*) – Poitiers (France), July 2019

- Accurate Electron Channeling Contrast Imaging (A-ECCI): a powerful tool for understanding the fundamental deformation mechanisms of materials.
  Max Planck Institut für Eisenforshung GMBH – Düsseldorf (Germany), March 2019

- Accurate Electron Channeling Contrast Imaging (A-ECCI): a powerful tool for understanding the fundamental deformation mechanisms of materials.
  Ruhr-Universität – Bochum (Germany), March 2019

Latest oral contributions to peer reviewed conferences

Full list on my webpage. Speaker is written in italics.

- Plasticity induced by nanoindentation in a CrCoNi medium-entropy alloy studied by accurate electron channeling contrast imaging revealing dislocation-low angle grain boundary interactions
  F. Habiyaremye, A. Guitton F. Schäfer, F. Scholz, M. Schneider, J. Frenzel, G. Laplanche, N. Maloufi
  Plasticité 2020 – Toulouse, Virtual (FR), 2021

- Interactions between dislocations and low-angle grain boundary in a single CrCoNi medium-entropy alloy
  F. Habiyaremye, A. Guitton F. Schäfer, F. Scholz, M. Schneider, J. Frenzel,

G. Laplanche, N. Maloufi
TMS2021 Annual Meeting & Exhibition – Orlando,Virtual (USA), 2021

- Microstructural anisotropy and its influence on the internal stress field within grains: experimental confrontation with full-field crystal plasticity models.
K. Venkatraman, M. Ben Haj Slama, V. Taupin, N. Maloufi, S. Berbenni, A. D. Rollett, M. Diehl, A. Guitton
TMS2021 Annual Meeting & Exhibition (*Keynote*) – Orlando, Virtual (USA), 2021

- Frank partial dislocation in Ti_2AlC-MAX phase induced by matrix-Cu diffusion.
W. Yu, J. Guénolé, J. Ghanbaja, M. Vallet, *A. Guitton*
45th International Conference and Expo on Advanced Ceramics and Composites (ICACC) – Daytona, Virtual (USA),2021

- Mechanisms of plastic deformation in the vicinity of a low-angle grain boundary in a CrCoNi medium-entropy alloy.
F. Habiyaremye, A. Guitton, F. Schäfer, F. Scholz, M. Schneider, J. Frenzel, G. Laplanche, N. Maloufi
MRS Fall Meeting & Exhibit – Boston, Virtual (USA),2020

- Effect of free surfaces on dislocation configurations – experiment and modeling.
H. Kriaa, V. Taupin, A. Guitton, L. Capolungo, N. Maloufi
MRS Fall Meeting & Exhibit – Boston, Virtual (USA),2020

- Confrontation between in-situ SEM observations and mesoscale polycrystalline plasticity models.
K. Venkatraman, M. Ben Haj Slama, V. Taupin, N. Maloufi, A. D. Rollett, S. Berbenni, A. Guitton
MRS Fall Meeting & Exhibit – Boston, Virtual (USA),2020

- Mechanisms of plastic deformation in the vicinity of a low-angle grain boundary in CrCoNi medium-entropy alloy
F. Habiyaremye, A. Guitton F. Schäfer, F. Scholz, M. Schneider, J. Frenzel, G. Laplanche, N. Maloufi
GDR-HEA – virtual, 2020

- In-situ SEM dislocation-scale characterization and simulation for BCC deformation during macroscopic tensile testing: new insight on pencil glide in β-Ti21S.
M. Ben Haj Slama, N. Maloufi, V. Taupin, A. D. Rollett, A. Guitton
1st colloquium on theoretical and experimental micro-mechanics – Metz (France), 2019

Latest poster contributions to peer reviewed conferences

Full list on my webpage. Speaker is written in italics.

- Experimental study of elementary deformation mechanisms around a low-angle grain boundary in a single crystalline CrCoNi medium-entropy alloy.
  F. Habiyaremye, *A. Guitton*, F. Schäfer, G. Laplanche, N. Maloufi
  4th Schöntal Symposium – Schöntal (Germany), 2020

- Characterization of dislocation evolution in bulk Ti21S specimen coupled with in-situ macroscopic tensile testing in SEM.
  M. Ben Haj Slama, N. Maloufi, J. Guyon, L. Weiss, A. Guitton
  EBSD 2019 Meeting – Teddington (UK), 2019

- Characterization of crystalline defects studied by STEM-in-SEM.
  C. Zhang, J.C. Menard, J. Guyon, J.J. Fundenberger, Y. Zhang, E. Bouzy, C. Hébert, *A. Guitton*
  MRS Fall Meeting & Exhibit – Boston (USA), 2018

- How to in-situ follow the evolution of dislocation configurations during mechanical testing on bulk specimen.
  M. Ben Haj Slama, H. Kriaa, J. Guyon, N. Maloufi, J.J. Fundenberger, *A. Guitton*
  MRS Fall Meeting & Exhibit – Boston (USA), 2018

- Fundamental and experimental aspects of diffraction for characterizing dislocations on bulk materials by electron channeling contrast imaging in scanning electron microscope.
  H. Kriaa, *A. Guitton*, N. Maloufi
  MRS Fall Meeting & Exhibit – Boston (USA), 2018

Miscellaneous

- Member of the scientific committee of the IRMA federation included in the network METSA (*Microscopie Électronique en Transmission et Sonde Atomique*: Transmission Electron Microscopy and Atom probe)

- Responsible with Dr. Vincent Taupin of the research group Micro- and nanomechanics, Auto-organization, PLasticity, Interfaces (MAPLI) from LEM3 (2021, effective in 2024)

- Reviewer for the Czech Science Foundation (2021)

- Member of the communication council of LEM3 (from 2021)

- Outstanding reviewer at Acta Materialia, Inc. (2020)

- ERC remote referee (2020)
- Selected within the Université de Lorraine (only 8 persons) to follow the working group of excellence “CODEV: develop the leadership of researchers” (2019-2020)
- ANR referee (2019)
- Special issue editor in Materials journal “New progress on electron microscopies for characterizing microstructures” (2019)
- Co-responsible of the bachelor in metallurgy (work/study program) with Prof. N. Allain (from 2017)
- Member of the board of the GUMP (French-speaking association of users of Philips-FEI-ThermoFisher electron microscopes) and member of the organization committee of symposia (from 2015)

Bibliography

[1] A. Conan Doyle. A scandal in Bohemia. In *The adventures of Sherlock Holmes*. Newnes, George, 1891.
(Cited on page -1).

[2] G.E.P. Box. Robustness in the Strategy of Scientific Model Building. In *Robustness in Statistics*, pages 201–236. Elsevier, 1979.
(Cited on page -1).

[3] A. H. Cottrell and D. L. Dexter. Dislocations and Plastic Flow in Crystals. *American Journal of Physics*, 22(4):242–243, apr 1954, doi:10.1119/1.1933704.
(Cited on pages 1 and 94).

[4] J.P. Hirth and J. Lothe. *Theory of Dislocations*. Krieger Publishing Company, 1992.
(Cited on pages 1, 7, 8, 9, 46, 47, 49, 59 and 95).

[5] E. Schmid and W. Boas. *Kristallplastizität*. Springer Berlin Heidelberg, Berlin, Heidelberg, 1935.
(Cited on page 5).

[6] V. Volterra. Sur l'équilibre des corps élastiques multiplement connexes. *Annales scientifiques de l'École normale supérieure*, 24:401–517, 1907, doi:10.24033/asens.583.
(Cited on page 7).

[7] J.M. Burgers. Physics. — Some considerations on the fields of stress connected with dislocations in a regular crystal lattice. I. In *Selected Papers of J. M. Burgers*, pages 335–389. Springer Netherlands, Dordrecht, 1995.
(Cited on page 7).

[8] D. Hull and D.J. Bacon. *Introduction to Dislocations*. Elsevier, 2011.
(Cited on pages 8 and 9).

[9] L. Priester. *Les joints de grains - De la théorie à l'ingénierie*. EDP Sciences, 2006.
(Cited on pages 8, 8, 8, 8, 8, 8, 10, 10 and 95).

[10] M. Schreiber, K.D. Molodov, T. Al-Samman, S. Korte-Kerzel, and D.A. Molodov. Impact of grain boundaries on microstructure evolution during deformation of a magnesium tricrystal. *Materials Science and Engineering: A*, 742:295–304, jan 2019, doi:10.1016/j.msea.2018.11.002.
(Cited on page 8).

[11] N. Hansen. Hall–Petch relation and boundary strengthening. *Scripta Materialia*, 51(8):801–806, oct 2004, doi:10.1016/j.scriptamat.2004.06.002.
(Cited on pages 8 and 62).

[12] R. Von Mises. Mechanik der festen körper im plastisch- deformablen zustand. *Nachrichten von der Gesellschaft der Wissenschaften zu Göttingen, Mathematisch-Physikalische Klasse*, 1913:582–592, 1913.
(Cited on page 8).

[13] J. Kacher, B.P. Eftink, B. Cui, and I.M. Robertson. Dislocation interactions with grain boundaries. *Current Opinion in Solid State and Materials Science*, 18(4):227–243, aug 2014, doi:10.1016/j.cossms.2014.05.004.
(Cited on page 8).

[14] M. Heller, J.S.K.L. Gibson, R. Pei, and S. Korte-Kerzel. Deformation of µm- and mm-sized Fe2.4wtwith a high angle grain boundary at room temperature. *Acta Materialia*, 194:452–463, aug 2020, doi:10.1016/j.actamat.2020.04.011.
(Cited on page 8).

[15] V. Novikov. *Concise Dictionary of Materials Science*. CRC Press, sep 2002.
(Cited on page 9).

[16] J. Guénolé, V. Taupin, M. Vallet, W. Yu, and A. Guitton. Features of a nano-twist phase in the nanolayered Ti <math altimg="si1.svg"> <msub> <mrow/> <mn>3</mn> </msub> </math> AlC <math altimg="si2.svg"> <msub> <mrow/> <mn>2</mn> </msub> </math> MAX phase. *Scripta Materialia*, 210:114425, mar 2022, doi:10.1016/j.scriptamat.2021.114425.
(Cited on page 10).

[17] E.O. Hall. The Deformation and Ageing of Mild Steel: III Discussion of Results. *Proceedings of the Physical Society. Section B*, 64(9):747–753, sep 1951, doi:10.1088/0370-1301/64/9/303.
(Cited on page 10).

[18] R. Z. Valiev, I. V. Alexandrov, Y. T. Zhu, and T. C. Lowe. Paradox of Strength and Ductility in Metals Processed Bysevere Plastic Deformation. *Journal of Materials Research*, 17(1):5–8, jan 2002, doi:10.1557/JMR.2002.0002.
(Cited on page 10).

[19] Y.T. Zhu, T.C. Lowe, and T.G. Langdon. Performance and applications of nanostructured materials produced by severe plastic deformation. *Scripta Materialia*, 51(8):825–830, oct 2004, doi:10.1016/j.scriptamat.2004.05.006.

[20] N.M. Cordero, S. Forest, E.P. Busso, S. Berbenni, and M. Cherkaoui. Grain size effects on plastic strain and dislocation density tensor fields in metal polycrystals. *Computational Materials Science*, 52(1):7–13, feb 2012, doi:10.1016/j.commatsci.2011.02.043.
(Cited on page 10).

[21] E. Bayerschen, A. T. McBride, B. D. Reddy, and T. Böhlke. Review on slip transmission criteria in experiments and crystal plasticity models. *Journal of Materials Science*, 51(5):2243–2258, mar 2016, doi:10.1007/s10853-015-9553-4.
(Cited on pages 11, 12 and 12).

[22] J.D Livingston and B Chalmers. Multiple slip in bicrystal deformation. *Acta Metallurgica*, 5(6):322–327, jun 1957, doi:10.1016/0001-6160(57)90044-5.
(Cited on page 12).

[23] T.C. Lee, I.M. Robertson, and H.K. Birnbaum. Prediction of slip transfer mechanisms across grain boundaries. *Scripta Metallurgica*, 23(5):799–803, may 1989, doi:10.1016/0036-9748(89)90534-6.

[24] J. Luster and M. A. Morris. Compatibility of deformation in two-phase Ti-Al alloys: Dependence on microstructure and orientation relationships. *Metallurgical and Materials Transactions A*, 26(7):1745–1756, jul 1995, doi:10.1007/BF02670762.

[25] E. Werner and W. Prantl. Slip transfer across grain and phase boundaries. *Acta Metallurgica et Materialia*, 38(3):533–537, mar 1990, doi:10.1016/0956-7151(90)90159-E.

[26] I. J. Beyerlein, N. A. Mara, J. Wang, J. S. Carpenter, S. J. Zheng, W. Z. Han, R. F. Zhang, K. Kang, T. Nizolek, and T. M. Pollock. Structure–Property–Functionality of Bimetal Interfaces. *JOM*, 64(10):1192–1207, oct 2012, doi:10.1007/s11837-012-0431-0.
(Cited on page 12).

[27] T.R. Bieler, P. Eisenlohr, C. Zhang, H.J. Phukan, and M.A. Crimp. Grain boundaries and interfaces in slip transfer. *Current Opinion in Solid State and Materials Science*, 18(4):212–226, aug 2014, doi:10.1016/j.cossms.2014.05.003.
(Cited on page 12).

[28] J.F Nye. Some geometrical relations in dislocated crystals. *Acta Metallurgica*, 1(2):153–162, mar 1953, doi:10.1016/0001-6160(53)90054-6.
(Cited on pages 13 and 96).

[29] C. Ernould, B. Beausir, J.-J. Fundenberger, V. Taupin, and E. Bouzy. Global DIC approach guided by a cross-correlation based initial guess for HR-EBSD and on-axis HR-TKD. *Acta Materialia*, 191:131–148, jun 2020, doi:10.1016/j.actamat.2020.03.026.
(Cited on pages 13 and 30).

[30] T. C. Lowe and A. K. Miller. Modeling Internal Stresses in the Nonelastic Deformation of Metals. *Journal of Engineering Materials and Technology*, 108(4):365–373, oct 1986, doi:10.1115/1.3225896.
(Cited on pages 13 and 96).

[31] W. Ludwig, A. King, P. Reischig, M. Herbig, E.M. Lauridsen, S. Schmidt, H. Proudhon, S. Forest, P. Cloetens, S. Rolland du Roscoat, J.Y. Buffière, T.J. Marrow, and H.F. Poulsen. New opportunities for 3D materials science of polycrystalline materials at the micrometre lengthscale by combined use of X-ray diffraction and X-ray imaging. *Materials Science and Engineering: A*, 524(1-2):69–76, oct 2009, doi:10.1016/j.msea.2009.04.009.

[32] T. Dillard, F. N'guyen, E. Maire, L. Salvo, S. Forest, Y. Bienvenu, J.D. Bartout, M. Croset, R. Dendievel, and P. Cloetens. 3D quantitative image analysis of open-cell nickel foams under tension and compression loading using X-ray microtomography. *Philosophical Magazine*, 85(19):2147–2175, jul 2005, doi:10.1080/14786430412331331916.

[33] H. Dierke, F. Krawehl, S. Graff, S. Forest, J. Šachl, and H. Neuhäuser. Portevin–LeChatelier effect in Al–Mg alloys: Influence of obstacles – experiments and modelling. *Computational Materials Science*, 39(1):106–112, mar 2007, doi:10.1016/j.commatsci.2006.03.019.

[34] R.A. Lebensohn, R. Brenner, O. Castelnau, and A.D. Rollett. Orientation image-based micromechanical modelling of subgrain texture evolution in polycrystalline copper. *Acta Materialia*, 56(15):3914–3926, sep 2008, doi:10.1016/j.actamat.2008.04.016.

[35] R. Pokharel, J. Lind, A.K. Kanjarla, R.A. Lebensohn, S.F. Li, P. Kenesei, R.M. Suter, and A.D. Rollett. Polycrystal Plasticity: Comparison Between Grain - Scale Observations of Deformation and Simulations. *Annual Review of Condensed Matter Physics*, 5(1):317–346, mar 2014, doi:10.1146/annurev-conmatphys-031113-133846.

[36] A.D. Rollett, F. Wagner, N. Allain-Bonasso, D.P. Field, and R.A. Lebensohn. Comparison of Gradients in Orientation and Stress between Experiment and Simulation. *Materials Science Forum*, 702-703:463–468, dec 2011, doi:10.4028/www.scientific.net/MSF.702-703.463.
(Cited on pages 13 and 96).

[37] N. Bertin, R.B. Sills, and W. Cai. Frontiers in the Simulation of Dislocations. *Annual Review of Materials Research*, 50(1):437–464, jul 2020, doi:10.1146/annurev-matsci-091819-015500.

(Cited on pages 13 and 97).

[38] L.T. Hansen, D.T. Fullwood, E.R. Homer, R.H. Wagoner, H. Lim, J.D. Carroll, G. Zhou, and H.J. Bong. An investigation of geometrically necessary dislocations and back stress in large grained tantalum via EBSD and CPFEM. *Materials Science and Engineering: A*, 772:138704, jan 2020, doi:10.1016/j.msea.2019.138704.
(Cited on pages 13 and 97).

[39] H. Zhang, A. Jérusalem, E. Salvati, C. Papadaki, KS.S. Fong, X. Song, and A.M. Korsunsky. Datasets for multi-scale diffraction analysis (synchrotron XRD and EBSD) of twinning-detwinning during tensile-compressive deformation of AZ31B magnesium alloy samples. *Data in Brief*, 26:104423, oct 2019, doi:10.1016/j.dib.2019.104423.

[40] H. Pi, J. Han, C. Zhang, A. K. Tieu, and Z. Jiang. Modeling uniaxial tensile deformation of polycrystalline Al using CPFEM. *Journal of University of Science and Technology Beijing, Mineral, Metallurgy, Material*, 15(1):43–47, feb 2008, doi:10.1016/S1005-8850(08)60009-2.

[41] F. Di Gioacchino and J. Quinta da Fonseca. An experimental study of the polycrystalline plasticity of austenitic stainless steel. *International Journal of Plasticity*, 74:92–109, nov 2015, doi:10.1016/j.ijplas.2015.05.012.
(Cited on pages 13 and 97).

[42] M.W. Barsoum and T. El-Raghy. Synthesis and Characterization of a Remarkable Ceramic: Ti3SiC2. *Journal of the American Ceramic Society*, 79(7):1953–1956, jul 1996, doi:10.1111/j.1151-2916.1996.tb08018.x.
(Cited on pages 15 and 89).

[43] M.W. Barsoum. The MN+1AXN phases: A new class of solids. *Progress in Solid State Chemistry*, 28(1-4):201–281, jan 2000, doi:10.1016/S0079-6786(00)00006-6.
(Cited on pages 15 and 17).

[44] M.W. Barsoum and T. El-Raghy. The MAX Phases: Unique New Carbide and Nitride Materials. *American Scientist*, 89(4):334, 2001, doi:10.1511/2001.4.334.
(Cited on pages 15, 16 and 17).

[45] M.W. Barsoum and M. Radovic. Elastic and Mechanical Properties of the MAX Phases. *Annual Review of Materials Research*, 41(1):195–227, aug 2011, doi:10.1146/annurev-matsci-062910-100448.
(Cited on page 15).

[46] Z.J. Lin, M.J. Zhuo, M.S. Li, J.Y. Wang, and Y.C. Zhou. Synthesis and microstructure of layered-ternary Ti2AlN ceramic. *Scripta Materialia*, 56(12):1115–1118, jun 2007, doi:10.1016/j.scriptamat.2007.01.049.
(Cited on page 16).

[47] M. Yan, Y.L. Chen, B.H. Mei, and J.Q. Zhu. Synthesis of high-purity Ti2AlN ceramic by hot pressing. *Transactions of Nonferrous Metals Society of China*, 18(1):82–85, feb 2008, doi:10.1016/S1003-6326(08)60015-1.
(Cited on page 17).

[48] X. Pi, W. Yu, C. Ma, X. Wang, S. Xiong, and A. Guitton. Processing and Mechanical Properties of Ti2AlC MAX Phase Reinforced AE44 Magnesium Composite. *Materials*, 13(4):995, feb 2020, doi:10.3390/ma13040995.
(Cited on page 17).

[49] W. Yu, J. Guénolé, J. Ghanbaja, M. Vallet, and A. Guitton. Frank partial dislocation in Ti2AlC-MAX phase induced by matrix-Cu diffusion. *Scripta Materialia*, 191:34–39, jan 2021, doi:10.1016/j.scriptamat.2020.09.007.
(Cited on pages 21, 28 and 97).

[50] W. Yu, X. Pi, W. Chen, M. Vallet, A. Guitton, and L. Zhang. Effects of A-site atoms in Ti_2AlC and Ti_3SiC_2 MAX phases reinforced Mg composites: interfacial structure and mechanical properties. *Materials Science and Engineering: A*, page 141961, 2021, doi:https://doi.org/10.1016/j.msea.2021.141961.
(Cited on page 17).

[51] A. Guitton, S. Van Petegem, C. Tromas, A. Joulain, H. Van Swygenhoven, and L. Thilly. Effect of microstructure anisotropy on the deformation of MAX polycrystals studied by in-situ compression combined with neutron diffraction. *Applied Physics Letters*, 104(24):241910, jun 2014, doi:10.1063/1.4884601.
(Cited on pages 17, 18, 18, 19, 19, 20, 90 and 98).

[52] Z.F. Zhang and Z.M. Sun. Shear fracture behavior of Ti3SiC2 induced by compression at temperatures below 1000°C. *Materials Science and Engineering: A*, 408(1-2):64–71, nov 2005, doi:10.1016/j.msea.2005.07.041.
(Cited on page 17).

[53] M.W. Barsoum, T Zhen, S.R. Kalidindi, M Radovic, and A Murugaiah. Fully reversible, dislocation-based compressive deformation of Ti3SiC2 to 1 GPa. *Nature Materials*, 2(2):107–111, feb 2003, doi:10.1038/nmat814.
(Cited on pages 17, 18, 19 and 19).

[54] M. W. Barsoum, A. Murugaiah, S. R. Kalidindi, and T. Zhen. Kinking Nonlinear Elastic Solids, Nanoindentations, and Geology. *Physical Review Letters*, 92(25):255508, jun 2004, doi:10.1103/PhysRevLett.92.255508.
(Cited on pages 17, 18, 19 and 19).

[55] S. Forest. Modeling slip, kink and shear banding in classical and generalized single crystal plasticity. *Acta Materialia*, 46(9):3265–3281, may 1998, doi:10.1016/S1359-6454(98)00012-3.
(Cited on page 18).

[56] A. Marano, L. Gélébart, and S. Forest. Intragranular localization induced by softening crystal plasticity: Analysis of slip and kink bands localization modes from high resolution FFT-simulations results. *Acta Materialia*, 175:262–275, aug 2019, doi:10.1016/j.actamat.2019.06.010.
(Cited on page 18).

[57] M. W. Barsoum, L. Farber, and T. El-Raghy. Dislocations, kink bands, and room-temperature plasticity of Ti3SiC2. *Metallurgical and Materials Transactions A*, 30(7):1727–1738, jul 1999, doi:10.1007/s11661-999-0172-z.
(Cited on pages 18 and 19).

[58] M. W. Barsoum, X. Zhao, S. Shanazarov, A. Romanchuk, S. Koumlis, S. J. Pagano, L. Lamberson, and G. J. Tucker. Ripplocations: A universal deformation mechanism in layered solids. *Physical Review Materials*, 3(1):013602, jan 2019, doi:10.1103/PhysRevMaterials.3.013602.
(Cited on page 18).

[59] G. Plummer, H. Rathod, A. Srivastava, M. Radovic, T. Ouisse, M. Yildizhan, P.O.Å. Persson, K. Lambrinou, M.W. Barsoum, and G.J. Tucker. On the origin of kinking in layered crystalline solids. *Materials Today*, jan 2021, doi:10.1016/j.mattod.2020.11.014.
(Cited on page 18).

[60] G.-P. Bei, A. Guitton, A. Joulain, V. Brunet, S. Dubois, L. Thilly, and C. Tromas. Pressure-enforced plasticity in MAX phases: from single grain to polycrystal investigation. *Philosophical Magazine*, 93(15):1784–1801, may 2013, doi:10.1080/14786435.2012.755272.
(Cited on pages 18, 19, 59, 90 and 97).

[61] J. Bauschinger. Changes of the elastic limit and the modulus of elasticity on various metals. *Zivilingenieur*, 27:289, 1881.
(Cited on page 19).

[62] A. Guitton, A. Joulain, L. Thilly, and C. Tromas. Dislocation analysis of Ti 2 AlN deformed at room temperature under confining pressure. *Philosophical Magazine*, 92(36):4536–4546, dec 2012, doi:10.1080/14786435.2012.715250.
(Cited on pages 19, 19, 19, 20, 21, 49, 90, 90 and 97).

[63] A. Joulain, L. Thilly, and J. Rabier. Revisiting the defect structure of MAX phases: the case of Ti_4AlN_3. *Philos. Mag.*, 88(9):1307–1320, 2008.
(Cited on page 19).

[64] C. Tromas, P. Villechaise, V. Gauthier-Brunet, and S. Dubois. Slip line analysis around nanoindentation imprints in Ti 3 SnC 2 : a new insight into plasticity of MAX-phase materials. *Philosophical Magazine*, 91(7-9):1265–1275, mar 2011, doi:10.1080/14786435.2010.494584.
(Cited on page 19).

[65] K. Gouriet, P. Carrez, P. Cordier, A. Guitton, A. Joulain, L. Thilly, and C. Tromas. Dislocation modelling in Ti 2 AlN MAX phase based on the Peierls–Nabarro model. *Philosophical Magazine*, 95(23):2539–2552, aug 2015, doi:10.1080/14786435.2015.1066938.
(Cited on pages 20, 28, 90 and 97).

[66] Z. Zhan, M. Radovic, and A. Srivastava. On the non-classical crystallographic slip in Tin+1AlCn MAX phases. *Scripta Materialia*, 194:113698, mar 2021, doi:10.1016/j.scriptamat.2020.113698.
(Cited on page 20).

[67] A. Guitton, A. Joulain, L. Thilly, and C. Tromas. Evidence of dislocation cross-slip in MAX phase deformed at high temperature. *Scientific Reports*, 4(1):6358, may 2015, doi:10.1038/srep06358.
(Cited on pages 20, 21, 21, 90, 90 and 97).

[68] H. Van Swygenhoven and S. Van Petegem. In-situ mechanical testing during X-ray diffraction. *Materials Characterization*, 78:47–59, apr 2013, doi:10.1016/j.matchar.2012.12.010.
(Cited on page 23).

[69] C. C. Tasan, J. P. M. Hoefnagels, E. C. A. Dekkers, and M. G. D. Geers. Multi-Axial Deformation Setup for Microscopic Testing of Sheet Metal to Fracture. *Experimental Mechanics*, 52(7):669–678, sep 2012, doi:10.1007/s11340-011-9532-x.
(Cited on page 23).

[70] G. Geandier, D. Thiaudière, R. N. Randriamazaoro, R. Chiron, S. Djaziri, B. Lamongie, Y. Diot, E. Le Bourhis, P. O. Renault, P. Goudeau, A. Bouaffad, O. Castelnau, D. Faurie, and F. Hild. Development of a synchrotron biaxial tensile device for in situ characterization of thin films mechanical response. *Review of Scientific Instruments*, 81(10):103903, oct 2010, doi:10.1063/1.3488628.
(Cited on page 23).

[71] D.M. Collins, M. Mostafavi, R.I. Todd, T. Connolley, and A.J. Wilkinson. A synchrotron X-ray diffraction study of in situ biaxial deformation. *Acta Materialia*, 90:46–58, may 2015, doi:10.1016/j.actamat.2015.02.009.
(Cited on page 23).

[72] A. Guitton, A. Irastorza-Landa, R. Broennimann, D. Grolimund, S. Van Petegem, and H. Van Swygenhoven. Picosecond pulsed laser for microscale sample preparation. *Materials Letters*, 160:589–591, dec 2015, doi:10.1016/j.matlet.2015.06.119.
(Cited on pages 24, 51, 91 and 98).

[73] S. Van Petegem, A. Guitton, M. Dupraz, A. Bollhalder, K. Sofinowski, M.V. Upadhyay, and H. Van Swygenhoven. A miniaturized biaxial deformation rig

for in-situ mechanical testing. *Experimental Mechanics*, 57(4):569–580, apr 2017, doi:10.1007/s11340-016-0244-0.
(Cited on pages 24, 25 and 91).

[74] L. Reimer. *Scanning Electron Microscopy*. Springer Berlin Heidelberg, Berlin, Heidelberg, 1998.
(Cited on pages 27, 29, 31, 37, 37, 38, 38, 38, 39 and 39).

[75] D.B. Williams and C.B. Carter. *Transmission Electron Microscopy*. Springer US, Boston, MA, 2009.
(Cited on pages 27, 27, 28, 28, 37 and 97).

[76] J. Ayache, L. Beaunier, J. Boumendil, G. Ehret, and D. Laub. *Sample Preparation Handbook for Transmission Electron Microscopy*. Springer New York, New York, NY, 2010.
(Cited on pages 27, 51 and 97).

[77] M. Legros. In situ mechanical TEM: Seeing and measuring under stress with electrons. *Comptes Rendus Physique*, 15(2-3):224–240, feb 2014, doi:10.1016/j.crhy.2014.02.002.
(Cited on pages 28, 28 and 97).

[78] M. Legros, G. Dehm, R.M. Keller-Flaig, E. Arzt, K.J. Hemker, and S. Suresh. Dynamic observation of Al thin films plastically strained in a TEM. *Materials Science and Engineering: A*, 309-310:463–467, jul 2001, doi:10.1016/S0921-5093(00)01702-0.

[79] F. Mompiou, D. Caillard, M. Legros, and H. Mughrabi. In situ TEM observations of reverse dislocation motion upon unloading in tensile-deformed UFG aluminium. *Acta Materialia*, 60(8):3402–3414, may 2012, doi:10.1016/j.actamat.2012.02.049.
(Cited on page 28).

[80] F. Mompiou, M. Legros, A. Boé, M. Coulombier, J.-P. Raskin, and T. Pardoen. Inter- and intragranular plasticity mechanisms in ultrafine-grained Al thin films: An in situ TEM study. *Acta Materialia*, 61(1):205–216, jan 2013, doi:10.1016/j.actamat.2012.09.051.
(Cited on pages 28 and 97).

[81] Q. Yu, M. Legros, and A.M. Minor. In situ TEM nanomechanics. *MRS Bulletin*, 40(1):62–70, jan 2015, doi:10.1557/mrs.2014.306.
(Cited on pages 28 and 98).

[82] A.D. Rollett, S.B. Lee, R. Campman, and G.S. Rohrer. Three-Dimensional Characterization of Microstructure by Electron Back-Scatter Diffraction. *Annual Review of Materials Research*, 37(1):627–658, aug 2007, doi:10.1146/annurev.matsci.37.052506.084401.
(Cited on page 29).

[83] N. Allain-Bonasso, F. Wagner, S. Berbenni, and D.P. Field. A study of the heterogeneity of plastic deformation in IF steel by EBSD. *Materials Science and Engineering: A*, 548:56–63, jun 2012, doi:10.1016/j.msea.2012.03.068.
(Cited on page 98).

[84] D. Barbier, N. Gey, N. Bozzolo, S. Allain, and M. Humbert. EBSD for analysing the twinning microstructure in fine-grained TWIP steels and its influence on work hardening. *Journal of Microscopy*, 235(1):67–78, jul 2009, doi:10.1111/j.1365-2818.2009.03182.x.

[85] S. Kalácska, J. Ast, P.D. Ispánovity, J. Michler, and X. Maeder. 3D HR-EBSD Characterization of the plastic zone around crack tips in tungsten single crystals at the micron scale. *Acta Materialia*, 200:211–222, nov 2020, doi:10.1016/j.actamat.2020.09.009.
(Cited on pages 29 and 98).

[86] S. Nishikawa and S. Kikichi. Diffraction of Cathode Rays by Mica. *Nature*, 121(3061):1019–1020, jun 1928, doi:10.1038/1211019a0.
(Cited on page 29).

[87] F. J. Humphreys. Grain and subgrain characterisation by electron backscatter diffraction. *Journal of Materials Science*, 36(16):3833–3854, 2001, doi:10.1023/A:1017973432592.
(Cited on pages 30 and 33).

[88] S. Kalácska, I. Groma, A. Borbély, and P. D. Ispánovity. Comparison of the dislocation density obtained by HR-EBSD and X-ray profile analysis. *Applied Physics Letters*, 110(9):091912, feb 2017, doi:10.1063/1.4977569.
(Cited on pages 30 and 98).

[89] C. Ernould, B. Beausir, J.J. Fundenberger, V. Taupin, and E. Bouzy. Integrated correction of optical distortions for global HR-EBSD techniques. *Ultramicroscopy*, 221:113158, feb 2021, doi:10.1016/j.ultramic.2020.113158.
(Cited on page 30).

[90] D. G. Coates. Kikuchi-like reflection patterns obtained with the scanning electron microscope. *The Philosophical Magazine: A Journal of Theoretical Experimental and Applied Physics*, 16(144):1179–1184, dec 1967, doi:10.1080/14786436708229968.
(Cited on pages 32, 32 and 98).

[91] G. R. Booker, A. M. B. Shaw, M. J. Whelan, and P. B. Hirsch. Some comments on the interpretation of the 'kikuchi-like reflection patterns' observed by scanning electron microscopy. *The Philosophical Magazine: A Journal of Theoretical Experimental and Applied Physics*, 16(144):1185–1191, dec 1967, doi:10.1080/14786436708229969.
(Cited on pages 32, 37 and 98).

[92] Y.N. Picard, R. Kamaladasa, M. De Graef, N. T. Nuhfer, W. J. Mershon, T. Owens, L. Sedlacek, and F. Lopour. Future Prospects for Defect and Strain Analysis in the SEM via Electron Channeling. *Microscopy Today*, 20(2):12–16, mar 2012, doi:10.1017/S1551929512000077.
(Cited on page 32).

[93] G. Naresh-Kumar, B. Hourahine, P. R. Edwards, A. P. Day, A. Winkelmann, A. J. Wilkinson, P. J. Parbrook, G. England, and C. Trager-Cowan. Rapid Nondestructive Analysis of Threading Dislocations in Wurtzite Materials Using the Scanning Electron Microscope. *Physical Review Letters*, 108(13):135503, mar 2012, doi:10.1103/PhysRevLett.108.135503.
(Cited on page 32).

[94] I. Gutierrez-Urrutia, S. Zaefferer, and D. Raabe. Electron channeling contrast imaging of twins and dislocations in twinning-induced plasticity steels under controlled diffraction conditions in a scanning electron microscope. *Scripta Materialia*, 61(7):737–740, oct 2009, doi:10.1016/j.scriptamat.2009.06.018.
(Cited on page 33).

[95] J. Guyon, H. Mansour, N. Gey, M.A. Crimp, S. Chalal, and N. Maloufi. Submicron resolution selected area electron channeling patterns. *Ultramicroscopy*, 149:34–44, feb 2015, doi:10.1016/j.ultramic.2014.11.004.
(Cited on pages 33, 34 and 92).

[96] H. Mansour, J. Guyon, M.A. Crimp, N. Gey, B. Beausir, and N. Maloufi. Accurate electron channeling contrast analysis of dislocations in fine grained bulk materials. *Scripta Materialia*, 84-85:11–14, aug 2014, doi:10.1016/j.scriptamat.2014.03.001.
(Cited on pages 33, 34, 35 and 92).

[97] M. Ben Saada, N. Gey, A. Guitton, B. Beausir, X. Iltis, and N. Maloufi. Multiscale approach for analyzing sub-boundaries induced during dislocational creep of uranium dioxide. In *SF2M Proceedings*, 2017.
(Cited on page 34).

[98] G. L'hôte, C. Lafond, P. Steyer, S. Deschanel, T. Douillard, C. Langlois, and S. Cazottes. Rotational-Electron Channeling Contrast Imaging analysis of dislocation structure in fatigued copper single crystal. *Scripta Materialia*, 162:103–107, mar 2019, doi:10.1016/j.scriptamat.2018.10.050.
(Cited on page 34).

[99] L. Reimer and H. Kohl. *Transmission Electron Microscopy*. Springer Series in Optical Sciences. Springer New York, New York, NY, 2008.
(Cited on page 37).

[100] J.P. Spencer, C.J. Humphreys, and P.B. Hirsch. A dynamical theory for the contrast of perfect and imperfect crystals in the scanning electron microscope using backscattered electrons. *Philosophical Magazine*, 26(1):193–213, jul 1972, doi:10.1080/14786437208221029.

(Cited on page 37).

[101] A.J. Wilkinson and P.B. Hirsch. Electron diffraction based techniques in scanning electron microscopy of bulk materials. *Micron*, 28(4):279–308, aug 1997, doi:10.1016/S0968-4328(97)00032-2.
(Cited on page 37).

[102] L. Reimer, U. Heilers, and G. Saliger. Kikuchi band contrast in diffraction patterns recorded by transmitted and backscattered electrons. *Scanning*, 8(3):101–118, 1986, doi:10.1002/sca.4950080303.
(Cited on page 38).

[103] E. Schrödinger. An Undulatory Theory of the Mechanics of Atoms and Molecules. *Physical Review*, 28(6):1049–1070, dec 1926, doi:10.1103/PhysRev.28.1049.
(Cited on page 38).

[104] H. Kriaa, A. Guitton, and N. Maloufi. Fundamental and experimental aspects of diffraction for characterizing dislocations by electron channeling contrast imaging in scanning electron microscope. *Scientific Reports*, 7(1):9742, aug 2017.
(Cited on pages 39, 46, 49, 49, 92 and 99).

[105] H. Kriaa, A. Guitton, and N. Maloufi. Modelling Electron Channeling Contrast Intensity of Stacking Fault and Twin Boundary Using Crystal Thickness Effect. *Materials*, 14(7):1696, mar 2021, doi:10.3390/ma14071696.
(Cited on pages 42, 42, 44, 44 and 45).

[106] H. Kriaa, A. Guitton, and N. Maloufi. Modeling dislocation contrasts obtained by accurate-electron channeling contrast imaging for characterizing deformation mechanisms in bulk materials. *Materials*, 12:1587, 2019.
(Cited on pages 46, 48, 48, 50, 92 and 99).

[107] H. Kriaa, A. Guitton, and N. Maloufi. Electron channeling contrast imaging: influence of diffraction conditions on the dislocation contraste. In *SF2M Proceedings*, 2017.
(Cited on page 49).

[108] S. Kondo, T. Mitsuma, N. Shibata, and Y. Ikuhara. Direct observation of individual dislocation interaction processes with grain boundaries. *Science Advances*, 2(11):e1501926, nov 2016, doi:10.1126/sciadv.1501926.
(Cited on page 51).

[109] J. Kacher and I.M. Robertson. Quasi-four-dimensional analysis of dislocation interactions with grain boundaries in 304 stainless steel. *Acta Materialia*, 60(19):6657–6672, nov 2012, doi:10.1016/j.actamat.2012.08.036.
(Cited on page 51).

[110] A.A. Kohnert, H. Tummala, R.A. Lebensohn, C.N. Tomé, and L. Capolungo. On the use of transmission electron microscopy to quantify dislocation densities in bulk metals. *Scripta Materialia*, 178:161–165, 2020, doi:10.1016/j.scriptamat.2019.11.011.
(Cited on page 51).

[111] R. Maaß, S. Van Petegem, C.N. Borca, and H. Van Swygenhoven. In situ Laue diffraction of metallic micropillars. *Materials Science and Engineering: A*, 524(1-2):40–45, oct 2009, doi:10.1016/j.msea.2009.05.062.
(Cited on pages 51 and 98).

[112] N.V. Malyar, J.-S. Micha, G. Dehm, and C. Kirchlechner. Dislocation-twin boundary interaction in small scale Cu bi-crystals loaded in different crystallographic directions. *Acta Materialia*, 129:91–97, may 2017, doi:10.1016/j.actamat.2017.02.067.
(Cited on pages 51 and 98).

[113] T. Richeton, T. Le, L.T.and Chauve, M. Bernacki, S. Berbenni, and M. Montagnat. Modelling the transport of geometrically necessary dislocations on slip systems: application to single- and multi-crystals of ice. *Modelling and Simulation in Materials Science and Engineering*, 25(2):025010, feb 2017, doi:10.1088/1361-651X/aa5341.
(Cited on page 51).

[114] H. Van Swygenhoven and S. Van Petegem. In-situ mechanical testing during X-ray diffraction. *Materials Characterization*, 78(0):47–59, apr 2013, doi:10.1016/j.matchar.2012.12.010.
(Cited on pages 51 and 98).

[115] D.F. Bahr and D.J. Morris. *Nanoindentation: Localized Probes of Mechanical Behavior of Materials*. Springer US, 2008.
(Cited on pages 53, 53 and 54).

[116] F. Habiyaremye, A. Guitton, X. Chen, T. Richeton, S. Berbenni, and N. Maloufi. Influence of the configurations of dislocations on the pop in load during nanoindentation in a CrCoNi medium entropy alloy. *Submitted*, ??(??):??, ?? 2021, doi:??
(Cited on page 53).

[117] H. Hertz. Ueber die Berührung fester elastischer Körper. *Journal für die reine und angewandte Mathematik (Crelles Journal)*, 1882(92):156–171, jan 1882, doi:10.1515/crll.1882.92.156.
(Cited on page 53).

[118] B.R. Lawn. Indentation of Ceramics with Spheres: A Century after Hertz. *Journal of the American Ceramic Society*, 81(8):1977–1994, jan 2005, doi:10.1111/j.1151-2916.1998.tb02580.x.
(Cited on page 53).

[119] Y.-W. Kim and D.M. Dimiduk. Progress in the understanding of gamma titanium aluminides. *JOM*, 43(8):40–47, aug 1991, doi:10.1007/BF03221103.
(Cited on page 55).

[120] F. Appel and R. Wagner. Microstructure and deformation of two-phase γ-titanium aluminides. *Materials Science and Engineering: R: Reports*, 22(5):187–268, may 1998, doi:10.1016/S0927-796X(97)00018-1.
(Cited on pages 55 and 99).

[121] E.A. Loria. Quo vadis gamma titanium aluminide. *Intermetallics*, 9(12):997–1001, dec 2001, doi:10.1016/S0966-9795(01)00064-4.
(Cited on page 55).

[122] J.C. Schuster and M. Palm. Reassessment of the binary Aluminum-Titanium phase diagram. *Journal of Phase Equilibria and Diffusion*, 27(3):255–277, jun 2006, doi:10.1361/154770306X109809.
(Cited on page 55).

[123] F. Appel, J.D.H. Paul, and M. Oehring. *Gamma Titanium Aluminide Alloys*. Wiley-VCH Verlag GmbH & Co. KGaA, Weinheim, Germany, sep 2011.
(Cited on page 55 and 55).

[124] S. R. Dey, A. Hazotte, and E. Bouzy. Multiscale γ variant selection in a quaternary near- γ Ti–Al alloy. *Philosophical Magazine*, 86(20):3089–3112, jul 2006, doi:10.1080/14786430600669832.
(Cited on page 56).

[125] S.R. Dey, A. Morawiec, E. Bouzy, A. Hazotte, and J.J. Fundenberger. A technique for determination of γ/γ interface relationships in a ($\alpha 2+\gamma$) TiAl base alloy using TEM Kikuchi patterns. *Materials Letters*, 60(5):646–650, mar 2006, doi:10.1016/j.matlet.2005.09.052.
(Cited on page 56).

[126] M.F. Stroosnijder, V.A.C. Haanappel, and H. Clemens. Oxidation behaviour of TiAl-based intermetallics—influence of heat treatment. *Materials Science and Engineering: A*, 239-240:842–846, dec 1997, doi:10.1016/S0921-5093(97)00674-6.
(Cited on page 57).

[127] W.T. Marketz, F.D. Fischer, and H. Clemens. Deformation mechanisms in TiAl intermetallics—experiments and modeling. *International Journal of Plasticity*, 19(3):281–321, mar 2003, doi:10.1016/S0749-6419(01)00036-5.
(Cited on pages 57 and 58).

[128] A. Guitton, H. Kriaa, E. Bouzy, J. Guyon, and N. Maloufi. A Dislocation-Scale Characterization of the Evolution of Deformation Microstructures around Nanoindentation Imprints in a TiAl Alloy. *Materials*, 11(2):305, feb 2018, doi:10.3390/ma11020305.
(Cited on pages 59, 92, 99 and 100).

[129] M. A. Gibson and C. T. Forwood. Slip transfer of deformation twins in duplex y-based Ti-Al alloys: Part III. Transfer across general large-angle γ-γ grain boundaries. *Philosophical Magazine A*, 82(7):1381–1404, may 2002, doi:10.1080/01418610208235678.
(Cited on page 60).

[130] B. Simkin. A factor to predict microcrack nucleation at γ–γ grain boundaries in TiAl. *Scripta Materialia*, 49(2):149–154, jul 2003, doi:10.1016/S1359-6462(03)00216-1.
(Cited on page 60 and 60).

[131] C. Zambaldi and D. Raabe. Plastic anisotropy of γ-TiAl revealed by axisymmetric indentation. *Acta Materialia*, 58(9):3516–3530, may 2010, doi:10.1016/j.actamat.2010.02.025.

[132] T.R. Bieler, A. Fallahi, B.C. Ng, D. Kumar, M.A. Crimp, B.A. Simkin, A. Zamiri, F. Pourboghrat, and D.E. Mason. Fracture initiation/propagation parameters for duplex TiAl grain boundaries based on twinning, slip, crystal orientation, and boundary misorientation. *Intermetallics*, 13(9):979–984, sep 2005, doi:10.1016/j.intermet.2004.12.013.
(Cited on page 60).

[133] M.C. Gao, J.W. Yeh, P.K. Liaw, and Y. Zhang, editors. *High-Entropy Alloys*. Springer International Publishing, Cham, 2016.
(Cited on page 61 and 61).

[134] J.W. Yeh, Y.L. Chen, S.J. Lin, and S.K. Chen. High-Entropy Alloys – A New Era of Exploitation. *Materials Science Forum*, 560:1–9, nov 2007, doi:10.4028/www.scientific.net/MSF.560.1.
(Cited on page 61).

[135] Z. Wu, H. Bei, G.M. Pharr, and E.P. George. Temperature dependence of the mechanical properties of equiatomic solid solution alloys with face-centered cubic crystal structures. *Acta Materialia*, 81:428–441, dec 2014, doi:10.1016/j.actamat.2014.08.026.
(Cited on page 61).

[136] K. Ming, X. Bi, and J. Wang. Strength and ductility of CrFeCoNiMo alloy with hierarchical microstructures. *International Journal of Plasticity*, 113:255–268, feb 2019, doi:10.1016/j.ijplas.2018.10.005.
(Cited on page 61).

[137] B. Gludovatz, A. Hohenwarter, K.V. S. Thurston, H. Bei, Z. Wu, E.P. George, and R.O. Ritchie. Exceptional damage-tolerance of a medium-entropy alloy CrCoNi at cryogenic temperatures. *Nature Communications*, 7(1):10602, apr 2016, doi:10.1038/ncomms10602.
(Cited on pages 61, 62 and 100).

[138] J. R. Strife and D. E. Passoja. The effect of heat treatment on microstructure and cryogenic fracture properties in 5Ni and 9Ni steel. *Metallurgical Transactions A*, 11(8):1341–1350, aug 1980, doi:10.1007/BF02653488.
(Cited on page 61).

[139] S. Praveen and H.S. Kim. High-Entropy Alloys: Potential Candidates for High-Temperature Applications - An Overview. *Advanced Engineering Materials*, 20(1):1700645, jan 2018, doi:10.1002/adem.201700645.
(Cited on page 61).

[140] G. Laplanche, A. Kostka, C. Reinhart, J. Hunfeld, G. Eggeler, and E.P. George. Reasons for the superior mechanical properties of medium-entropy CrCoNi compared to high-entropy CrMnFeCoNi. *Acta Materialia*, 128:292–303, apr 2017, doi:10.1016/j.actamat.2017.02.036.
(Cited on page 62 and 62).

[141] G. Laplanche, M. Schneider, F. Scholz, J. Frenzel, G. Eggeler, and J. Schreuer. Processing of a single-crystalline CrCoNi medium-entropy alloy and evolution of its thermal expansion and elastic stiffness coefficients with temperature. *Scripta Materialia*, 177:44–48, mar 2020, doi:10.1016/j.scriptamat.2019.09.020.
(Cited on page 62).

[142] Z. Zhang, M. M. Mao, J. Wang, B. Gludovatz, Z. Zhang, S.X. Mao, E.P. George, Q. Yu, and R.O. Ritchie. Nanoscale origins of the damage tolerance of the high-entropy alloy CrMnFeCoNi. *Nature Communications*, 6(1):10143, dec 2015, doi:10.1038/ncomms10143.
(Cited on page 62).

[143] Z. Zhang, H. Sheng, Z. Wang, B. Gludovatz, Z. Zhang, E.P. George, Q. Yu, S.X. Mao, and R.O. Ritchie. Dislocation mechanisms and 3D twin architectures generate exceptional strength-ductility-toughness combination in CrCoNi medium-entropy alloy. *Nature Communications*, 8(1):14390, apr 2017, doi:10.1038/ncomms14390.
(Cited on page 62).

[144] S. Yoshida, T. Bhattacharjee, Y. Bai, and N. Tsuji. Friction stress and Hall-Petch relationship in CoCrNi equi-atomic medium entropy alloy processed by severe plastic deformation and subsequent annealing. *Scripta Materialia*, 134:33–36, jun 2017, doi:10.1016/j.scriptamat.2017.02.042.
(Cited on page 62).

[145] M. Schneider, E.P. George, T.J. Manescau, T. Záležák, J. Hunfeld, A. Dlouhý, G. Eggeler, and G. Laplanche. Analysis of strengthening due to grain boundaries and annealing twin boundaries in the CrCoNi medium-entropy alloy. *International Journal of Plasticity*, 124:155–169, jan 2020, doi:10.1016/j.ijplas.2019.08.009.

[146] M.D. Sangid, T. Ezaz, H. Sehitoglu, and I.M. Robertson. Energy of slip transmission and nucleation at grain boundaries. *Acta Materialia*, 59(1):283–296, jan 2011, doi:10.1016/j.actamat.2010.09.032.
(Cited on page 62 and 62).

[147] P. Chowdhury, H. Sehitoglu, H.J. Maier, and R. Rateick. Strength prediction in NiCo alloys – The role of composition and nanotwins. *International Journal of Plasticity*, 79:237–258, apr 2016, doi:10.1016/j.ijplas.2015.07.002.
(Cited on page 62).

[148] F. Habiyaremye, A. Guitton, F. Schäfer, F. Scholz, M. Schenider, J. Frenzel, G. Laplanche, and N. Maloufi. Plasticity induced by nanoindentation in a CrCoNi medium-entropy alloy studied by accurate electron channeling contrast imaging revealing dislocation-low angle grain boundary interactions. *Materials Science and Engineering: A*, 817:141364, jun 2021, doi:10.1016/j.msea.2021.141364.
(Cited on pages 63, 63, 64, 65, 66, 67, 92, 99 and 100).

[149] F. Pöhl. Pop-in behavior and elastic-to-plastic transition of polycrystalline pure iron during sharp nanoindentation. *Scientific Reports*, 9(1):15350, dec 2019, doi:10.1038/s41598-019-51644-5.
(Cited on page 63).

[150] M. Kawamura, M. Asakura, N.L. Okamoto, K. Kishida, H. Inui, and E.P. George. Plastic deformation of single crystals of the equiatomic CrMnFeCoNi high-entropy alloy in tension and compression from 10 K to 1273 K. *Acta Materialia*, 203:116454, jan 2021, doi:10.1016/j.actamat.2020.10.073.
(Cited on page 67).

[151] S. Ismail-Beigi and T. A. Arias. Ab Initio Study of Screw Dislocations in Mo and Ta: A New Picture of Plasticity in bcc Transition Metals. *Physical Review Letters*, 84(7):1499–1502, feb 2000, doi:10.1103/PhysRevLett.84.1499.
(Cited on page 69).

[152] D. Rodney, L. Ventelon, E. Clouet, L. Pizzagalli, and F. Willaime. Ab initio modeling of dislocation core properties in metals and semiconductors. *Acta Materialia*, 124:633–659, feb 2017, doi:10.1016/j.actamat.2016.09.049.

[153] H. Li, S. Wurster, C. Motz, L. Romaner, C. Ambrosch-Draxl, and R. Pippan. Dislocation-core symmetry and slip planes in tungsten alloys: Ab initio calculations and microcantilever bending experiments. *Acta Materialia*, 60(2):748–758, jan 2012, doi:10.1016/j.actamat.2011.10.031.
(Cited on page 69).

[154] TIMET. TIMETAL 21S: high strength, oxidation resistant strip alloy, 2000.
(Cited on page 70).

[155] L. Weiss, J. Zollinger, P. Sallamand, E. Cicala, A. Mathieu, and E. Fleury. Mechanical properties and microstructural study of homogeneous and heterogeneous laser welds in α, β, and $\alpha + \beta$ titanium alloys. *Welding in the World*, 63(1):53–62, jan 2019, doi:10.1007/s40194-018-0627-1.
(Cited on page 70).

[156] M. Ben Haj Slama, N. Maloufi, J. Guyon, S. Bahi, L. Weiss, and A. Guitton. In situ macroscopic tensile testing in sem and electron channeling contrast imaging: Pencil glide evidenced in a bulk beta-ti21s polycrystal. *Materials*, 12:2479, 2019.
(Cited on pages 71, 72, 72, 73, 75, 76, 92, 92 and 101).

[157] AC/DC Module User's Guide: COMSOL Multiphysics, 2018.
(Cited on page 71).

[158] D. An, H. Zhao, B. Sun, and S. Zaefferer. Direct observations of collinear dislocation interaction in a Fe-17.4 Mn-1.50 Al-0.29 C (wt.in-situ electron channelling contrast imaging and cross-correlation electron backscatter diffraction. *Scripta Materialia*, 186:341–345, sep 2020, doi:10.1016/j.scriptamat.2020.05.044.
(Cited on page 74).

[159] K. Nakafuji, M. Koyama, and K. Tsuzaki. In-Situ Electron Channeling Contrast Imaging under Tensile Loading: Residual Stress, Dislocation Motion, and Slip Line Formation. *Scientific Reports*, 10(1):2622, dec 2020, doi:10.1038/s41598-020-59429-x.

[160] S. Wei and C.C. Tasan. Deformation faulting in a metastable CoCrNiW complex concentrated alloy: A case of negative intrinsic stacking fault energy? *Acta Materialia*, 200:992–1007, nov 2020, doi:10.1016/j.actamat.2020.09.056.
(Cited on page 74).

[161] N. Gao, D. Perez, G.H. Lu, and Z.G. Wang. Molecular dynamics study of the interaction between nanoscale interstitial dislocation loops and grain boundaries in BCC iron. *Journal of Nuclear Materials*, 498:378–386, jan 2018, doi:10.1016/j.jnucmat.2017.10.069.
(Cited on page 74).

[162] K.J. Kim, J.H. Yoon, M.H. Cho, and H. Jang. Molecular dynamics simulation of dislocation behavior during nanoindentation on a bicrystal with a Σ=5 (210) grain boundary. *Materials Letters*, 60(28):3367–3372, dec 2006, doi:10.1016/j.matlet.2006.03.020.

[163] J. Guénolé, M. Zubair, S. Roy, Z. Xie, M. Lipińska-Chwałek, S. Sandlöbes-Haut, and S. Korte-Kerzel. Exploring the transfer of plasticity across Laves phase interfaces in a dual phase magnesium alloy. *Materials & Design*, 202:109572, apr 2021, doi:10.1016/j.matdes.2021.109572.

[164] L.A. Zepeda-Ruiz, A. Stukowski, T. Oppelstrup, N. Bertin, N.R. Barton, R. Freitas, and V.V. Bulatov. Atomistic insights into metal hardening. *Nature Materials*, 20(3):315–320, mar 2021, doi:10.1038/s41563-020-00815-1.
(Cited on page 74).

[165] F. Roters, P. Eisenlohr, L. Hantcherli, D.D. Tjahjanto, T.R. Bieler, and D. Raabe. Overview of constitutive laws, kinematics, homogenization and multiscale methods in crystal plasticity finite-element modeling: Theory, experiments, applications. *Acta Materialia*, 58(4):1152–1211, feb 2010, doi:10.1016/j.actamat.2009.10.058.
(Cited on page 75).

[166] J. Kochmann, S. Wulfinghoff, L. Ehle, J. Mayer, B. Svendsen, and S. Reese. Efficient and accurate two-scale FE-FFT-based prediction of the effective material behavior of elasto-viscoplastic polycrystals. *Computational Mechanics*, 61(6):751–764, jun 2018, doi:10.1007/s00466-017-1476-2.
(Cited on page 75).

[167] G. Taylor and J. W. Christian. Experiments on the deformation of niobium single crystals. *Philosophical Magazine*, 15(137):893–929, may 1967, doi:10.1080/14786436708221636.
(Cited on page 75).

[168] B. Douat, C. Coupeau, J. Bonneville, M. Drouet, L. Vernisse, and L. Kubin. Atomic-scale insight into non-crystallographic slip traces in body-centred cubic crystals. *Scripta Materialia*, 162:292–295, mar 2019, doi:10.1016/j.scriptamat.2018.10.032.
(Cited on page 75).

[169] G. Taylor and C.F. Elam. The distortion of iron crystals. *Proceedings of the Royal Society of London. Series A, Containing Papers of a Mathematical and Physical Character*, 112(761):337–361, sep 1926, doi:10.1098/rspa.1926.0116.
(Cited on page 76).

[170] A. Seeger and W. Wasserbäch. Anomalous Slip - A Feature of High-Purity Body-Centred Cubic Metals. *physica status solidi (a)*, 189(1):27–50, jan 2002, doi:10.1002/1521-396X(200201)189:1<27::AID-PSSA27>3.0.CO;2-T.

[171] W. Pichl. Slip Geometry and Plastic Anisotropy of Body-Centered Cubic Metals. *physica status solidi (a)*, 189(1):5–25, jan 2002, doi:10.1002/1521-396X(200201)189:1<5::AID-PSSA5>3.0.CO;2-D.
(Cited on page 76).

[172] P. Gilormini, B. Bacroix, and J.J. Jonas. Theoretical analyses of <111> pencil glide in b.c.c. crystals. *Acta Metallurgica*, 36(2):231–256, feb 1988, doi:10.1016/0001-6160(88)90001-6.
(Cited on page 76).

[173] L. Dezerald, D. Rodney, E. Clouet, L. Ventelon, and F. Willaime. Plastic anisotropy and dislocation trajectory in BCC metals. *Nature Communications*, 7(1):11695, sep 2016, doi:10.1038/ncomms11695.
(Cited on page 100).

[174] L. T. Le, K. Ammar, and S. Forest. Efficient simulation of single and polycrystal plasticity based on the pencil glide mechanism. *Comptes Rendus. Mécanique*, 348(10-11):847–876, jan 2021, doi:10.5802/crmeca.44.
(Cited on page 76).

[175] M. Ben Haj Slama, V. Taupin, N. Maloufi, K. Venkatraman, A.D. Rollett, R.A. Lebensohn, S. Berbenni, B. Beausir, and A. Guitton. Electron channeling contrast imaging characterization and crystal plasticity modelling of dislocation activity in Ti21S BCC material. *Materialia*, 15:100996, mar 2021, doi:10.1016/j.mtla.2020.100996.
(Cited on pages 76, 76, 77, 78, 79, 93 and 101).

[176] K. Venkatraman, M. Ben Haj Slama, V. Taupin, N. Maloufi, and A. Guitton. Tuning critical resolved shear stress ratios for bcc-titanium Ti21S via an automated data analysis approach. *Modelling and Simulation in Materials Science and Engineering*, 29(5):055014, jul 2021, doi:10.1088/1361-651X/abfeb0.
(Cited on pages 76, 76, 77, 77, 77, 78, 78, 79, 79, 93 and 101).

[177] A. Reuss. Berechnung der Fließgrenze von Mischkristallen auf Grund der Plastizitätsbedingung für Einkristalle . *ZAMM - Zeitschrift für Angewandte Mathematik und Mechanik*, 9(1):49–58, 1929, doi:10.1002/zamm.19290090104.
(Cited on page 77).

[178] A. Molinari, G.R. Canova, and S. Ahzi. A self consistent approach of the large deformation polycrystal viscoplasticity. *Acta Metallurgica*, 35(12):2983–2994, dec 1987, doi:10.1016/0001-6160(87)90297-5.
(Cited on page 77).

[179] R.A. Lebensohn and C.N. Tomé. A self-consistent anisotropic approach for the simulation of plastic deformation and texture development of polycrystals: Application to zirconium alloys. *Acta Metallurgica et Materialia*, 41(9):2611–2624, sep 1993, doi:10.1016/0956-7151(93)90130-K.
(Cited on page 77).

[180] C. Mareau and S. Berbenni. An affine formulation for the self-consistent modeling of elasto-viscoplastic heterogeneous materials based on the translated field method. *International Journal of Plasticity*, 64:134–150, jan 2015, doi:10.1016/j.ijplas.2014.08.011.
(Cited on page 77).

[181] S. Lhadi, S. Berbenni, N. Gey, T. Richeton, and L. Germain. Micromechanical modeling of the effect of elastic and plastic anisotropies on the mechanical

behavior of β-Ti alloys. *International Journal of Plasticity*, 109:88–107, oct 2018, doi:10.1016/j.ijplas.2018.05.010.
(Cited on page 77).

[182] R.A. Lebensohn, A.K. Kanjarla, and P. Eisenlohr. An elasto-viscoplastic formulation based on fast Fourier transforms for the prediction of micromechanical fields in polycrystalline materials. *International Journal of Plasticity*, 32-33:59–69, may 2012, doi:10.1016/j.ijplas.2011.12.005.
(Cited on page 77).

[183] F. Roters, M. Diehl, P. Shanthraj, P. Eisenlohr, C. Reuber, S.L. Wong, T. Maiti, A. Ebrahimi, T. Hochrainer, H.-O. Fabritius, S. Nikolov, M. Friák, N. Fujita, N. Grilli, K.G.F. Janssens, N. Jia, P.J.J. Kok, D. Ma, F. Meier, E. Werner, M. Stricker, D. Weygand, and D. Raabe. DAMASK – The Düsseldorf Advanced Material Simulation Kit for modeling multi-physics crystal plasticity, thermal, and damage phenomena from the single crystal up to the component scale. *Computational Materials Science*, 158:420–478, feb 2019, doi:10.1016/j.commatsci.2018.04.030.
(Cited on page 77).

[184] V. Hounkpati, S. Fréour, D. Gloaguen, V. Legrand, J. Kelleher, W. Kockelmann, and S. Kabra. In situ neutron measurements and modelling of the intergranular strains in the near-β titanium alloy Ti-β21S. *Acta Materialia*, 109:341–352, may 2016, doi:10.1016/j.actamat.2016.02.065.
(Cited on page 78).

[185] C. Kusche, T. Reclik, M. Freund, T. Al-Samman, U. Kerzel, and S. Korte-Kerzel. Large-area, high-resolution characterisation and classification of damage mechanisms in dual-phase steel using deep learning. *PLOS ONE*, 14(5):e0216493, may 2019, doi:10.1371/journal.pone.0216493.
(Cited on page 79).

[186] S. Medghalchi, C.F. Kusche, E. Karimi, U. Kerzel, and S. Korte-Kerzel. Damage Analysis in Dual-Phase Steel Using Deep Learning: Transfer from Uniaxial to Biaxial Straining Conditions by Image Data Augmentation. *JOM*, 72(12):4420–4430, dec 2020, doi:10.1007/s11837-020-04404-0.

[187] R.R.P. Purushottam Raj Purohit, T. Richeton, S. Berbenni, L. Germain, N. Gey, T. Connolley, and O. Castelnau. Estimating single-crystal elastic constants of polycrystalline β metastable titanium alloy: A Bayesian inference analysis based on high energy X-ray diffraction and micromechanical modeling. *Acta Materialia*, 208:116762, apr 2021, doi:10.1016/j.actamat.2021.116762.

[188] K. Sedighiani, M. Diehl, K. Traka, F. Roters, J. Sietsma, and D. Raabe. An efficient and robust approach to determine material parameters of crystal plasticity constitutive laws from macro-scale stress–strain curves. *International Journal of Plasticity*, 134:102779, nov 2020, doi:10.1016/j.ijplas.2020.102779.
(Cited on page 79).

[189] K. Venkatraman, V. Taupin, and A. Guitton. Dimensionality reduction using principal component analysis to classify different grain boundary slip transfer regimes in BCC-Titanium Ti21S: A feature engineering-based approach. *Under review*, ??(??):??, ?? 2021, doi:??
(Cited on page 80 and 80).

[190] UNESCO Kalinga prize for the popularization of science.
(Cited on page 83).

[191] Universal Declaration of Human Rights.
(Cited on page 83).

[192] W.G. Cochran and G.M. Cox. *Experimental Design*. Wiley, 1992.
(Cited on page 94).

Résumé : Les travaux de recherche présentés ici portent sur des méthodologies expérimentales et mésoscopiques permettant d'établir statistiquement les liens entre les mécanismes opérant à l'échelle des dislocations et ceux opérant à l'échelle du polycristal. L'hypothèse sous-jacente de ce travail est la mise en œuvre de procédures expérimentales, qui permettent d'une part d'observer et d'autre part, de caractériser les défauts cristallins sur un échantillon polycristallin massif. Ainsi, les résultats obtenus peuvent être confrontés de manière pertinente aux modèles micromécaniques. Le premier chapitre de ce mémoire se concentre à rappeler l'importance du rôle des microstructures dans les mécanismes de déformation. L'exemple des phases MAX, dont la microstructure est très anisotrope, est donné. Une ouverture vers l'influence des changements de chemins de déformation sur la plasticité est également faite. Ensuite le second chapitre résume l'apport de la microscopie électronique, et notamment de la Microscopie Électronique à Balayage (MEB) pour la caractérisation fine des microstructures. L'accent est mis, dans le troisième chapitre, sur la physique et l'optimisation de la technique MEB d'imagerie par contraste de canalisation des électrons (Electron Channeling Contrast Imaging : ECCI) dans le but de suivre l'évolution des microstructures avec la déformation. Le chapitre 4, quant à lui, souligne le potentiel de l'ECCI pour le suivi de l'évolution des défauts cristallins au voisinage d'une seule interface localement déformée par nanoindentation. L'illustration est donnée en s'appuyant sur un alliage d'aluminiure de titane et un alliage à médium-entropie. Enfin quelques modèles de plasticité cristalline sont confrontés statistiquement et de manière *in-situ* avec l'expérience dans le cas d'un alliage de titane β-métastable.

Mots clés : plasticité ; microstructures ; microscopies ; ECCI; phases MAX ; TiAl ; alliage à médium entropie ; alliage de Ti β-metastable.

Abstract:

Research presented here focuses on experimental and mesoscopic methodologies to statistically establish the links between operating mechanisms at the dislocation scale and those operating at the polycrystal scale. The underlying assumption of this work is the development of experimental procedures, which allow on the one hand to observe and on the other hand, to characterize crystalline defects on bulk polycrystalline specimen. Therefore, obtained outcomes can be compared relevantly with micromechanical models. First chapter focuses on emphasizing the importance of the role of microstructures in deformation mechanisms. The example of MAX phases, whose microstructure is very anisotropic, is given. An opening on the influence of strain-path changes on plasticity is also done. Then, second chapter summarizes the contribution of electron microscopy, and in particular Scanning Electron Microscopy (SEM) for the fine characterization of microstructures. Third chapter emphases the physics and the optimization of the SEM technique of Electron Channeling Contrast Imaging (ECCI) in order to follow the evolution of microstructures with deformation. Chapter 4, on the other hand, highlights the potential of ECCI for capturing the evolution of crystalline defects in the vicinity of a single interface locally deformed by nanoindentation. Illustration is given with a titanium aluminide alloy and a medium entropy alloy. Finally, some models of crystal plasticity are compared statistically and *in-situ* with experiences in the case of a β-metastable titanium alloy.

Keywords: plasticity; microstructures; microscopies; ECCI; MAX phases; TiAl; medium entropy alloy; β-metastable Ti alloy.